IntechOpen

Phase Change Materials and Their Applications

Edited by Mohsen Mhadhbi

PHASE CHANGE MATERIALS AND THEIR APPLICATIONS

Edited by **Mohsen Mhadhbi**

Phase Change Materials and Their Applications
http://dx.doi.org/10.5772/intechopen.71894
Edited by Mohsen Mhadhbi

Contributors

Cheng Wang, Ye Zhu, Quan Shi, Zhi-Cheng Tan, Xin Liu, Xuetong Zhang, Guangyong Li, Xiaohua Zhang, Jesumathy Jesumathy, Daolin Cai, Zhitang Song, Yifeng Chen, Manish K Rathod, Liping Wei, Guodong Jiang, Mohsen Mhadhbi

Notice

First published in London, United Kingdom, 2018 by IntechOpen
eBook (PDF) Published by IntechOpen, 2019
IntechOpen is the global imprint of INTECHOPEN LIMITED, registered in England and Wales, registration number: 11086078, The Shard, 25th floor, 32 London Bridge Street
London, SE19SG – United Kingdom
Printed in Croatia

British Library Cataloguing-in-Publication Data
A catalogue record for this book is available from the British Library

Additional hard and PDF copies can be obtained from orders@intechopen.com

Phase Change Materials and Their Applications
Edited by Mohsen Mhadhbi

p. cm.

Print ISBN 978-1-78923-530-2

Online ISBN 978-1-78923-531-9

eBook (PDF) ISBN 978-1-83881-623-0

Meet the editor

Dr. Mohsen Mhadhbi received his PhD degree in Chemistry from the Faculty of Sciences of Sfax, University of Sfax (Tunisia). Since 2011, he has been an Assistant Professor and a member of a research team at the Laboratory of Useful Materials, National Institute of Research and Physical-Chemical Analysis, University of Carthage (Tunisia), focusing on the synthesis and characterization of nanomaterials for industrial responders (hydrogen storage, cutting tools, and biomedical applications). He served as a teacher in Inorganic Chemistry at different institutes in Tunisia and supervised several researchers in Materials Science. He has published works in national and international impacted journals and books. Dr. Mhadhbi is a member of different associations. He is also a reviewer and an editorial board member of different scientific journals and congresses.

Contents

Preface

Phase change materials (PCMs) have desirable electronic and optical properties that depend on the structure of atoms (crystalline state or amorphous state). These materials use the latent heat of phase change to control temperatures in a specific range and are suitable for building applications (by their incorporation into construction materials). They possess a low environmental impact and are nonpolluting during service life.

This book is devoted to a detailed understanding of the phase change materials and their wider applications in the industry; hence, the future perspectives of PCMs are discussed in this book.

Section 1 provides an introduction and the history of phase change materials. The experimental and numerical studies of PCMs are discussed in Section 2, while the thermal stability of PCMs is the subject of Section 3. Section 4 discusses the latent heat thermal energy storage system. Finally, the applications of PCMs are the focus of Section 5. This book provides the reader with a more thorough understanding of the subject. It covers various aspects of the subject and hence can be tailored for different audiences.

I would like to thank the publisher for taking a keen interest in bringing out this edition on time.

Mohsen Mhadhbi
Laboratory of Useful Materials
National Institute of Research and Physical-chemical Analysis
Technopole, Sidi Thabet, Ariana, Tunisia

Section 1

An Introduction to Phase Change Material

Chapter 1

Introductory Chapter: Phase Change Material

Mohsen Mhadhbi

Additional information is available at the end of the chapter

http://dx.doi.org/10.5772/intechopen.79432

1. Introduction

The discovery of phase change material (PCM) starts from the early 1900s in the work of Alan Tower Waterman of Yale University [1]. While studying thermionic emission of certain hot salts, Waterman noted some peculiarities in the conductivity of molybdenite (MoS_2). It was found that the conductivity of the chalcogenide can be altered progressively.

Phase change material or latent heat storage material is the most efficient used method to store thermal energy. Energy per unit mass is stored during phase changes from solid to liquid, and released during freezing at a constant temperature. The energy absorbed by the material allows increasing the vibrational energy states of the constituent atoms or molecules [2]. During melting, the atomic bonds loosen and consequently the material changes its state from solid to liquid. However, during solidification, the material transfers energy and, consequently, the molecules lose energy and order themselves in solid state.

There are several types of phase change material available, but the there are three main types: organic (paraffin and nonparaffin), inorganic (salt hydrates and metallic alloys), and eutectic (mixture of two or more PCM components: organic, inorganic, and both).

In the last decades, the researchers place emphasis on phase change material in which heat storage is carried out due to latent heat of fusion [3]. Application such PCM allows to lower the volume of heat storage units (HSUs), essentially. Low-temperature PCM became objects of prime investigations. However, the limited reserves of fossil fuel, the increase in greenhouse gas emissions, and the rapid growth of energy consumption have shed the light on the importance of effectively utilizing energy. For these reasons, the development of new sources of energy has been the focus of several researches. The use of phase change material for thermal energy storage provides a suitable solution, cheap and efficient energy storage, for improving the performance of energy systems and therefore reducing peak demand and

energy consumption. Thermal energy storage (TES) includes latent heat storage and thermochemical heat storage. Sensible heat storage requires large volumes because of its low energy density and requires proper design to discharge thermal energy. Hence, latent heat storage systems are low coast and easier to work than those thermochemical heat storage systems.

In this context, PCM-based cooling is a very attractive process of thermal control, considering the advantages of the PCM, such as high latent heat storage capacity, small volume change in the phase transformation, high specific heat capacity to provide additional sensible heat storage, chemical stability and no degradation for large number of cycles, phase transition occurs within the desired operating temperature range of the system high nucleation rate to avoid supercooling of the liquid phase, high thermal conductivity to assist the absorption and release of energy in the storage system, high density, noncorrosiveness, nonflammable, nontoxicity, relatively low cost, and high availability [4–6]. On the other hand, different solutions were then developed to improve the heat transfer in PCM-based thermal control units (TCUs), all related to the insertion of conducting paths or materials in the heat storage volume such as metal matrices or foams, micro- and nanosized metal and metal oxide fillers, discrete elements such as pins and fins, graphite, carbon nanotubes or fibers, and exfoliated graphite or graphene [7, 8].

2. Applications of PCM

The application of PCM has grown incrementally in various industries, such as the solar cooling and solar power plants [9], photovoltaic electricity systems [10], electronic industry [11], waste heat recovery systems [12], solar dryers in agricultural industry [13], domestic hot water [14], pharmaceutical products and preservation of food [15], and space industry [16]. Apart from the preceding utilizations, PCM improves energy performance and thermal comfort in buildings [17]. Therefore, PCM applications could be a powerful tool in designing net zero energy buildings [18]. PCM must be put in specific containers that depend on the thermal storage application [19]. The content of PCM depends on the specific thermal storage application. For example, in the case of building integrated latent heat storage, PCM can be contained in a porous matrix (wood, concrete, plasterboard, etc.).

The aim of this book is to assist the scientists and to provide the reader with a comprehensive overview of the properties of phase change material with a focus on their technological applications. The phase change characteristics by various investigators are reviewed with the applications of the phase change characteristics in information storage applications. The present status and future perspectives of phase change material are discussed.

Author details

Mohsen Mhadhbi

Address all correspondence to: mhadhbi_mohsen@yahoo.fr

Laboratory of Useful Materials, National Institute of Research and Physical-Chemical Analysis, Technopole, Sidi Thabet, Ariana, Tunisia

References

[1] Waterman AT. Positive ionisation of certain hot salts, together with some observations on the electrical properties of molybdenite at high temperatures. Philosophical Magazine. 1917;**33**:225

[2] Fleischer AS. Thermal Energy Storage Using Phase Change Materials: Fundamentals and Applications. SpringerBriefs in Thermal Engineering and Applied Science. Kulacki FA, Series editor. Minneapolis, MN, USA; 2015. 97 p. DOI: 10.1007/978-3-319-20922-7

[3] Kenisarin MM. High-temperature phase change materials for thermal energy storage. Renewable and Sustainable Energy Reviews. 2010;**14**:955-970. DOI: 10.1016/j.rser.2009.11.011

[4] Heine D, Abhat A. Investigation of physical and chemical properties of phase change materials for space heating/cooling applications. In Sun: Mankind's Future Source of Energy. Proceedings of the International Solar Energy Congress, New Delhi, India (January 1978;**1**:16-21). (A79-17276 05-44). Elmsford, N.Y.: Pergamon Press, Inc; 1978. pp. 500-506

[5] Khudhair AM, Farid MM. A review on energy conservation in building applications with thermal storage by latent heat using phase change materials. Energy Conversion and Management. 2004;**45**(2):263-275. DOI: 10.1016/S0196-8904(03)00131-6

[6] Tyagi VV, Buddhi D. PCM thermal storage in buildings: A state of art. Renewable and Sustainable Energy Reviews. 2007;**11**(6):1146-1166. DOI: 10.1016/j.rser.2005.10.002

[7] Fan L, Khodadadi JM. Thermal conductivity enhancement of phase change materials for thermal energy storage: A review. Renewable and Sustainable Energy Reviews. 2011;**15**:24-46. DOI: 10.1016/j.rser.2010.08.007

[8] Sarier N, Onder E. Organic phase change materials and their textile applications: An overview. Thermochimica Acta. 2012;**540**:7-60. DOI: 10.1016/j.tca.2012.04.013

[9] Aydin D, Casey SP, Riffat S. The latest advancements on thermochemical heat storage systems. Renewable and Sustainable Energy Reviews. 2015;**41**:356-367. DOI: 10.1016/j.rser.2014.08.054

[10] Ma T, Yang H, Zhang Y, Lu L, Wang X. Using phase change materials in photovoltaic systems for thermal regulation and electrical efficiency improvement: A review and outlook. Renewable and Sustainable Energy Reviews. 2015;**43**:1273-1284. DOI: 10.1016/j.rser.2014.12.003

[11] Dhaidan NS, Khodadadi JM. Melting and convection of phase change materials in different shape containers: A review. Renewable and Sustainable Energy Reviews. 2015;**43**:449-477. DOI: 10.1016/j.rser.2014.11.017

[12] Fang G, Tang F, Cao L. Preparation, thermal properties and applications of shape-stabilized thermal energy storage materials. Renewable and Sustainable Energy Reviews. 2014;**40**:237-259. DOI: 10.1016/j.rser.2014.07.179

[13] Shalaby SM, Bek MA, El-Sebaii AA. Solar dryers with PCM as energy storage medium: A review. Renewable and Sustainable Energy Reviews. 2014;**33**:110-116. DOI: 10.1016/j.rser.2014.01.073

[14] Seddegh S, Wang X, Henderson AD, Xing Z. Solar domestic hot water systems using latent heat energy storage medium: A review. Renewable and Sustainable Energy Reviews. 2015;**48**:517-533. DOI: 10.1016/j.rser.2015.04.147

[15] Belman-Flores JM, Barroso-Maldonado JM, Rodríguez-Muñoz AP, Camacho-Vázquez G. Enhancements in domestic refrigeration, approaching a sustainable refrigerator: A review. Renewable and Sustainable Energy Reviews. 2015;**51**:955-968. DOI: 10.1016/j.rser.2015.07.003

[16] Zhou Z, Zhang Z, Zuo J, Huang K, Zhang L. Phase change materials for solar thermal energy storage in residential buildings in cold climate. Renewable and Sustainable Energy Reviews. 2015;**48**:692-703. DOI: 10.1016/j.rser.2015.04.048

[17] AL-Saadi SN, Zhai Z. Modeling phase change materials embedded in building enclosure: A review. Renewable and Sustainable Energy Reviews. 2013;**21**:659-673. DOI: 10.1016/j.rser.2013.01.024

[18] Bastani A, Haghighat F, Kozinski J. Designing building envelope with PCM wallboards: Design tool development. Renewable and Sustainable Energy Reviews. 2014;**31**:554-562. DOI: 10.1016/j.rser.2013.12.031

[19] Konuklu Y, Ostry M, Paksoy HO, Charvat P. Review on using microencapsulated phase change materials (PCM) in building applications. Energy and Buildings. 2015;**106**:134-155. DOI: 10.1016/j.enbuild.2015.07.019

Section 2

Experimental and Numerical Study of Phase Change Material

Chapter 2

Experimental and Numerical Studies on Phase Change Materials

Cheng Wang and Ye Zhu

Additional information is available at the end of the chapter

http://dx.doi.org/10.5772/intechopen.76807

Abstract

Phase change materials (PCMs) are attracting significant attentions in research and application, categorized into mainly three types, that is, organic (O), inorganic (IO) and eutectic (E). This section introduces the experimental and numerical investigations conducted in recent decades, mainly focused on the properties enhancement of PCMs and the performance improvement of its application in latent heat storage (LHS) units, as well as the evaluation and optimization of LHS units. It was concluded that lots of contribution have been made to PCMs and LHS units analysis. However, there is still some weakness in research, such as the lackness of detailed and systematic research on properties, the non-uniform standard on testing method as well as the contradictory conclusions. The most evaluation of LHS units is based on energy, instead of exergy, entropy and entransy. There is another issue that most of the research is based on numerical analysis, while less experimental research is conducted, especially in the case of LHS unit.

Keywords: phase change materials (PCMs), latent heat storage (LHS), numerical, experimental

1. Introduction

Energy is the basis of modern society and is important for the survival of mankind as well as the development of civilization. Non-renewable and renewable sources are two kinds of energy source. Since the non-renewable energy source will be run out someday, the utilization of renewable energy source has been paid more and more attention in research. However, in most cases of renewable energy sources, such as solar and wind, intermittent nature is found. What is more, there is always a gap between energy supply and energy demand, as far as power, space and time in concern. Thus, energy storage technologies are proposed to solve or diminish this issue.

Energy is usually stored in energy storage (ES) system, in the form of mechanical, chemical, biological, magnetic and thermal. These energy storage forms can also be subsidized further in details. For instance, mechanical energy can be stored in compressed air, flywheel or hydro-pool, etc. and chemical energy can be stored in battery, reversible-reaction or hydrogen, etc. Among these energy storage forms, the most commonly used is the thermal energy storage (TES) with phase change materials (PCMs), due to its merits of low-cost, environmental-friend, easy-to-operate and abundant sources of storage facilities.

As a matter of fact, we human being has used renewable energy and conducted thermal energy storage, since quite a long time ago. For example, the ancient people utilized wind or hydro power to drive wheels for irrigation and they collected ice or snow in winter for cooling in summer. In modern society, we try to fully utilize the clean energy source, to deeply understand the process involved in TES process and to seek nature materials or manufacture artificial materials for TES. For the performance improvement of TES, the thermophysical properties are important limitations. For instance, the limited thermal conductivity of PCMs strongly constrains the conductive heat transfer process. The viscosity of PCMs at liquid phase also constrains the convective heat transfer process. In this section, we will introduce some progress of the research on PCMs and TES and discuss on the weak points.

2. Experimental studies of PCMs

Experiments studies were conducted on the properties of PCMs and the performance in LHS, as well as the enhancement.

2.1. Types and properties of PCMs

The materials involved in LHS are called as phase change materials (PCMs). There are varieties of PCMs under development, categorized as organic (O), inorganic (IO) and eutectic (E) materials, available in a wide range of melting/solidification temperature (**Figure 1**).

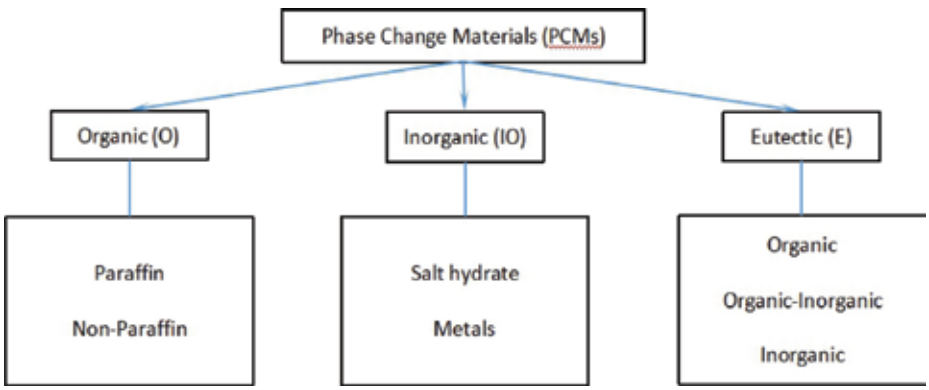

Figure 1. Categories of PCMs.

Thermal properties	Physical properties	Kinetic properties	Chemical properties	Economic availability
High latent heat of transition	Small volume change	Sufficient crystallization rate	Long-term chemical stability	Abundant
High thermal conductivity	Low vapor pressure	No supercooling	No toxicity	Cost effective
Suitable melting/ solidification temperature	High density		Non-flammable	Available
			Non-corrosive	Commercially viable

Table 1. Properties of PCMs in demand.

Desired property of PCMs includes thermodynamic, kinetic, physical and chemical properties, as well as economic availability, as shown in **Table 1**.

Unfortunately, there is not a single kind of PCMs that satisfies all the properties listed above. The most undesired character of PCMs property is its thermal conductivity, since it will limit the heat transfer during energy storage/release process and correspondingly lead to deteriorated performance of LHS unit. This is often the case, except for some metallic PCMs. For instance, several measures have been taken. The major technical method is to composite with materials of high thermal conductivity.

2.2. Types of TES

TES can be categorized as three types, that is, sensible heat storage (SHS), latent heat storage (LHS) and thermo-chemical storage (TCS). In the first type (SHS), thermal energy is stored as the temperature increase of certain matters, usually with large thermal capacity. So, the amount of energy storage Q can be easily estimated as the product of mass m, thermal capacity C and temperature uplift ΔT, as shown:

$$Q = \int_{T_1}^{T_2} m \cdot C \cdot dT \tag{1}$$

In the second type (LHS), thermal energy is stored as the phase change process of certain materials, including the transformation of phase between solid and liquid (S-L) in melting/ solidification process, between solid and gas (S-G) in sublimation/desublimation process, from liquid to gas (L-G) in condensation/evaporation process, as well as the transition from one solid phase to another (S-S). The amount of energy storage Q is the sum of the sensible heat stored in both phases and the latent heat involved in phase-transformation, which is the main portion of energy storage amount.

$$Q = \int_{T_1}^{T_m} m \cdot C_{phase\_1} \cdot dT + m \cdot \Delta H_m + \int_{T_m}^{T_2} m \cdot C_{phase\_2} \cdot dT \tag{2}$$

In the third type (TCS), thermal energy is stored in similar way as LHS. The major difference is that thermal energy is mainly stored as the enthalpy change in thermo-chemical reaction, instead of phase-transformation process.

Comparing with LHS and TCS, SHS technology often requires larger vessels. Comparing with LHS, TCS is associated with larger energy storage density, but is still at pre-mature state in terms of research and development. Therefore, latent heat storage (LHS) attracts the most attention in research and is believed as the most promising technology.

The performance of heat storage/release in PCMs is realized in LHS unit. The major favored characteristics of LHS unit includes faster rate of heat charging/discharging, higher efficiency of heat release, based on thermodynamic evaluations, including the basis of energy, exergy, entropy and entransy as well. Another important research field is the optimization of LHS unit.

It is widely accepted that performance of LHS unit is mainly constrained by heat transfer process. Therefore, heat transfer enhancement is a major task for LHS unit performance improvement in most research. Since heat transfer is generously expressed as:

$$Q = K \cdot A \cdot \Delta T_m \tag{3}$$

where K represents the heat transfer coefficient in conduction or convection process, A represents the surface area for heat transfer and ΔT_{m} represents the temperature difference between PCMs and HTF. The enhancement of heat transfer implies the increase of Q. So, it is obvious that there are three major methods for heat transfer enhancement of LHS unit, that is, increase of K, A and ΔT_{m}.

The heat transfer coefficient should include both conductive and convective. The increase of conductive heat transfer coefficient can be mainly traced back to the thermal conductivity enhancement on PCMs. The only exception would be the encapsulation of PCMs. As far as the increase of convective heat transfer coefficient, the theoretical basis is convective heat transfer. Therefore, the progress on convective heat transfer can be applied directly in the performance improvement of LHS unit, such as the influence of passage size and shape, the effects of faster flow velocity and the disturbed flow pattern. More effective increase of convective heat transfer coefficient should be attributed to the application of heat pipe (HP) technology.

2.3. Heat transfer enhancement techniques

Heat transfer for thermal energy storage applications with phase change materials is reviewed by Ref. [1]. The major measures include conductive heat transfer enhancement and convective heat transfer enhancement.

2.3.1. Composites with porous materials

Composite with porous materials is an effective method for thermal conductivity enhancement of PCMs. Impregnation is a fast-growing technology. The porous material offers space for PCMs and the high thermal conductivity of porous materials supports more effective heat

transfer in composite. Expanded graphite and metal foam are the mostly adopted porous materials.

Zhao and Wu [2] reported the considerable improvement of thermal conductivity of sodium nitrate with porous expanded graphite matrix and metal foams. The experimental results of embedding non-metallic PCMs in porous graphite showed tens or hundreds times of thermal conductivity improvement. Siaphush et al. [3] reported the effective thermal conductivity increased from 0.423 W/m/K to 3.06 W/m/K, when 95% porosity copper foam is adopted in PCMs of eicosane. It is also reported that critical porosity value exists for enhancement with porous carbon graphite foams. Yin et al. [4] reported in experiments that the critical mass fraction of porous graphite is 6.25%. Exceeding this value, the reinforcement effect decreases. Similar phenomenon is also found in our research on the effect of adoption expanded graphite in octadecane for performance improvement of LHS unit. However, the critical value is found at around 20%. Gao et al. [5] investigated the thermal performance of a direct contact thermal energy storage container with erythritol and expanded graphite. The thermal conductivity is reported as increased by about 2.5 times, with 4% mass fraction of EG, and the melting time is reduced by 16.7%.

Comparing with the amount of porous materials in composite, it is also reported that the pore structure is more important for composite. Lafdi et al. [6] investigated experimentally on the effects of foam porosity and pore size on the melting rate of PCMs. Zhong et al. [7] reported that small pore size and thick ligament in graphite foam leads to higher thermal diffusivity, while large pore size and thin ligament leads to larger latent heat storage capacity. Since the thermal diffusivity and latent heat storage density are both important factors, the pore size and ligament should be optimized in the design of LHS unit. Wu and Zhao [8] reported that mixed porous base is more effective than single porous base. Zhang et al. [9] studied the performance of metal foam (copper) and paraffin composite. Gulfam et al. [10] investigated the enhancement of thermal conductivity with expanded graphite in paraffin wax. Teppei et al. [11] reported high thermal conductivity of erythritol enhanced with porous nickel. Similar works are also reported by Nomura et al. with metal-stabilized carbon-fiber network [12] as well as expanded perlite, diatom earth and gamma-alumina [13].

Besides expanded graphite and metal foams, ceramic is also adopted recently as enhancement medium, as Li et al. [14] reported. With the development of material science, there should be more materials with porous structure, such as graphene, aerogel, etc., under consideration for the enhancement of thermal conductivity as well as other properties.

2.3.2. Dispersion of high conductive particles

The effect of addition of metal particles, especially with nano-size, on the enhancement of thermal conductivity of PCMs is also reported widely. Different from the obvious and established structure of compressed expanded graphite and metal foam, the distribution of particles are more like to expanded graphite in composite. However, the effects are usually better in the case of nano-particles addition. The reinforcement effect by the dispersion of nano-particles in continuous PCMs should be attributed to the unique phenomenon at microscopic

scale, for example, reduce the internal resistance for heat transfer, which is also reported for the thermal conductivity enhancement of heat transfer fluid (HTF) in literatures.

Fan et al. [15], Qi et al. [16], Tao et al. [17], Kim et al. [18] and Shi et al. [19] investigated the effects of several types of carbon-based nano-particles. It is found that disk carbon nano-particles can improve the thermal conductivity by 10 times. Besides graphite or graphene, carbon nanotubes (CNTs) are more typical nano-particles in composite. Zhang et al. [20] investigated on nanoscale heat transfer in composite of sugar alcohol and carbon nanotubes. It is reported that specific improvement of heat transfer depends on the material and the diameter of CNT. Carbon nano-fibers (CNFs) are another common nano-particles in composite. Fereshteh et al. [21] analyses the application of phase change material with carbon fibers for thermal management of a Li-ion battery cell. It is concluded that the application of carbon fibers influences the temperature distribution in cells. Higher concentration of carbon fibers leads to more uniform temperature distribution. The maximum thermal conductivity enhancement degree is reported as 115% and averaged at 105%. Nomura et al. [22] reported a significant reinforcement degree of thermal conductivity for erythritol. Different CNFs groups and its mixture are adopted. It is found that with the mixture of CNFs at different length, thermal conductivity is more enhanced, comparing with the addition of single CNFs. To further construct the network for heat transfer inside composite, low-melting metal, such as indium is added to help bridge CNFs nearby. In recent studies, other carbon materials are under research.

Besides the carbon materials, the addition of nano-metal-particles, such as Cu, Ti and other magnetic metals, in composite are also conducted by researchers Kibria et al. [23], Zhang et al. [24], Luo et al. [25], etc. It is concluded that the thermal conductivity is enhanced, and sometimes the thermal capacity is also enhanced. Mettawee et al. [26] reported the effect of Al powder on thermal conductivity enhancement of paraffin wax. Motahar et al. [27] reported non-monotonic behavior of thermal conductivity, and optimum value of nano-particles occurs in composite. Wang et al. [28] reported the increase of thermal conductivity with mass fraction of CNTs. Similar result of MWCNTs is also reported by Zeng et al. [29] for palmitic acid. Oya et al. [11] studied the thermal conductivity enhancement of erythritol with graphite and nickel particles. The largest enhancement is reported as 6.4 times higher, comparing with the thermal conductivity of pure phase change material, at 15% volume fraction of expanded graphite. Khyad et al. [30] adopted 1% mass fraction of aluminum or copper to enhance thermal conductivity of paraffin.

Since the nano-particle can enhance the thermal conductivity of PCMs with the similar mechanism, more research is expected on this scope, with the development of materials science on materials as well as the manufacture method.

2.3.3. Using extended surface

Surface area for heat transfer is the most common method applied for the heat transfer enhancement of LHS unit, mainly in the form of fin-structure. The adoption of fins increase the contact surface between HTF and PCMs. Research is mainly focused on the selection of fin materials as well as the configuration and number of fins in LHS unit. As far as fin materials are concerned, thermal conductivity, density, cost and corrosion as well as mechanical performance are major

concerns. Recently, mostly metal, such as copper, bronze, steel, stainless steel, aluminum alloy, etc., and sometimes graphite or ceramic are used as fin materials.

The core of fin-structure is its configuration, including shapes and orientation. The performance of single structured-fin will lead to the number of fins in demand is influential to the configuration of fins in LHS unit. The investigation of fin configuration is similar to heat exchanger (HE) with almost constant temperature boundary. The typical structure of LHS unit is tube-and-shell. So, there will be two forms of PCMs arrangement, that is, inside of tube and outside of tube as well as annual space between tubes.

As far as the orientation of fins is concerned, there are two mainly forms, that is, alongside and perpendicular to the axial direction. The fins can be arranged inside and outside of tubes (**Figure 2**).

Sparrow et al. [31] experimentally investigated the solidification process of PCMs in a finned vertical tube. It was concluded that conduction controls the process, when liquid temperature is lower and at melting temperature. While convection is the controlling mode for temperature above melting temperature. Tao et al. [32] investigated numerically with the performance of LHS unit in a photo-thermal (PT) application. Velraj et al. [33] reported with numerical and experimental analysis on vertical finned tube. The results show the reversal decrease of solidification period with number of fins. Zhao and Tan [34] investigated the effects of HTF temperature and flowrate as well as fin height on the charging rate of LHS unit. It is concluded that with the increase of HTF inlet temperature and mass flowrate, as well as the increase of fin height, the charging period is shortened, implying enhanced heat transfer process. Erek et al. [35] analyzed the effects of fin parameters, such as fin size and fin space, as well as the effects of HTF on the dimensionless energy storage value. Liu et al. [36] conducted similar experimental research on the melting of stearic acid in annual space. It is concluded that heat conduction and natural convection are both the factors for heat transfer enhancement in LHS unit. Hosseini et al. [37] concluded that with the increase of fin's height, the reduction of melting

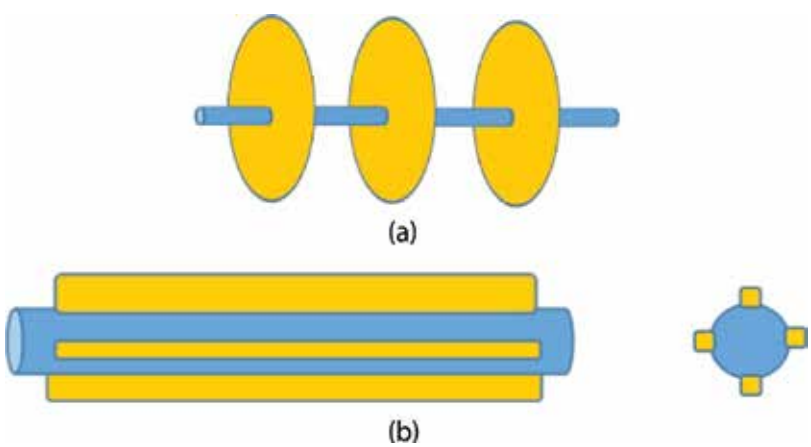

Figure 2. Sketch of fin configurations. (a) Perpendicular to the axial direction and (b) alongside the axial direction.

time exhibits a descending trend. Comparing with the melting process, effects of increasing fin's height is more significant in solidification process.

Besides the shell-and-tube configuration, numerical investigation on plate-type LHS is also conducted by Gharebaghi and Sezai [38] for rectangular heat sink. Sharifi et al. [39] developed an analytic model to predict the melting period of PCMs. Mahmoud et al. [40] conducted different arrangements for heat sink with PCMs at different melting temperature. It is concluded that increasing fin number is good for heat distribution in LHS unit and leading to lower the peak temperature of heat sink. Arshad et al. [41] studied the effects of pin thickness as well as the volume fraction of PCMs on the cooling performance of heat sinks for electronic devices. The volume fraction of PCMs is kept at 9%. The heating boundary is assumed as uniform heat flux. Heat sinks are finned or not finned. The thickness of fins is ranging from 1 mm to 3 mm, with the interval of 1 mm. The volume fraction of PCMs is ranging from 0 to 1, with the interval of 0.33. Rahimi et al. [42] investigated with the charging and discharging processes of PCMs in finned-tube heat exchanger in experiments. The utilization of fins reduces the melting and solidification periods. It is also reported that the increase of inlet temperature is more effective for melting time reduction in the bare tube heat exchangers. The variation of flow rate of HTF is also more intensely influential on the solidification time for the bare tube heat exchangers.

As reported in the review paper contributed by Nasiru et al. [1], the presence of fins improve the heat transfer during the phase change process, regardless of the make-up and geometry of the LHTES systems. However, few studies considered the effects of fin numbers on thermal response of the LHS unit. Although the trend is easy to find, the quantitative analysis will help the optimal design in practice.

2.3.4. Using multi-PCMs

The increase of ΔT_m should be expressed more precisely as the uniform distribution of the temperature difference between PCMs and HTF in LHS unit, during charging and discharging process. The benefits can be not only evaluated with the energy basis, but also with the exergy/entropy basis as well as the entransy basis, which is proposed in the recent decade.

According to the demand of uniform temperature difference between PCMs and HTF, the melting temperature of PCMs should decrease alongside the flow direction of HTF in charging process and increase alongside the flow direction of HTF in discharging process. This is usually realized by the transverse of flow direction of HTF in two processes.

Fang and Chen [43] numerically investigated the effects of multiple PCMs on the performance of LHS unit. It is concluded that difference of melting temperature between multiple PCMs is crucial for performance improvement. Wang et al. [44] proposed a new concept of homogeneous phase change process using multiple PCMs to significantly decrease the melting/solidification periods. Cui et al. [45] numerically analyzed the structure with three types of PCMs for solar receiver. It is reported that the fluctuation of HTF outlet temperature is better controlled, comparing with single PCMs. More energy flowrate is also expected. Hu et al. [46] proposed a thermal storage system with frustum-shape. Along the flow direction of HTF,

volume of PCMs change. Maximum five types of PCMs are adopted in the LHS unit. It is found effective even at small temperature difference. However, there is also some report about the asynchronous effects of multiple PCMs on the charging process and the discharging process, by Kurnia et al. [47]. It is concluded that the arrangement of PCMs with high melting temperature at the inlet of HTF would improve the heat transfer in discharging process, but may slightly worsen the charging process.

Thus, the major factor for multiple PCMs design is the match of melting temperature of PCMs in LHS unit. To better understand this issue and to provide guidance for the design of LHS unit, optimization of multi-stage LHS unit with multiple PCMs is conducted. Since there is no heat-and-work conversion during the operation of LHS unit, entransy theory is also adopted for optimization, besides the traditional energy and exergy/entropy analysis.

Tao et al. [48] reported the melting temperature match for double-stage LHS unit in charging process. Zhao et al. [49] reported the melting temperature match for multi-stage LHS unit in charging process. Wang et al. [50–52] reported the optimized match of melting temperature and surface for heat transfer of double- and multi-stage LHS unit in charging and cycle period.

However, less attention has been paid to the transient process optimization as well as other factors influencing the operation of LHS unit. Moreover, the comparison between entransy analysis and exergy analysis is important. Works are undergoing in our group. It is found that the difference between optimum melting temperature of nearby PCMs is constant in entransy analysis, while the ratio is constant in entropy analysis. The detailed discussion will be made. However, still the reason lies there, not so easy to answer, although we know that is superficially due to the difference between the optimization goals.

2.3.5. Encapsulation

Encapsulation of PCMs is also an effective method for heat transfer improvement in PCMs region. The mechanism may be explained as the reduce of heat transfer path as well as the increase of surface conducting heat transfer. Encapsulation of PCMs is to disperse PCMs in LHS unit into groups of small-sized particles closed and surrounded by other materials or the derivatives of PCMs itself after procedure of treatment. So, the direct property of PCMs is actually not changed, and the benefits are mainly contributed to the performance improvement of LHS unit as discussed later. The main research lies on the selection of raw-material and the method of encapsulation, as reviewed by Jacob and Bruno [53], Liu et al. [54], Saman et al. [55], Liu et al. [56], etc.

Jamekhorshid et al. [57] and Su et al. [58] reviewed the microencapsulation methods of PCMs. Milian et al. [59] reviewed on specific encapsulation techniques for inorganic phase change materials and the thermophysical properties. Sketch of encapsulated PCMs is expressed in **Figure 3**. The shell can be single layered or multiple layered or linked matrix, and the core can be single zone or several isolated zones. The shape could be regular, such as spherical, tubular or oval and irregular.

The methods of encapsulation are summarized in **Table 2**.

As far as the shell is concerned, Jacob and Bruno [53] reviewed on the shell materials in the encapsulation for high temperature thermal energy storage. Steel, nickel, sodium silicate,

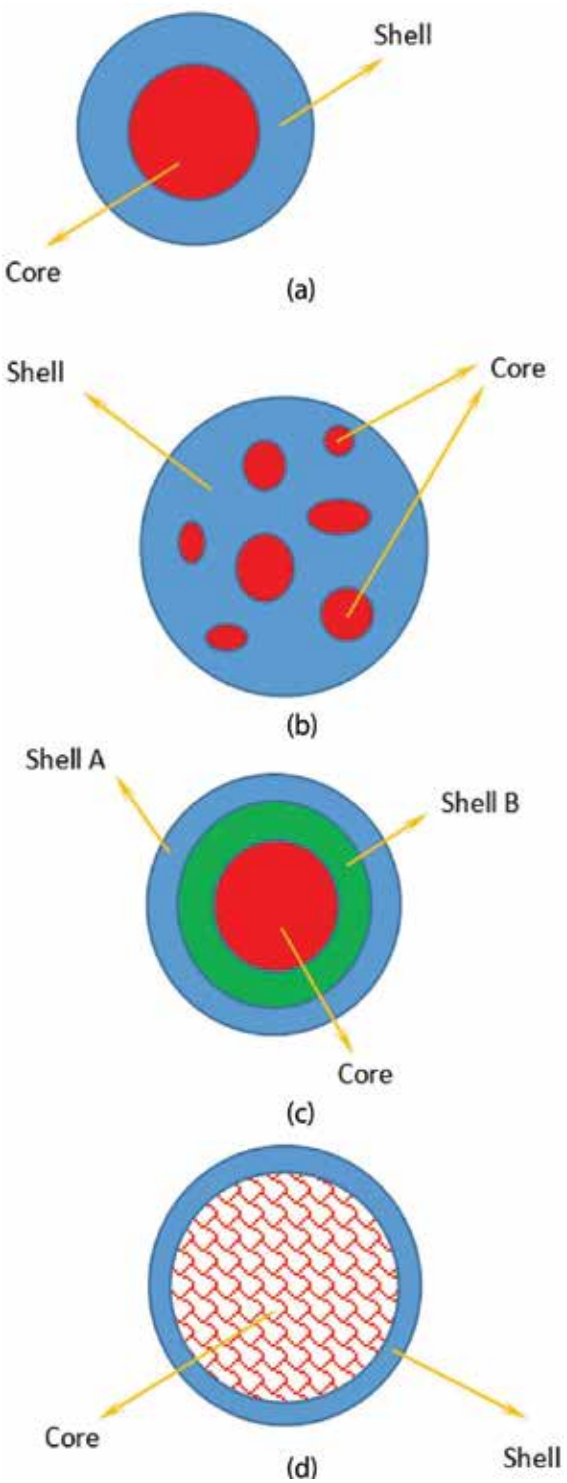

Figure 3. Sketch of encapsulated PCMs shapes. (a) Mononuclear; (b) polynuclear; (c) multi-wall; (d) matrix.

Physical methods	Chemical methods	Physic-chemical methods
Pan coating	Interfacial polymerization	Ionic gelation
Air-suspension coating	Suspension polymerization	Coacervation
Centrifugal extrusion	Emulsion polymerization	Sol-gel
Vibration nozzle		
Spray drying		
Solvent evaporation		

Table 2. Methods of encapsulation of PCMs.

silicon dioxide, calcium carbonate and titanium dioxide are identified as shell materials. It is better to further consider the corrosion between shell materials and PCMs encapsulated, which is important for long-term stability as well as cost reduction. Ma et al. [60] reported an encapsulated metallic phase change materials. The shell material is iron and the core material is copper. The preparation is based on aerodynamic levitation method. It is concluded that the morphology evolution is attributed to the combined effects of liquid phase fraction of two not-miscible liquids, Stokes and Marangoni velocities of droplets, as well as the rotation direction of particles in the solidification process. Chen et al. [61] reported the preparation of nanocapsules. The core PCMs is n-dodecanol and the encapsulation method is miniemulsion polymerization with polymerizable emulsifier. The diameter is measured as 150 nm and the phase change temperature is 18.2°C. Yang et al. [62] proposed a hybrid elastomeric spherical structure. It is composed of foam core and solid shell. The performance is predicted with numerical investigation.

2.3.6. Application of heat pipe

Heat pipe is a thermal carrier to transfer heat from hot medium to cold medium spatially separated. Heat pipe has its own working fluid, flowing inside at closed or open mode. At the end of hot medium, the liquid phase working fluid evaporates and flows to the end of cold medium, where the gas phase working fluid condensates and flows back to the end of hot medium and makes a cycle. Since phase change is involved, heat pipe usually can supply better performance of heat transfer between hot medium and cold medium.

There are two operation modes of HP in LHS unit. The first is simultaneous heating for discharging and cooling for charging, and the other is intermittent heating and cooling. To some extent, the latter mode is easier to understand, and the former mode is better for the power match and good for continuous operation. In the intermittent mode, PCMs operates as the hot end of HP in discharging process of LHS unit and as the cold end of HP in charging process.

Shabgard et al. [63] developed a thermal network model to investigate the performance of cascaded PCMs and conducted exergy analysis. Shabgard et al. [64] considered the transient response of HP-assisted LHTES system with a 2D model. It is concluded that HP spacing is the key parameter for LHS unit design and controls the dynamic response of the system. Robak

et al. [65] experimentally investigated the performance of HP-assisted LHTES system. It is concluded that with the assistance of HP, heat transfer during discharging process is almost twice improved. Bergman et al. [66] numerically investigated the performance of LHTES with HP in solar thermal power plant and reported increased charging/discharging rate of PCMs for two kinds of HTF flow pattern. Nithyanandam and Pitchumani [67] conducted a similar computational analysis on 3D physical model. In another work of Nithyanandam and Pitchumani [68], dynamic performance behavior of HP-assisted LHTES system is investigation with the consideration of cyclic operation.

However, most of the research is based on gravity-assisted HP. With the development of HP technology, other kinds of HP should also be considered for application in LHS unit. Moreover, it is found that most of the HP-assisted LHTES system is analyzed numerically and less attention has been paid to the experimental analysis. This will be an open field for research in the future.

2.3.7. Combined heat transfer enhancement techniques

With two or more techniques, such as the combination of fin-structure and heat pipe, or the combination of multiple PCMs and heat pipe, it is expected possible to further improve performance of LHS unit. Jung and Boo [69] numerically investigated the transient behavior of a LHS unit with fin-structured heat pipe. They used a row-by-row analysis method to estimate the layer necessary for system design. It is concluded that the increase of pitch would help increase heat transfer rate. Khalifa et al. [70] compared the performance of bare heat pipe and finned heat pipe. It is concluded that with fin-structure, energy efficiency is improved significantly. Nithyanandam and Pitchumani [71] conducted numerical analysis on LHSTES system with metal foam and embedded heat pipe. It is reported that the augmentation in heat transfer rate during charging decreased with pore-density of metal foam, due to the restriction in the formation of buoyancy-induced convection.

3. Numerical studies of PCMs

Although the results of numerical analysis are not always the case in practice, it offers an important way to investigate the process as well as the performance of phase change materials as well as latent heat storage units, characterized with less cost and short time occupation as well as convenience of parameter adjustment. The focus and the core in numerical analysis rely on the model used as well as the verification and modification of numerical models with experimental results.

3.1. Numerical models

Esen et al. [72] applied two models to describe the diurnal transient behavior of energy storage tanks. In the first model, HTF is flowing outside of pipe, the inside of which is filled with PCMs. In the second model, HTF is flowing inside of pipe, the outside of which is surrounded

with PCMs. Two-dimensional analysis is conducted with enthalpy-based method, coupled with convective heat transfer between HTF and PCMs. The effects of properties of PCMs, parameters of geometry, such as the radius and height of cylinder or pipe, and characters of HTF, such as velocity and inlet temperature, on the melting time are discussed (**Figure 4**).

The expression of Nu is listed as:

For heat transfer inside tube:

$$Nu_{\mathrm{p}} = 3.66(\mathrm{Re} \leq 2200) \tag{4}$$

$$Nu_{\mathrm{p}} = 0.023 \cdot \mathrm{Re}^{0.8} \cdot \mathrm{Pr}^{0.4}(\mathrm{Re} > 2200) \tag{5}$$

For heat transfer outside tube:

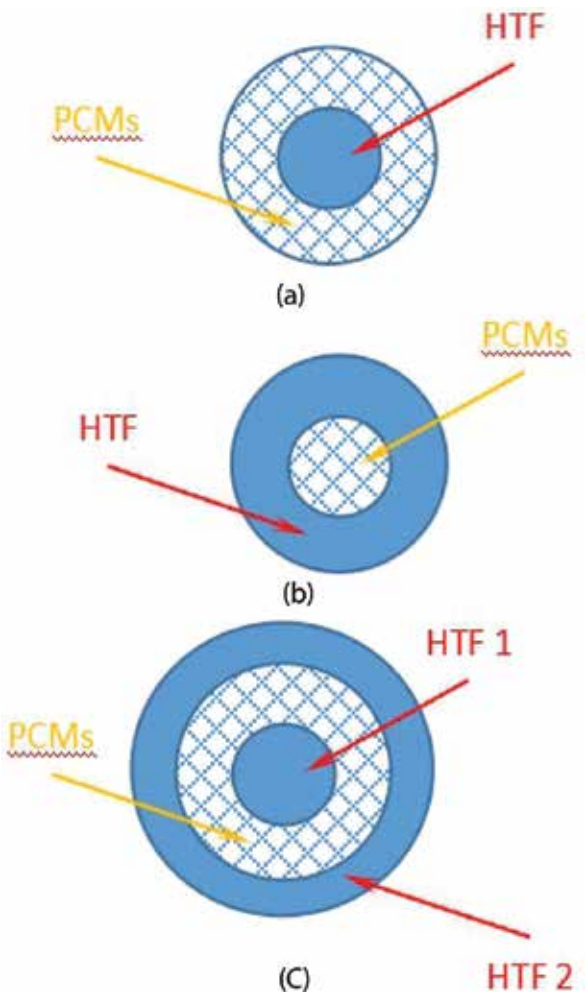

Figure 4. Configuration of HTF passage. (a) Outside of tube; (b) inside of tube; (c) annual between tubes.

$$Nu_{\mathrm{c}} = 3.66 + 4.12 \cdot \left(\left(\frac{D}{R} \right) - 0.205 \right)^{0.569} \mathrm{Re} \leq 2200 \tag{6}$$

$$\frac{Nu_{\mathrm{c}}}{Nu_{\mathrm{p}}} = 1.08 - 0.794 \cdot e^{-1.62 \cdot \frac{D}{R}} \mathrm{Re} > 2200 \tag{7}$$

Xia et al. [73] analyzed the heat transfer of latent thermal energy storage (LTES) system based on the effective packed bed model. The flow field is simplified as the flow through voids of a bed packed with PCMs particles. The random packing model is proposed for better simulation. The material properties and the thickness of encapsulation are two major factors for the heat transfer performance of a LTES bed.

The porosity is listed as:

$$\varepsilon_{\mathrm{r}} = \varepsilon_{\infty} \cdot \left(1 + \left(\frac{0.87}{\varepsilon_{\infty}} - 1 \right) \cdot e^{-5 \cdot \left(\frac{\frac{D}{2} - r}{d} \right)} \right) \tag{8}$$

$$\varepsilon_{3\mathrm{D}} = \frac{n_{3\mathrm{D}} \cdot \frac{4}{3} \cdot \pi \cdot \left(\frac{d}{2} \right)^3}{\pi \cdot \left(\frac{D}{2} \right)^2 \cdot H} \tag{9}$$

$$\varepsilon_{2\mathrm{D}} = \frac{n_{2\mathrm{D}} \cdot \pi \cdot \left(\frac{d}{2} \right)^3}{\pi \cdot \left(\frac{D}{2} \right)^2 \cdot H} \tag{10}$$

Izquierdo-Barrientos et al. [74] presented a dimensionless numerical model for the evolution of enthalpy with temperature, instead of constant phase change temperature assumption.

The dimensionless parameters include:

$$\widehat{T} = \frac{T - T_0}{T_{\max} - T_0} \tag{11}$$

$$\widehat{\theta} = \frac{\theta - T_0}{T_{\max} - T_0} \tag{12}$$

$$\widehat{\psi} = \frac{\psi - T_0}{T_{\max} - T_0} \tag{13}$$

$$\widehat{t} = t \cdot \frac{u}{H} \tag{14}$$

$$\widehat{x} = \frac{x}{H} \tag{15}$$

Modi and Perez-segarra [75] developed a one-dimensional numerical model for a single-tank thermocline thermal storage system in the concentrated solar power plant. The influence of types of heat transfer fluid, the temperature difference stored in HTF as well as the cycle cut-off on system performance is investigated. Two aspects are taken as criterion for comparison, that is, cyclic behavior of the system and the time required for equilibrium state attainment.

The heat transfer coefficient is expressed as:

$$h = \frac{6 \cdot (1-\varepsilon) \cdot k \cdot \left(2 + 1.1 \cdot \mathrm{Re}^{0.6} \cdot \mathrm{Pr}^{\frac{1}{3}}\right)}{D^2} \tag{16}$$

Opitz and Treffinger [76] developed a general heterogeneous model of heat transfer in packed beds. Lumped element formulation is implemented. The results are verified with two different experiments cited from references. No necessary to calibrate theoretical model with experiment results is reported.

The pressure drop for one layer of the packed bed is expressed as:

$$\Delta P = 150 \cdot \frac{(1-\varepsilon)^2}{\varepsilon^2} \cdot \frac{\eta}{d^2} \cdot w \cdot H + 1.75 \cdot \frac{(1-\varepsilon)}{\varepsilon^3} \cdot \frac{\rho}{d} \cdot w^2 \cdot H \tag{17}$$

The heat transfer is summarized as:

With correlation of Coutier and Farber:

$$h_{\mathrm{fs}} = \frac{700}{6 \cdot (1-\varepsilon)} \cdot \left(\frac{m}{A}\right)^{0.76} \cdot d^{0.24} \tag{18}$$

With correlation of Gnielinski:

$$Nu_{\mathrm{fs,i}} = f_{\mathrm{a}} \cdot \left(2 + \sqrt{(Nu_{\mathrm{lam,i}})^2 + (Nu_{\mathrm{turb,i}})^2}\right) \tag{19}$$

$$Nu_{\mathrm{lam,i}} = 0.644 \cdot \sqrt{\mathrm{Re}_{\mathrm{bed,i}}} \cdot \sqrt[3]{\mathrm{Pr}_{\mathrm{f,i}}} \tag{20}$$

$$Nu_{\mathrm{turb,i}} = \frac{0.037 \cdot (\mathrm{Re}_{\mathrm{bed,i}})^{0.8} \cdot \mathrm{Pr}_{\mathrm{f,i}}}{1 + 2.443 \cdot (\mathrm{Re}_{\mathrm{bed,i}})^{-0.1} \cdot \left((\mathrm{Pr}_{\mathrm{f,i}})^{\frac{2}{3}} - 1\right)} \tag{21}$$

$$f_{\mathrm{a}} = 1 + 1.5 \cdot (1-\varepsilon) \tag{22}$$

$$\frac{1}{h_{\mathrm{fs,p,i}}} = \frac{1 + \frac{Bi}{5}}{h_{\mathrm{fs,i}}} \tag{23}$$

$$Bi_{\mathrm{bed}} = h_{\mathrm{fs}} \cdot \frac{d_{\mathrm{p}}}{k_{\mathrm{bed}}} \tag{24}$$

Amin et al. [77] developed an effectiveness-NTU model of a thermal storage system with packed bed of encapsulated PCMs with the sphere shape. The two-dimensional representation is proposed to predict the heat transfer during phase change, comparing with one-dimensional phase change assumption in other configurations. A new definition of thermal resistance between HTF and PCMs is developed, taking the phase change process into consideration.

The heat transfer is expressed as:

$$Nu = \left(7 - 10 \cdot \xi + 5 \cdot \xi^2\right) \cdot \left(1 + 0.7 \cdot \mathrm{Re}^{0.2} \cdot \mathrm{Pr}^{\frac{1}{3}}\right) + \left(1.33 - 2.4 \cdot \xi + 1.2 \cdot \xi^2\right) \cdot \mathrm{Re}^{0.7} \cdot \mathrm{Pr}^{\frac{1}{3}} \quad (25)$$

Karthikeyan and Velraj [78] compared several mathematical models for numerical investigation of packed bed with encapsulated spherical PCMs. The enthalpy formulation technique is used to accommodate the phase change behavior of paraffin. Fully explicit finite difference method is adopted for solving numerical models. It is reported that the validity of model depends on the kind of HTF.

The governing equations are listed as:

For model 1:

$$\varepsilon \cdot \rho_\mathrm{f} \cdot A_\mathrm{c} \cdot L \cdot c_\mathrm{f} \cdot \left(\frac{\partial T_\mathrm{f}}{\partial t} + v_\mathrm{max} \cdot \frac{\partial T_\mathrm{f}}{\partial x}\right) = h_\mathrm{s} \cdot a_\mathrm{p} \cdot \left(T_\mathrm{p} - T_\mathrm{f}\right) \quad (26)$$

$$(1 - \varepsilon) \cdot \rho_\mathrm{p} \cdot A_\mathrm{c} \cdot L \cdot c_\mathrm{p} \cdot \left(\frac{\partial H_\mathrm{p}}{\partial t}\right) = h_\mathrm{s} \cdot a_\mathrm{p} \cdot \left(T_\mathrm{f} - T_\mathrm{p}\right) \quad (27)$$

For model 2:

$$\varepsilon \cdot \rho_\mathrm{f} \cdot A_\mathrm{c} \cdot L \cdot c_\mathrm{f} \cdot \left(\frac{\partial T_\mathrm{f}}{\partial t} + v_\mathrm{max} \cdot \frac{\partial T_\mathrm{f}}{\partial x}\right) = k_\mathrm{f} \cdot \frac{\partial^2 T_\mathrm{f}}{\partial x^2} + h_\mathrm{s} \cdot a_\mathrm{p} \cdot \left(T_\mathrm{p} - T_\mathrm{f}\right) \quad (28)$$

$$(1 - \varepsilon) \cdot \rho_\mathrm{p} \cdot A_\mathrm{c} \cdot L \cdot c_\mathrm{p} \cdot \left(\frac{\partial H_\mathrm{p}}{\partial t}\right) = k_\mathrm{p} \cdot \frac{\partial^2 T_\mathrm{p}}{\partial x^2} + h_\mathrm{s} \cdot a_\mathrm{p} \cdot \left(T_\mathrm{f} - T_\mathrm{p}\right) \quad (29)$$

For model 3:

$$\varepsilon \cdot \rho_\mathrm{f} \cdot A_\mathrm{c} \cdot L \cdot c_\mathrm{f} \cdot \left(\frac{\partial T_\mathrm{f}}{\partial t} + v_\mathrm{max} \cdot \frac{\partial T_\mathrm{f}}{\partial x}\right) = h_\mathrm{s} \cdot a_\mathrm{p} \cdot \left(T_\mathrm{p}\big|_{\mathrm{r}=\mathrm{r}_0} - T_\mathrm{f}\right) \quad (30)$$

$$\rho_\mathrm{p} \cdot \left(\frac{\partial H_\mathrm{p}}{\partial t}\right) = k_\mathrm{p} \cdot \frac{\partial^2 T_\mathrm{p}}{\partial r^2} + \frac{2}{r} \cdot k_\mathrm{p} \cdot \frac{\partial T_\mathrm{p}}{\partial r} \quad (31)$$

3.2. Numerical simulation

Pakrouh et al. [79] present a numerical investigation on geometric optimization of heat sinks. Paraffin is selected as PCMs and aluminum is adopted as materials for heat sink and fins. The optimization parameters include the number of fins, the height of fins and the thickness of fins as well as the base. Natural convection is also taken into consideration. It reported a complex relation between PCMs and the volume percentage of thermal conductivity enhancers (TCEs). Shmueli et al. [80] investigated numerically with melting of PCMs in a vertical cylindrical tube and compared with experiments. The model is based on enthalpy-porosity formulation. The effects of parameters, such as the term describing the mushy zone in the momentum equation and the pressure-velocity coupling as well as pressure discretization schemes, are examined. No difference between PISO and SIMPLE schemes is found, while there is considerable

difference between PRESTO and Body-Force-Weighted schemes. Local heat transfer and melting are compared and verified for numerical results. It is concluded that at the beginning of melting process, the heat transfer is mainly in the form of conduction in solid phase; while at the end of this process, the heat transfer is dominated by convection in liquid phase. Cascetta et al. [81] utilized FLUENT software to simulate the flow and heat transfer in an axisymmetric tank of cylindrical shape. Incompressible turbulent flow and fully developed forced convection is adopted in two-phase transient (LTNE-local thermal non-uniform) model to calculate the temperatures of fluid and solid phases. The porosity of filled bed is also considered variable in the radial direction and the thermal properties of both phases are related to temperature. The results agree well with experiments. Sciacovelli et al. [82] used enthalpy method to analyze the phase change phenomenon. Natural convection is neglected, due to the fully resolved fluid flow in the liquid phase. The evaluation of melting front as well as the temperature and velocity fields is studied in details. However, it is concluded that natural convection significantly affects the phase change process. Also in this paper, the effects of enhancement of thermal conductivity with the adoption of highly conductive nano-particles in PCMs are considered. Augment of thermal performance is found, due to the application of nano-particles. The melting time is reduced by 15% with 4% volume fraction of nano-particles. Similar results are also found for the heat transfer performance.

4. Conclusions

For the properties of PCMs under research, besides thermal conductivity and phase equilibrium, others such as supercooling [83], corrosion [84] and transportation [85] are also characterized and discussed. However, less attention has been paid on the systematic discussion. This is partly due to the diverse results in different research groups, and sometimes the conclusions are contradictory. For instance, Teng et al. [86] reported the advantage of multi-wall carbon nanotubes (MWCNTs) over graphite for effective enhancement of thermal conductivity. However, Choi et al. [87] reported the contrary conclusion. Another case is the reported results of the same method and the same materials at different ages or by different groups are sometimes at significant variations. For instance, the heat of fusion for Paraffin Wax is reported as 173.6 kJ/kg [88] and 266 kJ/kg [89]; the melting temperature of myristic acid is reported as 49–51°C [90] and 58°C [91].

One of the reasons lies on the lackness of uniform standard or detailed information of preparation, manufacture and raw materials as well as the diversified methods of properties measurements. As far as thermal conductivity is concerned, researchers can utilize stationary and non-stationary methods to measure. Even in detailed non-stationary measurement, point-, linear- or surface- heating source is available for choice. Therefore, it seems difficult to collect the results in reference to obtain the regular of physical properties for theoretical estimation or analysis.

In this section, we mainly introduce the progress of property enhancement of PCMs and performance improvement of LHS unit. The detailed information of reported results is referred

to cited references. It is found that lots of work has been done in the past decades and great progress has been made. However, there is still some weakness in research. For PCMs, most research is based on experimental measurement of properties, and less attention has been paid on the regular summary for theoretical estimation in the future or optimal design of composite material as well as energy storage unit. As far as LHS unit is concerned, it is the opposite condition, where most research is based on numerical analysis and less experimental research is conducted. This may lead to the deviation of the performance of LHS unit in application from the designed values, especially when the properties of PCMs as well as its composite are still not clear in details. What is more, the lackness of uniform standard and detailed report on information of preparation, manufacture and raw materials makes it difficult to collect the results of different groups and different ages all together.

Acknowledgements

This work is supported by Natural Science Foundation of China (51306023) and Advanced Catalysis and Green Manufacturing Collaborative Innovation Center.

Conflict of interest

None declared.

Author details

Cheng Wang[1]* and Ye Zhu[2]

*Address all correspondence to: wangcheng3756@163.com

1 Jiangsu Provincial Key Laboratory of Oil and Gas Storage and Transportation Technology, Changzhou University, Changzhou, China

2 Jiangsu Provincial Key Laboratory of Fine Petrochemical Engineering, Changzhou University, Changzhou, China

References

[1] Ibrahim NI, Al-Sulaiman FA, Rahman S, Yilbas BS, Sahin AZ. Heat transfer enhancement of phase change materials for thermal energy storage applications: A critical review. Renewable and Sustainable Energy Reviews. 2017;**74**:26-50

[2] Zhao CY, Wu ZG. Heat transfer enhancement of high temperature thermal energy storage using metal foams and expanded graphite. Solar Energy Materials and Solar Cells. 2011; **95**:636-643

[3] Siaphush A, O'Brien J, Crepeau J. Phase change heat transfer enhancement using copper porous foam. Journal of Heat Transfer. 2008;**130**:082301

[4] Yin H, Gao X, Ding J, Zhang Z. Experimental research on heat transfer mechanism of heat sink with composite phase change materials. Energy Conversion and Management. 2008; **49**:1740-1746

[5] Gao L, Zhao J, An Q, Zhao D, Meng F, Liu X. Experiments on thermal performance of erythritol/expanded graphite in a direct contact thermal energy storage container. Applied Thermal Engineering. 2017;**113**:858-866

[6] Lafdi K, Mesalhy O, Shaikh S. Experimental study on the influence of foam porosity and pore size on the melting of phase change materials. Journal of Applied Physics. 2007;**102**: 083549

[7] Zhong Y, Guo Q, Li S, Shi J, Liu L. Heat transfer enhancement of paraffin wax using graphite foam for thermal energy storage. Solar Energy Materaisl and Solar Cells. 2010; **94**:1011-1014

[8] Wu ZG, Zhao CY. Experimental investigations of porous materials in high temperature thermal energy storage systems. Solar Energy. 2011;**85**:1371-1380

[9] Zhang P, Meng ZN, Zhu H, Wang YL, Peng SP. Melting heat transfer characteristics of a composite phase change material fabricated by paraffin and metal foam. Applied Energy. 2017;**185**:1971-1983

[10] Gulfam R, Zhu W, Li X, Cheema II, Sheng P, Zhao G, Deng Y. Design, fabrication and numerical analysis of compact thermal management system integrated with composite phase change material and thermal bridge. Energy Conversion and Management. 2018; **156**:25-33

[11] Oya T, Nomura T, Okinaka N, Akiyama T. Phase change composite based on porous nickel and erythritol. Applied Thermal Engineering. 2012;**40**:373-377

[12] Nomura T, Zhu C, Nan S, Tabuchi K, Wang S, Akiyama T. High thermal conductivity phase change composite with a metal-stabilized carbon-fiber network. Applied Energy. 2016;**179**:1-6

[13] Nomura T, Okinaka N, Akiyama T. Impregnation of porous material with phase change material for thermal energy storage. Materials Chemistry and Physics. 2009;**115**:846-850

[14] Li Y, Guo B, Huang G, Kubo S, Shu P. Characterization and thermal performance of nitrate mixture/SiC ceramic honeycomb composite phase change materials for thermal energy storage. Applied Thermal Engineering. 2015;**81**:193-197

[15] Fan L, Zhu Z, Liu M. A similarity solution to unidirectional solidification of nano-enhanced phase change materials (NePCM) considering the mushy region effect. International Journal of Heat and Mass Transfer. 2015;**86**:478-481

[16] Qi G, Yang J, Bao R, Liu Z, Yang W, Xie B, Yang M. Enhanced comprehensive performance of polyethylene glycol based phase change material with hybrid graphene nanomaterials for thermal energy storage. Carbon. 2015;**88**:196-205

[17] Tao YB, Lin CH, He YL. Preparation and thermal properties characterization of carbonate salt/carbon nanomaterial composite phase change material. Energy Conversion and Management. 2015;**97**:103-110

[18] Kim S, Drzal LT. High latent heat storage and high thermal conductive phase change materials using exfoliated expanded nanoplatelets. Solar Energy Materials and Solar Cells. 2009;**93**:136-142

[19] Shi J, Ger M, Liu Y, Fan Y, Wen N, Li C, Nenwen P. Improving the thermal conductivity and shape-stabilization of phase change materials using nanographite additives. Carbon. 2013;**51**:365-372

[20] Zhang H, Rindt CCM, Smeulders DMJ, Nedea SV. Nanoscale heat transfer in carbon nanotubes - sugar alcohol composite as heat storage materials. Journal of Physical Chemistry C. 2016;**120**:21915-21924

[21] Samimi F, Babapoor A, Azizi M, Karimi G. Thermal management analysis of a Li-ion battery cell using phase change material loaded with carbon fibers. Energy. 2016;**96**:355-371

[22] Nomura T, Tabuchi K, Zhu C, Sheng N, Wang S, Akiyama T. High thermal conductivity phase change composite with percolating carbon fiber network. Applied Energy. 2015;**154**: 678-685

[23] Kibria MA, Anisur MR, Mahfuz MH, Saidur R, Metselaar IHSC. A review on thermophysical properties of nanoparticle dispersed phase change materials. Energy Conversion and Management. 2015;**95**:69-89

[24] Zhang XL, Chen XD, Zhao QZ, Ding L. The research on the dispersion effect improvement for nano-copper in erythritol. Materials Research Innovations. 2015;**19**(S1):9-13

[25] Zhichao L, Qiang Z, Gaohui W. Preparation and enhanced heat capacity of nano-titania doped erythritol as phase change material. International Journal of Heat and Mass Transfer. 2015;**80**:653-659

[26] Mettawee ES, Assassa GMR. Thermal conductivity enhancement in a latent heat storage system. Solar Energy. 2007;**81**:839-845

[27] Motahar S, Nikkam N, Alemrajabi AA, Khodabandeh R, Toprak MS, Muhammed M. Experimental investigation on thermal and rheological properties of n-octadecane with dispersed TiO_2 nanoparticles. International Communications in Heat and Mass Transfer. 2014;**59**:68-74

[28] Wang J, Xie H, Xin Z, Li Y, Chen L. Enhancing thermal conductivity of palmitic acid based phase change materials with carbon nanotubes as fillers. Solar Energy. 2010;**84**:339-344

[29] Zeng JL, Cao Z, Yang DW, Xu F, Sun LX, Zhang XF, Zhang L. Effects of MWNTs on phase change enthalpy and thermal conductivity of a solid-liquid organic PCM. Journal of Thermal Analysis and Calorimetry. 2009;**95**:507-512

[30] Khyad A, Samrani H, Bargach MN, Tadili R. Energy storage with PCMs: Experimental analysis of paraffin's phase change phenomenon & improvement of its properties. Journal of Material & Environment Science. 2016;**7**:2551-2560

[31] Sparrow EM, Larson ED, Ramsey JW. Freezing on a finned tubed for either conduction-controlled or natural-convection-controlled heat transfer. International Journal of Heat and Mass Transfer. 1981;**24**:273-284

[32] Tao YB, He YL, Qu ZG. Numerical study on performance of molten salt phase change thermal energy storage system with enhanced tubes. Solar Energy. 2012;**86**:1155-1163

[33] Velraj R, Seeniraj RV, Hafner B, Faber C, Schwarzer K. Experimental analysis and numerical modelling of inward solidification on a finned vertical tube for a latent heat storage unit. Solar Energy. 1997;**60**:281-290

[34] Zhao D, Tan G. Numerical analysis of a shell-and-tube latent heat storage unit with fins for air-conditioning application. Applied Energy. 2015;**138**:381-392

[35] Erek A, Ilken Z, Acar MA. Experimental and numerical investigation of thermal energy storage with a finned tube. International Journal of Energy Research. 2005;**29**:283-301

[36] Liu Z, Sun X, Ma C. Experimental investigations on the characteristics of melting processes of stearic acid in an annulus and its thermal conductivity enhancement by fins. Energy Conversion and Management. 2005;**46**:959-969

[37] Hosseini MJ, Rahimi M, Bahrampoury R. Thermal analysis of PCM containing heat exchanger enhanced with normal annular fines. Mechanical Science. 2015;**6**:221-234

[38] Gharebaghi M, Sezai I. Enhancement of heat transfer in latent heat storage modules with internal fins. Numerical Heat Transfer, Part A: Application. 2007;**53**:749-765

[39] Sharifi N, Bergman TL, Faghri A. Enhancement of PCM melting in enclosures with horizontally-finned internal surfaces. International Journal of Heat and Mass Transfer. 2011;**54**:4182-4192

[40] Mahmoud S, Tang A, Toh C, Al-dadah R, Soo SL. Experimental investigation of inserts configurations and PCM type on the thermal performance of PCM based heat sinks. Applied Energy. 2013;**112**:1349-1356

[41] Arshad A, Ali HM, Ali M, Manzoor S. Thermal performance of phase change material (PCM) based pin-finned heat sinks for electronics devices: Effect of pin thickness and PCM volume fraction. Applied Thermal Engineering. 2017;**112**:143-155

[42] Rahimi M, Ranjbar AA, Ganji DD, Sedighi K, Hosseini MJ. Experimental investigation of phase change inside a finned-tube heat exchanger. Journal of Engineering, 2014. 641954

[43] Fang M, Chen G. Effects of different multiple PCMs on the performance of a latent thermal energy storage system. Applied Thermal Engineering. 2007;**27**:994-1000

[44] Wang J, Chen G, Jiang H. Theoretical study on a novel phase change process. International Journal of Energy Research. 1999;**23**:287-294

[45] Cui H, Yuan X, Hou X. Thermal performance analysis for a heat receiver using multiple phase change materials. Applied Thermal Engineering. 2003;**23**:2353-2361

[46] Zhipei H, Li A, Gao R, Yin H. Enhanced heat transfer for PCM melting in the frustum-shaped unit with multiple PCMs. Journal of Thermal Analysis and Calorimetry. 2015;**120**: 1407-1416

[47] Kurnia JC, Sasmito AP, Jangam SV, Mujumdar AS. Improved design for heat transfer performance of a novel phase change material (PCM) thermal energy storage (TES). Applied Thermal Engineering. 2013;**50**:896-907

[48] Tao YB, He YL, Liu YK, Tao WQ. Performance optimization of two-stage latent heat storage unit based on entransy theory. International Journal of Heat and Mass Transfer. 2014;**77**:695-703

[49] Xu HJ, Zhao CY. Thermodynamic analysis and optimization of cascaded latent heat storage system for energy efficient utilization. Energy. 2015;**90**:1662-1673

[50] Wang C, Zhu Y. Optimization of double-stage latent heat storage unit in whole cycle with entransy analysis. International Journal of Heat and Mass Transfer. 2017;**114**:1013-1024

[51] Wang C, Zhu Y. Entransy analysis on boiler air pre-heater with multi-stage LHS unit. Applied Thermal Engineering. 2018;**130**:1139-1146

[52] Wang C, Zhu Y. Entransy analysis on optimization of a double-stage latent heat storage unit with the consideration of an unequal separation. Energy. 2018;**148**:386-396

[53] Jacob R, Bruno F. Review on shell materials used in the encapsulation of phase change materials for high temperature thermal energy storage. Renewable and Sustainable Energy Reviews. 2015;**48**:79-87

[54] Liu C, Rao Z, Zhao J, Huo Y, Li Y. Review on nanoencapsulated phase change materials: Preparation, characterization and heat transfer enhancement. Nano Energy. 2015;**13**:814-826

[55] Gunasekara SN, Martin V, Chiu JN. Phase equilibrium in the design of phase change materials for thermal energy storage: State-of-the-art. Renewable and Sustainable Energy Reviews. 2017;**73**:558-581

[56] Liu S, Li Y, Zhang Y. Review on heat transfer mechanisms and characteristics in encapsulated PCMs. Heat Transfer Engineering. 2015;**36**:880-901

[57] Jamekhorshid A, Sadrameli SM, Farid M. A review of microencapsulation methods of phase change materials (PCMs) as a thermal energy storage (TES) medium. Renewable and Sustainable Energy Reviews. 2014;**31**:531-542

[58] Weiguang S, Jo D, Kokogiannakis G. Review of solid-liquid phase change materials and their encapsulation technologies. Renewable and Sustainable Energy Reviews. 2015;**48**: 373-391

[59] Milian YE, Gutierrez A, Grageda M, Ushak S. A review on encapsulation techniques for inorganic phase change materials and the influence on their thermophysical properties. Renewable and Sustainable Energy Reviews. 2017;**73**:983-999

[60] Ma B, Li J, Zhe X, Peng Z. Fe-shell/Cu-core encapsulated metallic phase change materials prepared by aerodynamic levitation method. Applied Energy. 2014;**132**:568-574

[61] Chen Z, Fei Y, Zeng X, Zhang Z. Preparation, characterization and thermal properties of nanocapsules containing phase change materials n-dodecanol by miniemulsion polymerization with polymerizable emulsifier. Applied Energy. 2012;**91**:7-12

[62] Yang W, Yue Z, Baoxing X. A hybrid elastomeric foam-core/solid-shell spherical structure of enhanced energy absorption performance. International Journal of Solids and Structures. 2016;**92-93**:17-28

[63] Shabgard H, Robak CW, Bergman TL, Faghri A. Heat transfer and exergy analysis of cascaded latent heat storage with gravity-assisted heat pipes for concentrating solar power applications. Solar Energy. 2012;**86**:816-830

[64] Shabgard H, Faghri A, Bergman TL, Andraka CE. Numerical simulation of heat pipe-assisted latent heat thermal energy storage unit for dish-stirling systems. Journal of Solar Energy Engineering. 2013;**136**:021025

[65] Robak CW, Bergman TL, Faghri A. Enhancement of latent heat storage using embedded heat pipes. International Journal of Heat and Mass Transfer. 2011;**54**:3476-3484

[66] Shabgard H, Bergman TL, Sharifi N, Faghri A. High temperature latent heat thermal energy storage using heat pipes. International Journal of Heat and Mass Transfer. 2010; **53**:2979-2988

[67] Nithyanandam K, Pitchumani R. Computational studies on a latent thermal energy storage system with integral heat pipes for concentrating solar power. Applied Energy. 2013; **103**:400-415

[68] Nithyanandam K, Pitchumani R. Computational modeling of dynamic response of a latent thermal energy storage system with embedded heat pipes. Journal of Solar Energy Engineering. 2013;**136**:011010

[69] Jung EG, Boo JH. Thermal analytical model of latent thermal storage with heat pipe exchanger for concentrated solar power. Solar Energy. 2014;**102**:318-332

[70] Khalifa A, Tan L, Date A, Akbarzadeh A. A numerical and experimental study of solidification around axially finned heat pipes for high temperature latent heat thermal energy storage units. Applied Thermal Engineering. 2014;**70**:609-619

[71] Nithyanandam K, Pitchumani R. Computational studies on metal foam and heat pipe enhanced latent thermal energy storage. Journal of Heat Transfer. 2014;**136**:051503

[72] Esen M, Durmus A, Durmus A. Geometric design of solar-aided latent heat store depending on various parameters and phase change materials. Solar Energy. 1998;**62**:19-28

[73] Xia L, Zhang P, Wang RZ. Numerical heat transfer analysis of the packed bed latent heat storage system based on an effective packed bed model. Energy. 2010;**35**:2022-2032

[74] Izquierdo-Barrientos MA, Sobrino C, Almendros-Ibanez JA. Modeling and experiments of energy storage in a packed bed with PCM. International Journal of Multiphase Flow. 2016; **89**:1-9

[75] Modi A, Perez-segarra CD. Thermocline thermal storage systems for concentrated solar power plants: one-dimensional numerical model and comparative analysis. Solar Energy. 2014;**100**:84-93

[76] Opitz F, Treffinger P. Packed bed thermal energy storage model—Generalized approach and experimental validation. Applied Thermal Engineering. 2014;**73**:245-252

[77] Amin NAM, Belusko M, Bruno F. An effectiveness-NTU model of a packed bed PCM thermal storage system. Applied Energy. 2014;**134**:356-362

[78] Karthikeyan S, Velraj R. Numerical investigation of packed bed storage unit filled with PCM encapsulated spherical containers—A comparison between various mathematical models. International Journal of Thermal Sciences. 2012;**60**:153-160

[79] Pakrouh R, Hosseini MJ, Ranjbar AA, Bahrampoury R. A numerical method for PCM-based pin fin heat sinks optimization. Energy Conversion and Management. 2015;**103**:542-552

[80] Shnueli H, Ziskind G, Letan R. Melting in a vertical cylindrical tube: Numerical investigation and comparison with experiments. International Journal of Heat and Mass Transfer. 2010;**53**:4082-4091

[81] Cascetta M, Cau G, Puddu P, Serra F. A comparison between CFD simulation and experimental investigation of a packed-bed thermal energy storage system. Applied Thermal Engineering. 2016;**98**:1263-1272

[82] Sciacovelli A, Colella F, Verda V. Melting of PCM in a thermal energy storage unit: Numerical investigation and effect of nanoparticle enhancement. International Journal of Energy Research. 2013;**37**:1610-1623

[83] Safari A, Saidur R, Sulaiman FA, Yan X, Dong J. A review on supercooling of phase change materials in thermal energy storage systems. Renewable and Sustainable Energy Reviews. 2017;**70**:905-919

[84] Vasu A, Hagos FY, Noor MM, Mamat R, Azmi WH, Abdullah AA, Ibrahim TK. Corrosion effect of phase change materials in solar thermal energy storage application. Renewable and Sustainable Energy Reviews. 2017;**76**:19-33

[85] Tay NHS, Liu M, Belusko M, Bruno F. Review on transportable phase change material in thermal energy storage systems. Renewable and Sustainable Energy Reviews. 2017;**75**: 264-277

[86] Teng T, Cheng C, Cheng C. Performance assessment of heat storage by phase change materials containing MWCNTs and graphite. Applied Thermal Engineering. 2013;**50**:637-644

[87] Da HC, Lee J, Hong H, Kang YT. Thermal conductivity and heat transfer performance enhancement of phase change materials (PCM) containing carbon additives for heat storage application. International Journal of Refrigeration. 2014;**42**:112-120

[88] Dincer I, Rosen MA. Thermal energy storage: systems and applications. 2nd ed. John Wiley & Sons; 2011

[89] Heckenkamp J. Baumann H. Sonderdruck aus Nachrichten: Latentwaermespeicher; 1997

[90] Sari A, Kaygusuz K. Thermal performance of myristic acid as a phase change material for energy storage application. Renewable Energy. 2001;**24**:303-317

[91] Lane GA. Low temperature heat storage with phase change materials. International Journal of Ambient Energy. 1980;**1**:155-168

Section 3

Thermal Stability of Phase Change Material

Chapter 3

Phase Change Materials and Their Applications

Manish K. Rathod

Additional information is available at the end of the chapter

http://dx.doi.org/10.5772/intechopen.75923

Abstract

Along with the heat transfer mechanism for the development of a latent heat storage unit (LHSU), the choice of the phase change material (PCM) plays an important role. The enviable thermo-physical, kinetic, and chemical properties of PCM with the economy is an essential criterion for efficient thermo-economical LHSU. The most important criteria that have limited widespread use of LHSU are the useful life of phase change materials. For long term performance of LHSU, the PCM used in the system should be thermally stable and reliable. It does not deteriorate its own properties, especially latent heat and melting point after a repeated number of thermal cycles. Thus an exhaustive literature survey is carried out for different types of PCMs used. The primary objective of this chapter is to carry out a critical review of thermal stability of different group of PCM especially for low temperature applications. Further, an extensive list of different PCMs which are undergone thermal cyclic tests by different researchers is prepared. This information is towards the selection of reliable PCM for latent heat storage unit.

Keywords: thermal stability, thermal cycles, differential scanning calorimeter, phase change material, latent heat

1. Introduction

Energy plays a major role in the economic prosperity and the technological competitiveness of the nation. Rapid development has led to huge demand for energy. The resource augmentation and growth in energy supply have failed to meet the ever increasing demands exerted by the multiplying population, rapid urbanization and progressing economy. In order to conserve energy and reduce dependency on fossil fuels and also to reduce the greenhouse gas emission, it is essential to develop efficient and inexpensive energy storage system [1]. Energy storage systems eliminate shortage between supply and demand and also exhilarate energy system performance and reliability. The energy storage can substantially reduce the

total energy consumption when integrated to sustainable energy sources such as solar energy, wind energy, waste heat recovery, biogas etc. And hence, conserve indigenous conventional energy sources. The thermal energy storage (TES) is also popular now and acts as a crucial aspect in engineering applications. TES may comprise sensible storage systems (energy storage by single phase heating and cooling), latent heat storage (energy storage by two phase melting and solidification) and thermochemical heat storage (energy storage by reversible chemical interactions between reactive components). The sensible heat storage (SHS) systems are widely used for low temperature solar thermal applications. However, SHS systems require a large storage volume for small temperature swing. The latent heat storage (LHS) systems stand out due to high storage density and nearly isothermal phase change [1–4].

The thermal energy storage materials used for LHS systems are also known as phase change materials (PCM). Telkes and Raymond [6] are pioneers to study PCM. A wide range of phase change materials with myriad melting points have been identified and studied exhaustively. These PCMs can be categorized as organic (paraffins and fatty acids), inorganics (salt hydrates and metallic) and eutectic combination of organic and/or inorganic materials. A detailed classification of PCM for latent heat storage applications is given in **Figure 1**.

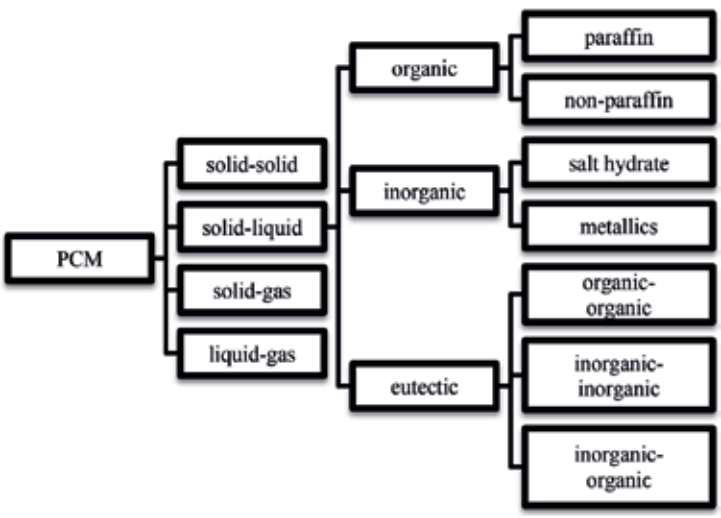

Figure 1. Classification of PCMs [5].

Figure 2. Phase-change materials in their original states, (a) paraffin wax, (b) stearic acid, (c) sodium hydroxide.

Figure 2 shows a sample of paraffin wax (paraffin), stearic acid (fatty acid) and sodium hydroxide (salt hydrate) in their original states, respectively.

2. Properties of PCM

Successful utilization of the latent heat storage unit (LHSU) depends considerably on the selection of the PCM, which plays an important role in development of LHSU. The feasibility of using a particular PCM for an LHSU is based on some desirable thermo-physical, kinetic, and chemical properties of the PCM. These desirable thermal, physical, kinetic, chemical and economical properties of PCM are listed below in **Table 1**.

As no single material can have all the required properties for an ideal thermal storage media, one has to use the available material and try to make up for the poor physical properties by an appropriate system design. Thus, selection of appropriate PCM is a challenge to the researchers.

Thermal properties	• Suitable melting point for particular application
	• High latent heat of fusion per unit volume
	• High thermal conductivity of solid and liquid phases for better heat transfer
	• Higher specific heat for additional sensible heat storage
Physical properties	• Favorable phase equilibrium
	• High density for smaller container volume
	• Small volume change during phase transition
	• Low vapor pressure to reduce the containment problem
	• Reproducibility in the congruent during entire thermal cycle
Kinetic properties	• Little or no supercooling during freezing (Supercooling of more than a few degrees interferes with proper heat extraction)
	• High rates of nucleation and high rate of crystal growth. i.e., the melt should crystallize at its thermodynamic freezing point.
	• Effective heat transfer, especially at isothermal conditions
Chemical properties	• No degradation after a number of freeze/melt cycle
	• Non-corrosiveness to the construction material
	• No chemical decomposition
	• No toxicity
	• Nonpoisonous, non-flammable, non-polluting and non-explosive
Economic criteria	• Available in plenty
	• Inexpensive
	• Ease recycling and treatment

Table 1. Desired properties of PCM [5, 7–10].

3. Drawbacks of PCM

The commercialization of LHSU is found to be limited due to lack of desirable thermo-physical properties. The low thermal conductivity of PCM, variation in thermo-physical properties of PCMs under extended cycles, phase segregation, sub cooling, incongruent melting, volume change and high cost are primary factors to restrict efficient performance of LHSU. The major drawback of LHSU is the lower thermal conductivity and thermal stability of the PCM. This is typically between 0.15 and 0.3 W/mK for organic materials and between 0.4 and 0.7 W/mK for salt hydrates [11]. The effect of the lower value of conductivity is reflected during energy retrieval or withdrawal with an appreciable temperature drop during the process. As a result, the rate of phase change process (melting/solidification of PCM) has not been up to the expected level. In a nutshell, adequate amount of energy may be available, but the system may not be able to use it at the required rate.

Further, the selection of using phase change material in any latent energy storage system is based on desirable thermo-physical, kinetic, and chemical properties in addition to economic criteria. However, each class of PCM has its own characteristics, applications, advantages, and limitations. As no single material can have all the required properties for an ideal thermal storage media, one has to optimize between the desired thermal performances and the cost. The economic criterion for employing a PCM in a system depends on the life and cost of the storage material. Hence, in order to ensure long term performance and economic feasibility of latent heat storage systems a comprehensive knowledge of thermal stability of the PCMs as functions of the repeated number of thermal cycles is essential.

4. Thermal stability of PCM

The PCMs may degrade with repetition of storage cycles. A large degradation in terms of thermo-physical properties with time is not desirable for any PCM. If it is thermally, chemically and physically stable after a repeated number of thermal cycles of operation, then PCM is said to be reliable. It does not deteriorate its own properties, especially latent heat and melting point after a repeated number of thermal cycles. A PCM is thermally stable for latent heat storage applications if it ensures negligible change in the melting point and latent heat of fusion after a large number of thermal cycles of operation. The commercial grade PCMs are widely preferred for the latent heat storage system due to large scale availability and low cost. However, it has always been noted that the thermo-physical properties and behavior of commercial grade materials are found to be very different from those quoted in the literature for laboratory grade materials (purity more than 99%). The influence of number of thermal cycles on the melting temperature and latent heat of fusion for commercial grade PCMs is thus required to be evaluated before their selection for a particular application.

Thus, the thermal stability test of PCMs should be performed prior to its actual applications. The previous literature addresses preparation, leakage, thermal conductivity and thermal storage properties of PCMs exhaustively. However, the reports on the thermal stability and/or

reliability of PCMs are found to be relatively inadequate. Till now, two major review papers are found in the literatures which emphasize the importance of thermal stability. Rathod and Banerjee [5] presents lists of PCMs for which thermal cycling test was carried out by different researchers and reported in the literature. Ferrer et al. [12] also presents a list of different PCMs undergone thermal cycling test. They also focus on the methodologies used by the different researchers, along with the equipment used and the analytical conditions in which the tests were carried out. Thus a lucid review of different low temperature PCMs for which thermal stability tests were carried out and reported in the literature is presented here.

4.1. Thermal stability test

A LHSU integrated with solar thermal systems undergo at least one melt/freeze thermal cycle a day, also known as normal cycle. This thermal cycle test can be established using different equipment like thermostatic chamber/bath, thermal bath, electric hot plate, constant temperature oven, etc. Other more specific equipment for thermal cycle test is thermal cycler which is most commonly used in biomedical applications [12]. Such thermal cycle tests carried out under controlled conditions in the laboratory are also known as accelerated thermal cycle tests [13, 14]. A small quantity sample of tested PCM is withdrawn after each specified number of thermal cycles for measuring the thermo-physical properties i.e. melting point and latent heat of fusion of the PCM.

The differential scanning calorimeter (DSC) is widely used in the laboratory to measure the melting temperature and heat of fusion of PCM. DSC works on a thermo-analytical principle. In this technique, the difference in the amount of heat required to raise the temperature of a sample and a reference is obtained as a function of temperature. During this process, it is required to maintain nearly the same temperature of the sample and reference. The heat capacity over the range of temperatures of a reference sample should be well-defined in prior. The alumina (Al_2O_3) is most recommended reference material for DSC analysis of PCM [9].

During DSC analysis, heat is supplied to both the sample and reference material. The heat is provided in such a manner that the temperature of the sample and reference material is maintained constant. When the sample undergoes a physical transformation such as phase transitions, more or less amount of heat will be required by the sample than the reference material for maintaining the same temperature. The requirement of less or more heat flow to the sample depends on whether the process is exothermic or endothermic [15–17]. By observing the difference in heat flow between the sample and reference, the amount of heat absorbed or released during such transitions is established by DSC. A plot between heat flow and temperature, known as DSC curve, is then drawn. Latent heat of fusion is calculated using the area under the peak of that curve. The phase transition temperature is taken as the onset obtained by line fitting of the rising part of the peak. The phase transition range is calculated between onset temperature and temperature corresponding to the peak of the curve. This range is commonly known as the "mushy zone" during which the PCM first softens and then melts. In this way the melting point and latent heat of fusion can be obtained with the use of DSC. The observed changes in these properties after a number of repeated thermal cycles can establish the stability of the PCM.

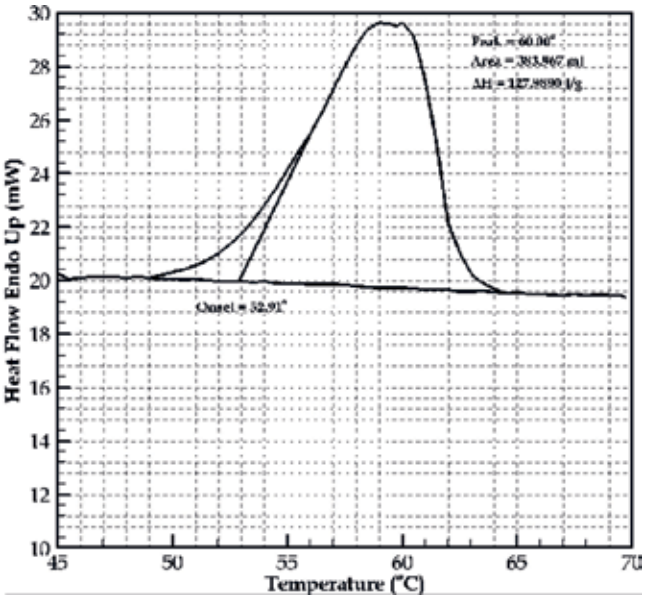

Figure 3. DSC measurement of the latent heat of fusion and the melting temperature of paraffin [18].

Figure 3 shows the DSC curve for a sample PCM, i.e. paraffin wax. The obtained temperature range of paraffin is 52.9–60.0°C. As area under the curve is 383.967 mJ and mass of sample is 3 mg, latent heat of fusion is 127.989 J/g. In order to analyze the changes in latent heat of fusion and phase transition temperature, a relative percentage difference is obtained after every specified thermal cycle, i.e. 50th or 100th. The relative percentage difference (RPD) of any property *i* of the PCM at any number of cycles *n* and the 0th cycle may be defined as [19]:

$$RPD = \frac{X_{n,i} - X_{0,i}}{X_{0,i}} \times 100(\%) \tag{1}$$

where $X_{n,i}$ denotes to the values of onset and peak temperatures and the latent heat of the PCM after n cycles and $X_{0,i}$ are the values of these quantities at 0th cycle. A critical review is carried out for thermal stability of different group of PCM with number of thermal cycles.

5. Thermal stability of PCM: a review

The thermal stability test carried out by various researchers on different groups of PCMs is discussed in this section.

5.1. Organic PCMs

This class of materials covers the wide range of melting temperature, i.e. between 0°C and about 200°C. The most of organic PCMs are not stable at higher temperatures because of the

covalent bonds. In most cases, the density of organic PCM is lesser than that of inorganic materials, i.e., less than 10^3 kg/m^3 [10]. Therefore, organic materials usually have smaller latent heat of fusion per volume than inorganic materials. Merits and demerits of the organic PCMs are as follows [5, 8].

Merits

- Available in large temperature range
- High latent heat of fusion
- Less supercooling (also called self-nucleation)
- Melt and freeze repeatedly without phase segregation
- Congruent phase transition process
- High thermal stability
- Non-corrosive

Demerits

- Lower thermal conductivity inherently
- Lower density of material
- Least compatible with plastic containments
- Combustible
- Costly

Organic PCMs are further divided in the group of paraffins and non-paraffins.

5.1.1. Paraffins

The natural paraffins are a mixture of pure alkanes, which have quite a wide range of the phase change temperature. The chemical formula of normal paraffins is C_nH_{2n+2}. They are straight chain saturated hydrocarbons with melting temperature range from 23 to 67°C. The chemical structure of paraffins is as shown in the **Figure 4**.

Paraffin wax is the most commonly used commercial organic heat storage PCM. Their volume increase upon melting is in the order of 10 vol.%. However, it is less critical because paraffins build up smaller forces upon expansion as they are softer. Paraffins are insoluble in water. They do not react with most common chemical reagents [10]. Many researchers have reported that paraffins are favorable because they are with the high heat of fusion, less supercooling and stable behavior. Paraffins are comparatively less costly and widely available. These PCMs are ecologically harmless and non-toxic [27, 28]. A list of paraffins studied by different researchers for stability test is given in **Table 2**. It can be observed that majority

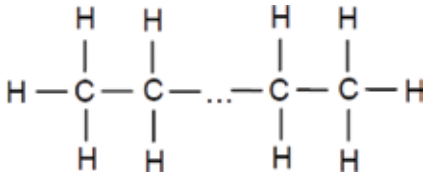

Figure 4. Chemical structure of paraffins.

Sr. no.	PCMs	Thermal cycles	Reference
1.	Paraffin (70 wt%) + Polypropylene (30 wt%)	3000	Alkan et al. [20]
2.	Paraffin ($C_{22.2}H_{44.1}$) (technical grade)	900	Hadjieva et al. [21]
3.	Paraffin ($C_{23.2}H_{48.4}$) (technical grade)	900	Hadjieva et al. [21]
4.	Paraffin wax 53 (commercial grade)	300	Sharma et al. [14]
		1500	Sharma et al. [22]
		1000	Silakhori et al. [23]
5.	Paraffin wax 54	1500	Shukla et al. [24]
6.	Paraffin wax 58–60	600	Shukla et al. [24]
7.	Paraffin wax 60–62	600	Shukla et al. [24]
8.	n-heptadecane/Poly methyl methacrylate ($C_{17}H_{36}$)	5000	Sari et al. [25]
9.	n-eicosane (C20)	1000	Karaipekli et al. [26]

Table 2. Thermal cycled paraffins.

of paraffins which is tested for thermal cycles are with melting temperature in the range of 45–60°C. Further, it noticed from the literature that paraffins do not degrade in their thermal properties even after number of thermal cycles.

5.1.2. Non-paraffins

Non-paraffins are the most studied and favorable PCMs for the researchers. These organic materials can be further categorized in subgroups of fatty acids and other non-paraffin organics (i.e., esters, alcohol, glycols, etc.). Due to the availability in suitable phase change temperature and high heat of fusion, fatty acids are the most potential PCM among all non-paraffins. A fatty acid is characterized by the formula $CH_3(CH_2)_{2n}COOH$.The chemical structure of fatty acid is shown in **Figure 5**. Fatty acids are easily producible from common vegetable and animal oils and thus provide an assurance of continuous supply despite the shortage of fuel sources [29–33]. The fatty acids are thermally stable after repeated melting/freezing cycles because they consist of only one component there cannot be phase separation. **Table 3** provides a list of non-paraffins studied for thermal stability.

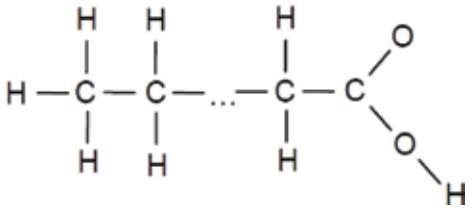

Figure 5. Chemical structure of fatty acid.

5.2. Thermal stability of inorganic PCMs

Inorganic materials are also available in a wide range of temperature. Inorganic materials usually have similar latent heat of fusion per mass compared to organic materials. However, latent heat of fusion per volume is higher due to their high density. Merits and demerits of the inorganic PCMs are as follows [5, 8].

Merits

- High volumetric latent heat storage capacity
- Sharp melting point
- Low vapor pressure in the melt state
- High thermal conductivity
- Relatively low volume change
- Noncorrosive, nonreactive and nonflammable
- Better compatibility with the conventional construction materials
- Low cost and readily available

Demerits

- Supercooling
- Low degree of nucleation
- Dehydration occurs during the phase change process
- Compatibility with some building materials is limited
- Corrosive with some metals
- Slightly toxic in nature

The family of inorganic materials includes salt hydrates and metallic PCMs.

Sr. no.	PCM	Thermal cycles	Reference
1.	Acetamide (CH_3CONH_2)	300	Sharma et al. [14]
		1500	Sharma et al. [22]
2.	Acetanilide (C_8H_9NO)	500	El-Sebaii et al. [34]
3.	Benzamide	1000	Dheep and Shreekumar [35]
4.	Capric acid (55 wt%) + Expanded perlite (45 wt%)	5000	Sarı and Karaipekli [31]
5.	Erythritol	1000	Shukla et al. [24]
6.	Lauric acid ($C_{11}H_{23}COOH$)	120	Abhat and Malatidis [36]
		1200	Sarı [37]
		910	Sari and Kaygusuz [30]
7.	Methyl palmitate	50	Nikolic et al. [38]
8.	Methyl stearate	50	Nikolic et al. [38]
9.	Myristic acid ($C_{13}H_{27}COOH$)	450	Hasan and Sayigh [39]
		1200	Sarı [37]
		910	Sari and Kaygusuz [30]
10.	Palmitic acid ($C_{15}H_{31}COOH$)	120	Abhat and Malatidis [36]
		450	Hasan [40]
		1200	Sarı [37]
		910	Sari and Kaygusuz [30]
11.	Palmitic acid (80 wt%) + Expanded graphite (20 wt%)	3000	Sarı and Karaipekli [32]
12.	Palmitic acid-TiO_2 composite	1500	Sharma et al. [41]
13.	Stearic acid ($C_{17}H_{35}COOH$)	450	Hasan [42]
		300	Sharma et al. [14]
		1200	Sarı [37]
		910	Sari and Kaygusuz [30]
		1500	Sharma et al. [22]
14.	Sebacic acid	1000	Dheep and Shreekumar [35]
15.	Urea	50	Sharma et al. [43]
16.	D-mannitol 99%	50	Sole et al. [44]
17.	Myo-inositol 98%	100	Sole et al. [44]
18.	Galactitol 97%	50	Sole et al. [44]

Table 3. Thermal cycled non-paraffins.

5.2.1. Salt hydrates

The oldest group of PCMs is salt hydrates. Salt hydrates are alloys of members of the inorganic salt family (oxides, carbonates, sulfates, and nitrates) with water molecules with a specific ratio. The chemical formula for salt hydrates is AB (salt compound).nH_2O. The salt hydrates show a three dimensional structure which is open enough to absorb and adjust water molecules inside the crystal lattice. **Figure 6** shows the crystal lattice of calcium chloride, which easily attracts H_2O molecules and forms calcium chloride hexahydrate.

The bonds are usually hydrogen bonds. The location and orientation of water molecules are well-defined in the structure. These types of PCMs have sharp transitions at the melt point, higher latent heats, smaller density change and have higher thermal conductivities than the organics. They have higher densities than the organics. Though these advantages, wide spread utilization are limited due to some negative attributes. The most significant issue with salt hydrates is their chemical instability. As salt hydrates consist of salt and water, there is a tendency to separate it into different phases. They lose some water content after every heating cycle. During the melting of salt hydrates dehydrated salts tend to settle out. It is called phase separation. The problem of phase separation can be eliminated to a certain extent with the use of gelled or thickened mixtures. High degree of supercooling is another major problem. They do not start to crystallize at the specified freezing point. The problem of supercooling can be eliminated with the use of suitable nucleating agents to start the crystal growth in the storage media. Regarding the compatibility with other materials, salts can be corrosive to metals. Their safety differs strongly between different salts. The volume change of salt hydrates is up to 10 vol.%. They have high thermal conductivity and low cost. Furthermore, some salts are chemically aggressive towards structural materials. Due to sharp melting point, higher

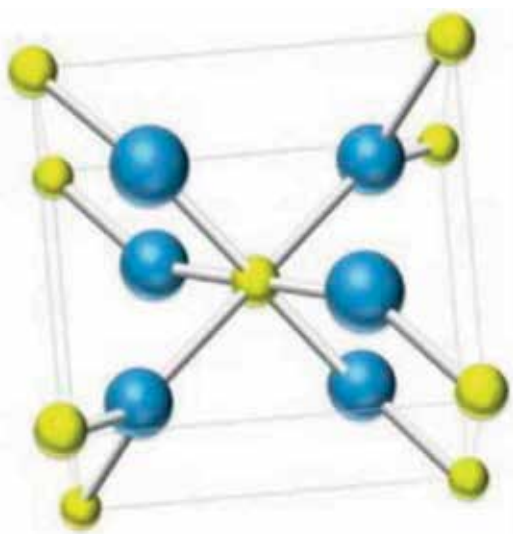

Figure 6. Crystal lattice of calcium chloride [10].

thermal conductivity, low cost and abundant in nature, salt hydrates have potential for heat storage applications [28]. However, less consideration has given by the researchers due to the major issues of it i.e. phase separation and supercooling. A list of salt hydrates tested by various researchers for stability along with their melting point and latent heat of fusion is shown in **Table 4**.

The latent heat of fusion of paraffins, fatty acids and salt hydrates whose melting temperatures are within 0–120°C is observed in **Figure 7**. It is noted that the melting temperature range of almost all PCMs is 20–60°C except acetamide, acetanilide, trichlorofluoromethane heptadecahydrate, $MgCl_2 \cdot 6H_2O$. Further, it is observed that the latent heat of fusion of these PCMs are in the range of 120–225 kJ/kg.

5.2.2. Metal alloy PCMs

This group consists of the low melting metals and metal alloys. This category of PCMs is the most underused of all the common PCM categories, perhaps due to the low latent heat and weight penalties. However, despite this, the metals exhibit the potential in certain applications where the compactness is important. This is due to the fact that it has high heat of fusion per unit volume. The metals that can be used in low temperature applications are cesium, gallium, indium, tin and bismuth, while the metals for high temperature applications include zinc, magnesium, aluminum and their alloys [10]. The researchers are attracted to these PCMs at some extend because of higher thermal conductivities and high

Sr. no.	PCMs	Thermal cycles	Reference
1.	Calcium chloride hexahydrate	1000	Kimura and Kai [45]
	($CaCl_2 \cdot 6H_2O$)	1000	Fellchenfeld et al. [46]
		5650	Porisini [47]
		1000	Tyagi et al. [48]
2.	Glauber's salt ($Na_2SO_4 \cdot 10H_2O$)	320	Marks [49]
		5650	Porisini [47]
3.	Magnesium chloride hexahydrate ($MgCl_2 \cdot 6H_2O$)	500	El-Sebaii et al. [34]
		1000	El-Sebaii et al. [19]
4.	$Na_2SO_4 \cdot nH_2O$	1000	Ting et al. [50]
5.	$Na_2SO_4 \cdot 1/2NaCl.10H_2O$	5650	Porisini [47]
6.	$NaOH \cdot 3.5H_2O$	5650	Porisini [47]
7.	Sodium acetate trihydrate	500	Wada et al. [51]
	($NaCH_3COO \cdot 3H_2O$)	100	Kimura and Kai [52]
8.	Trichlorofluoromethane heptadecahydrate ($CCl_3F \cdot 17H_2O$)	100	Kimura and Kai [53]

Table 4. Thermal cycled salt hydrates.

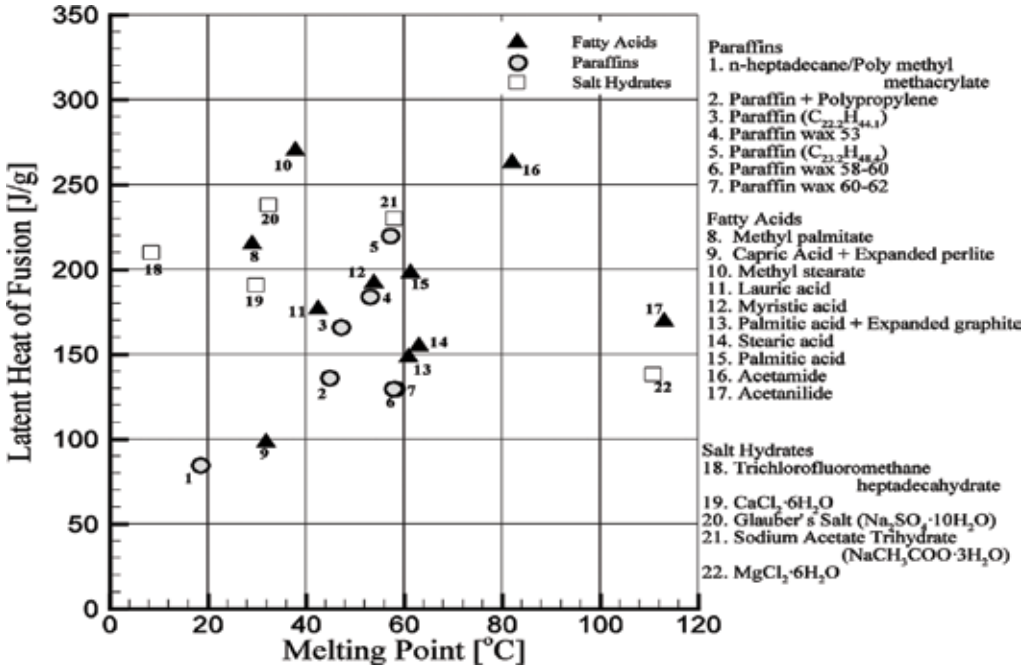

Figure 7. Latent heat of fusion of paraffins, fatty acids and salt hydrates undergoing a phase transition within the temperature range 0–120°C [5].

physical and chemical stability. Sun et al. [54] established the thermal stability and corrosion characteristics of the PCM, i.e. Al–34% Mg–6% Zn alloy. The melting temperature is 454°C and latent heat of fusion is 314.4 kJ/kg. Thermal stability test was carried out for 1000 thermal cycles. The change in melting temperature of this alloy was observed in the range of 3.06–5.3°C after 1000 thermal cycles. The latent heat of fusion is also decreased only 10.98% after 1000 thermal cycles.

Sr. no.	PCM	Thermal cycles	Reference
1.	$CaCl_2 \cdot 6H_2O$ (80 mol%) + $CaBr_2 \cdot 6H_2O$ (20 mol%)	1000	Kimura and Kai [56]
2.	$CaCl_2 \cdot 6H_2O$ (93 wt%) + $Ca(NO_3)_2 \cdot 4H_2O$ (5 wt%) + $Mg(NO_3)_2 \cdot 6H_2O$ (2 wt%)	1000	Kimura and Kai [56]
3.	$CaCl_2 \cdot 6H_2O$ (96 wt%) + KNO_3 (2 wt%) + KBr (2 wt%)	1000	Kimura and Kai [56]
4.	$CaCl_2 \cdot 6H_2O$ (96 wt%) + NH_4NO_3 (2 wt%) + NH_4Br (2 wt%)	1000	Kimura and Kai [56]
5.	$NaCH_3COO \cdot 3H_2O$ (90 wt%) + $NaBr \cdot 2H_2O$ (10 wt%)	1000	Kimura and Kai [52]
6.	$NaCH_3COO \cdot 3H_2O$ (85 wt%) + $NaHCOO \cdot 3H_2O$ (15 wt%)	1000	Kimura and Kai [52]
7.	$Mg(NO_3)_2 \cdot 6H_2O$ (93 wt%) + $MgCl_2 \cdot 6H_2O$ (7 wt%)	1000	Nagano et al. [57]

Table 5. Thermal cycled inorganic eutectics.

Sr. no.	PCM	Thermal cycles	Reference
1.	Ammonium alum ($NH_4Al(SO_4)_2 \cdot 12H_2O$)(15%) + ammonium nitrate (NH_4NO_3)(85%)	1100	Jotshi et al. [58]
2.	Butyl stearate (49 wt%) + Butyl palmitate (48 wt%) + Other (3 wt%)	100	Feldman et al. [59]
3.	Capric acid (65 mol%) + Lauric acid (35 mol%)	120	Dimaano and Escoto [60]
		360	Shilei et al. [61]
4.	Capric acid (73.5 wt%) + Myristic acid (26.5 wt%)	5000	Karaipekli et al. [62]
5.	Capric acid (83 wt%) + Stearic acid (17 wt%)	5000	Karaipekli et al. [63]
6.	Caprylic acid (70 wt%) + 1-dodecanol (30 wt%)	120	Zuo et al. [64]
7.	Lauric acid (66 wt%) + Myristic acid (34 wt%)	1460	Sari [65]
8.	Lauric acid (69 wt%) + Palmitic acid (31 wt%)	1460	Sari [37]
9.	Lauric acid (75.5 wt%) + Stearic acid (24.5 wt%) +	360	Sarı et al. [66]
10.	Lauric acid (77.05 wt%) + Palmitic acid (22.95 wt%)	100	Zhang et al. [29]
11.	Methyl stearate (86 wt%) + Methyl palmitate (14 wt%)	50	Nikolic et al. [38]
12.	Methyl stearate (91 wt%) + Cetyl palmitate (9 wt%)	50	Nikolic et al. [38]
13.	Methyl stearate (91 wt%) + Cetyl stearate (9 wt%)	50	Nikolic et al. [38]
14.	Myristic acid (58 wt%) + Palmitic acid (42 wt%)	360	Sarı et al. [66]
15.	Myristic acid (64 wt%) + Stearic acid (36 wt%)	1460	Sari [65]
16.	Myristic acid + Glycerol	1000	Sarı et al. [67]
17.	Palmitic acid (64.2 wt%) + Stearic acid (35.8 wt%)	360	Sarı et al. [66]
18.	Palmitic acid + Glycerol	1000	Sarı et al. [67]
19.	Stearic acid + Glycerol	1000	Sarı et al. [67]
20.	Tetradodecanol (53.60 wt%) + Lauric acid (46.40 wt%)	1000	Jingyu et al. [68]
21.	Tetradodecanol (71.84 wt%) + Myristic acid (28.16 wt%)	1000	Jingyu et al. [68]

Table 6. Thermal cycled organic eutectics.

5.3. Thermal stability of eutectics

A eutectic is a congruent composition of two or more components, each of which melts and freezes as a single compound. The eutectic PCM can be a mixture of two or more compounds of either organic materials, inorganic materials or both. The mixture of these compound forms

a crystal during crystallization. They melt and freeze to an intimate mixture of crystals simultaneously without separation [55]. The primary issue with these compounds is the cost. They are two or three times costlier than organic or inorganic PCMs.

Myriad eutectics can be produced for any preferred melting point for thermal energy storage systems. However, only limited data are available on their thermo-physical properties of these eutectics as the use of these materials is very new to thermal storage applications. Some of the inorganic and organic eutectics which were produced and studied for thermal stability by earlier investigators are listed in **Tables 5** and **6** respectively.

It can be noted that the most developed eutectics proposed as PCM were tailored from fatty acids and salt hydrates respectively. The recent research is more focused to organic eutectics, considering the phase separation and super cooling issues of the salt hydrates. It is observed that the thermal stability test was carried out for most of the eutectics for at least 1000 thermal cycles.

Figure 8 shows the latent heat of fusion of eutectics having melting temperature within a temperature range of 0–80°C. The most of the organic eutectics have melting point and latent heat of fusion are in the range of 20–60°C and 150–200 kJ/kg respectively. Also, the inorganic eutectics developed from calcium chloride hexahydrate has melting point near 20°C and latent heat of fusion below 150 kJ/kg. It can be noted that the eutectic developed from methyl stearate and methyl palmitate has higher latent heat of fusion out of all eutectics.

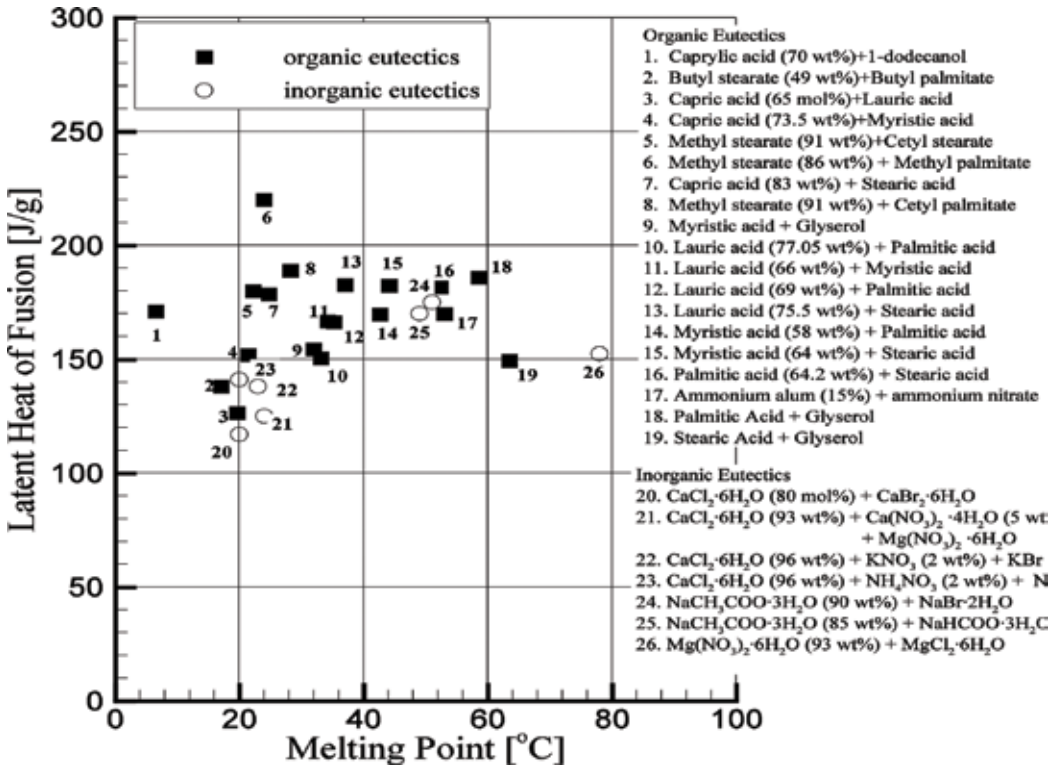

Figure 8. Latent heat of fusion per unit mass of eutectics undergoing a phase transition within the temperature range 0–100°C [5].

The equipment used to carry out thermal cycle test for different sample of PCMs are thermostatic chamber, thermal bath, electric hot plate, thermal box with heater and cooler, two thermostatic bath, etc. Most researchers have used have used thermostatic chamber setup to cycle the sample. However, there are vast varieties of equipments through which thermal cycle test will be carried out. There is no standard rule or format for selection of the equipment to conduct thermal cycles. The selection of the equipment is based on its availability, cost and rapidity of thermal cycles required.

6. Concluding remarks

It is required to make sure thermal stability of PCM after repeated number of thermal cycles for long term performance of latent heat energy storage unit. The PCM is most thermally stable and reliable, if the change in its thermo-physical properties, especially latent heat and melting point PCM is negligible after repeated number of thermal cycles. The following conclusions are drawn from the analysis of literature related to thermal stability of PCMs.

1. The differential scanning calorimetry (DSC) technique is the most common method to measure thermal properties of PCM i.e. melting point and latent heat of fusion. It is also noted that baring a few exception, no measurements were performed to establish the temperature dependent properties like specific heat, thermal conductivity etc. of PCMs. The thermal stability with respect to these temperature dependence parameters should also be observed after repeated number of thermal cycles.
2. It is found that most studied PCMs are those whose melting temperature and latent heat of fusion are in the range of 40–60°C and 150–225 kJ/kg respectively. However, most of the salt hydrates analyzed by the researchers has melting point near 20–30°C.
3. Paraffins are perhaps the most popular type of PCM as they are available in wide range of phase transition temperature. As paraffin melts more slowly over a wide range of temperatures, it is preferable to speak of a melt range instead of melting temperature. Fatty acids are prospective PCMs as they are produced from common vegetable and animal oils which ensure continuous supply even during shortage of fuel sources. The most analyzed fatty acids are stearic acid, lauric acid, myristic acid, capric acid and palmitic acid. It is also observed that organic PCM have better thermal stability after number of thermal cycles.
4. The major issues with the salt hydrates are phase separation and subcooling. In most cases phase separation can be overcome using a gelling additive. In order to suppress subcooling, a suitable nucleating material has to be added to the PCM to ensure that the solid phase is formed with little subcooling.
5. Many researchers focus on development of new eutectic type PCMs in spite of pure compounds since last decade. It is also observed here that almost all eutectic PCMs analyzed for thermal cycling test are made from fatty acids which give the melting temperature range and latent heat of fusion between 20 and 60°C and 150–200 kJ/kg respectively.

Author details

Manish K. Rathod

Address all correspondence to: mkr@med.svnit.ac.in

Department of Mechanical Engineering, Sardar Vallabhbhai National Institute of Technology (SV NIT), Surat, Gujarat, India

References

[1] Dincer I, Rosen MA. Thermal Energy Storage Systems and Applications. 2nd ed. United Kingdom: John Wiley and Sons Ltd; 2002

[2] Kaygusuz K. The viability of thermal energy storage. Energy Sources. 1999;**21**:745-755

[3] Farid MM, Khudhair AM, Siddique AK, Sari A. A review on phase change energy storage: Materials and applications. Energy Conversion and Management. 2004;**45**:1597-1615

[4] Sharma A, Tyagi V, Chen CR, Buddhi D. Review on thermal energy storage with phase change materials and applications. Renewable and Sustainable Energy Reviews. 2009; **13**(2):318-345

[5] Rathod MK, Banerjee J. Thermal stability of phase change materials used in latent heat energy storage systems: A review. Renewable and Sustainable Energy Reviews. 2013; **18**:246-258

[6] Telkes M, Raymond E. Storing solar heat in chemicals—A report on the Dover house. Heat Vent. 1949;**46**(11):80-86

[7] Abhat A. Low temperature latent heat thermal energy storage: Heat storage materials. Solar Energy. 1983;**30**(4):313-331

[8] Kalaiselvam, Parameshwaran. Thermal Energy Storage Technologies for Sustainability. Elsevier Inc; 2014

[9] Cabeza LF. Advances in Thermal Energy Storage Systems: Methods and Applications. Woodhead Publishing Series in Energy: Number 66. Elsevier Inc; 2015

[10] Fleischer AS. Thermal energy storage using phase change materials. In: SpringerBriefs in Thermal Engineering and Applied Science. 2015

[11] Kenisarin M, Mahkamov K. Solar energy storage using phase change material. Renewable and Sustainable Energy Reviews. 2007;**11**(9):1913-1965

[12] Ferrer G, Sole A, Barreneche C, Martorell I, Cabeza LF. Review on the methodology used in thermal stability characterization of phase change materials. Renewable and Sustainable Energy Reviews. 2015;**50**:665-685

[13] Buddhi D, Sawhney RL. In: Proceedings on Thermal Energy Storage and Energy Conversion; 1994

[14] Sharma SD, Buddhi D, Sawhney RL. Accelerated thermal cycle test of latent heat storage materials. Solar Energy. 1999;**66**(6):483-490

[15] Dean JA. The Analytical Chemistry Handbook. New York: McGraw Hill, Inc; 1995. pp. 15.1-15.5

[16] Pungor EA. Practical Guide to Instrumental Analysis. Boca Raton, Florida; 1995. pp. 181-191

[17] Skoog DA, Holler FJ, Timothy N. Principles of Instrumental Analysis. 5th ed. New York; 1998. pp. 805-808

[18] Rathod MK, Banerjee J, Chaudhari VN. Thermal reliability of stearic acid as phase change material used in latent heat storage. In: International Conference on Advances and Trends in Engineering Materials and their Applications; Montreal, Canada; 2011

[19] El-Sebaii AA, Al-Heniti S, Al-Ghamdi AA, Al-Marzouki F. One thousand thermal cycles of magnesium chloride hexahydrate as a promising PCM for indoor solar cooking. Energy Conversion and Management. 2011;**52**:1771-1777

[20] Alkan C, Kaya K, Sari A. Preparation, thermal properties and thermal reliability of form-stable paraffin/polypropylene composite for thermal energy storage. Journal of Polymers and the Environment. 2009;**17**:254-258

[21] Hadjieva M, St K, Argirov J. Thermophysical properties of some paraffins applicable to thermal energy storage. Solar Energy Materials and Solar Cells. 1992;**27**:181-187

[22] Sharma A, Sharma SD, Buddhi D. Accelerated thermal cycle test of acetamide, stearic acid and paraffin wax for solar thermal latent heat storage applications. Energy Conversion and Management. 2002;**43**:1923-1930

[23] Silakhori M, Naghavi MS, Metselaar HSC, Mahlia TMI, Fauzi H, Mehrali M. Accelerated thermal cycling test of microencapsulated paraffin wax/polyaniline made by simple preparation method for solar thermal energy storage. Materials. 2013;**6**:1608-1620

[24] Shukla A, Buddhi D, Sawhney RL. Thermal cycling test of few selected inorganic and organic phase change materials. Renewable Energy. 2008;**33**:2606-2614

[25] Sari A, Eroglu R, Biçer A, Karaipekli A. Synthesis and thermal energy storage properties of erythritol tetrastearate and erythritol tetrapalmitate. Chemical Engineering and Technology. 2011;**34**(1):87-92

[26] Karaipekli A, Bicer A, Sari A, Tyagi VV. Thermal characteristics of expanded perlite/paraffin composite phase change material with enhanced thermal conductivity using carbon nanotubes. Energy Conversion and Management. 2017;**134**:373-381

[27] Hasnain S. Review on sustainable thermal energy storage technologies. Part I: Heat storage materials and techniques. Energy Conversion and Management. 1999;**39**:1127-1138

[28] Zalba B, Marin JM, Cabeza LF, Mehling H. Review on thermal energy storage with phase change: Materials, heat transfer analysis and applications. Applied Thermal Engineering. 2003;**23**:251-283

[29] Zhang JJ, Zhang JL, He SM, Wu KZ, Liu XD. Thermal studies on the solid-liquid phase transition in binary systems of fatty acids. Thermochimica Acta. 2001;**369**:157-160

[30] Sari A, Kaygusuz K. Some fatty acids used for latent heat storage: Thermal stability and corrosion of metals with respect to thermal cycling. Renewable Energy. 2003;**28**:939-948

[31] Sari A, Karaipekli A. Preparation, thermal properties and thermal reliability of capric acid/expanded perlite composite for thermal energy storage. Materials Chemistry and Physics. 2008;**109**:459-464

[32] Sarı A, Karaipekli A. Preparation, thermal properties and thermal reliability of palmatic acid/expanded graphite composite as form–stable PCM for thermal energy storage. Solar Energy Materials and Cells. 2009;**93**:571-576

[33] Zalba B, Marin JM, Cabeza LF, Mehling H. Free-cooling of buildings with phase change materials. International Journal of Refrigeration. 2003;**27**:839-849

[34] El-Sebaii AA, Al-Amir S, Al-Marzouki FM, Faidah AS, Al-Ghamdi AA, Al-Heniti S. Fast thermal cycling of acetanilide and magnesium chloride hexahydrate for indoor solar cooking. Energy Conversion and Management. 2009;**50**:3104-3111

[35] Dheep GR, Shreekumar A. Influence of accelerated thermal charging and discharging cycles on thermo-physical properties of organic phase change materials for solar thermal energy storage applications. Energy Conversion and Management. 2015;**105**:13-19

[36] Abhat A, Malatidis NA. Determination of properties of heat of fusion storage materials for low temperature applications. In: 1st IEA Conference on New Energy Conservation Technologies and their Commercialisation; Berlin, FRG: Springer; 1981

[37] Sari A. Thermal reliability test of some fatty acids as PCMs used for solar thermal latent heat storage applications. Energy Conversion and Management. 2005;**44**:2277-2287

[38] Nikolic R, Marinovic-Cincovic M, Gadzuric S, Zsigrai IJ. New materials for solar thermal storage solid/liquid transitions in fatty acid esters. Solar Energy Materials & Solar Cells. 2003;**79**:285-292

[39] Hasan A, Sayigh AA. Some fatty acids as phase-change thermal energy storage materials. Renewable Energy. 1994;**4**(1):69-76

[40] Hasan A. Phase change material energy storage system employing palmatic acid. Solar Energy. 1994;**52**(2):143-154

[41] Sharma RK, Ganesh P, Tyagi VV, Metselaar HSC, Sandaran SC. Thermal properties and heat storage analysis of palmitic acid-TiO_2 composite as nano-enhanced organic phase change material (NEOPCM). Applied Thermal Engineering. 2016;**99**:1254-1262

[42] Hasan A. Thermal energy storage system with stearic acid as phase change material. Energy Conversion and Management. 1994;**35**(10):843-856

[43] Sharma A, Sharma SD, Buddhi D, Sawhney RL. Thermal cycle test of urea for latent heat storage applications. International Journal of Energy Resources. 2001;**25**:465-468

[44] Solé A, Neumann H, Niedermaier S, Martorell I, Schossig P, Cabeza LF. Stability of sugar alcohols as PCM for thermal energy storage. Solar Energy Materials & Solar Cells. 2014;**126**:125-134

[45] Kimura H, Kai J. Phase change stability of $CaCl_2.6H_2O$. Solar Energy. 1984;**33**(1):49-55

[46] Fellchenfeld H, Sarig S. Calcium chloride hexahydrate: A phase-changing material for energy storage. Industrial and Engineering Chemistry Product Research and Development. 1985;**24**:130-133

[47] Porosini FC. Salt hydrates used for latent heat storage: Corrosion of metals and reliability of thermal performance. Solar Energy. 1988;**41**:193-197

[48] Tyagi VV, Buddhi D. Thermal cycle testing of calcium chloride hexahydrate as a possible PCM for latent heat storage. Solar Energy Materials & Solar Cells. 2008;**92**(8):891-899

[49] Marks S. An investigation of the thermal energy storage capacity of Glauber's salt with respect to thermal cycling. Solar Energy. 1980;**25**:225-258

[50] Ting KC, Giannakakos PN, Gilbert SG. Durability of latent heat storage tube-sheets. Solar Energy. 1987;**39**(2):79-85

[51] Wada T, Yamamoto R, Matsuo Y. Heat storage capacity of sodium acetate trihydrate during thermal cycling. Solar Energy. 1984;**33**(3/4):373-375

[52] Kimura H, Kai J. Phase change stability of sodium acetate trihydrate and its mixtures. Solar Energy. 1985;**35**(6):527-534

[53] Kimura H, Kai J. Feasibility of trichlorofluoromethane (CCl_3F, R11) heptadecahydrate as a heat storage material. Energy Conversion and Management. 1985;**25**(2):179-186

[54] Sun JQ, Zhang RY, Liu ZP, Lu GH. Thermal reliability test of Al–34%Mg–6%Zn alloy as latent heat storage material and corrosion of metal with respect to thermal cycling. Energy Conversion and Management. 2007;**48**(2):619-624

[55] Lane GA. Phase change thermal storage materials. In: Guyer C, editor. Hand Book of Thermal Design. McGraw Hill Book Co; 1981

[56] Kimura H, Kai J. Mixture of calcium chloride hexahydrate with some salt hydrates or anhydrous salts as latent heat storage materials. Energy Conversion and Management. 1988;**28**(3):197-200

[57] Nagano K, Ogawa K, Mochida T, Hayashi K, Ogoshi H. Thermal characteristics of magnesium nitrate hexahydrate and magnesium chloride hexahydrate mixture as a phase change material for effective utilization of urban waste heat. Applied Thermal Engineering. 2004;**24**(2-3):221-232

[58] Jotshi CK. Thermal storage in ammonium alum/ammonium nitrate eutectic for solar space heating applications. Solar Energy Engineering. 1998;**120**:20-24

[59] Feldman D, Banu D, Hawes D, Ghanbari E. Obtaining an energy storing building material by direct incorporation of an organic phase change material in gypsum board. Solar Energy Materials. 1991;**22**:231-242

[60] Dimaano M, Escoto A. Preliminary assessment of a mixture of capric acid and lauric acids for low-temperature thermal energy storage. Energy. 1998;**23**:421-427

[61] Shilei L, Neng Z, Guohui F. Eutectic mixture of capric acid and lauric acid applied in building wallboards for heat energy storage. Energy and Buildings. 2006;**38**:708-711

[62] Karaipekli A, Sari A. Capric-myristic acid/expanded perlite composite as form-stable phase change material for latent heat thermal energy storage. Renewable Energy. 2008;**33**:2599-2605

[63] Karaipekli A, Sari A, Kaygusuz K. Thermal properties and thermal reliability of capric acid/stearic acid mixture for latent heat thermal energy storage. Energy Sources, Part A: Recovery, Utilization, and Environmental Effects. 2009;**31**:199-207

[64] Zuo J, Li W, Weng L. Thermal performance of caprylic acid/ 1-dodecanol eutectic mixture as phase change material (PCM). Energy and Buildings. 2011;**43**:207-210

[65] Sari A. Eutectic mixtures of some fatty acids for low temperature solar heating applications: Thermal properties and thermal reliability. Applied Thermal Engineering. 2005;**25**: 2100-2107

[66] Sari A, Sari H, Onal A. Thermal properties and thermal reliability of eutectic mixtures of some fatty acids as latent heat storage materials. Energy Conversion and Management. 2004;**45**:365-376

[67] Sari A, Bicer A, Karaipekli A, Alkan C, Karadag A. Synthesis, thermal energy storage properties and thermal reliability of some fatty acid esters with glycerol as novel solid-liquid phase change materials. Solar Energy Materials & Solar Cells. 2010;**94**:1711-1715

[68] Jingyu H, Shilei L, Xiangfei K, Shangbao L, Yiran I. Form stable phase change material based on eutectic mixture of tetradecanol and fatty acids for building energy storage: Preparation and performance analysis. Materials. 2013;**6**:4758-4775

Section 4

Latent Heat Thermal Energy Storage System

Chapter 4

Latent Heat Thermal Energy Storage System

Ponnuraj Stella Jesumathy

Additional information is available at the end of the chapter

http://dx.doi.org/10.5772/intechopen.77177

Abstract

Latent heat thermal energy storage systems (LHTESS) are versatile due to their heat source at constant temperature and heat recovery with small temperature drop. In this context, latent heat thermal energy storage system employing phase change material (PCM) is the attractive one due to high-energy storage density with smaller temperature difference between storing and releasing functions. PCMs are generally possessed with low thermal conductivity, which leads to decreased rates of heat storage and extraction during melting and crystallization process. However, the low thermal conductivity of paraffin limits its use as a thermal energy storage material. In this chapter, experiments are conducted to investigate the enhancement of thermal conductivity of paraffin wax by adding alumina nanoparticles. Stable composites containing 5 and 10 vol% nanoparticles in paraffin were prepared by intense sonification. The thermophysical properties of the alumina nanoparticle enhanced paraffin (ANEP) specifically the melting and freezing temperature, latent heat, thermal conductivity, and dynamic viscosity were measured and compared with paraffin wax. These results as well as the thermal conductivity and dynamic viscosity variations with respect to temperature and nanoparticle volume concentration are discussed. Comparison of predicted Maxwell's model of a recent study shows higher enhancement than the Arasu predicted Maxwell's model.

Keywords: melting, solidification, latent heat, thermal conductivity, nanoparticle, phase change material

1. Introduction

Thermal energy storage technology has been garnering tremendous attention during the past two decades. In general, the thermal energy storage techniques exploit latent heat, sensible heat, and thermo-chemical. Among the aforementioned three types, latent heat thermal energy storage which employs phase change material is praiseworthy owing to its advantageous

characteristics, such as high storage density and nearly isothermal operating characteristics during the phase change process [1–5]. Consequently, it owns versatile applications in the fields of solar energy utilization, waste heat recovery, and active and passive cooling of electronic devices. Among the investigated PCMs, paraffin wax is regarded as the most promising phase change material because of its desirable characteristics such as large latent heat, minimal volume change, chemical stability, no phase segregation, nontoxicity, and commercial availability at low cost [6]. Inspite of these desirable properties of paraffin wax, the low thermal conductivity (0.21–0.24 W/m K) is its major drawback. Different approaches have been used to enhance the thermal conductivity of PCM, such as dispersion of high thermal conductive materials into PCMs, encasing the PCM within finned tubes, and impregnation of porous materials like carbon and metal foams [7]. Dispersing nanoparticles in paraffin has the potential to improve the thermal conductivity, thereby significantly improving its thermal energy storage characteristics. Zeng et al. [8] investigated the effect of copper nano wires (Cu NWs) dispersed in tetradecanol (TD). The thermal conductivity of the composite PCMs improved nine times better than that of pure PCM, when the composite PCM was containing 11.9 vol% Cu NWs. In this chapter, emulsion of alumina nanoparticles into melting paraffin wax in different volume fractions was prepared to study the thermophysical properties like melting/freezing point, latent heat, thermal conductivity, and dynamic viscosity. Stable composites were prepared, and a significant thermal conductivity enhancement is reported in this chapter. The distinguishing feature of this chapter is to compare the present thermal conductivity results of various volume fractions with the predicted Maxwell model as reported in the literature [9].

2. Preparation of nanocomposite PCMs

In the present study, paraffin wax (T_m = 58–60°C) is employed as PCM owing to its desirable properties like chemical stability, nontoxic, high latent heat capacity, etc. Al_2O_3 nanoparticles were purchased from Royal Scientific Suppliers Co. Ltd. The purity of the Al_2O_3 is 99.5%, and the particle size lies in the range of 20–50 nm. **Table 1** depicts the physical properties of paraffin wax, alumina nanoparticle [10], and nanocomposite PCM.

Nanocomposite PCMs were prepared by adding different volume fractions of Al_2O_3 nanoparticles into paraffin wax; however, no surfactant was used. **Figure 1** illustrates the steps involved in the preparation of composite PCMs with the addition of alumina nanoparticle in volume fractions of 5 and 10%. Initially, paraffin wax was heated to a temperature of 80°C, and the Al_2O_3 nanoparticles were then dispersed into the liquid paraffin wax. Suspensions were prepared by strong shear mixing at 1000 rpm for 20 min using a magnetic stirrer. The mixture was sonicated using an ultrasonic vibrator (Toshiba, India), generating ultrasonic pulses of 100 W at 36 ± 3 kHz. However, to ensure stability and homogeneity, intense sonication was done for a period of 6 hours. The mixture was kept in the liquid state throughout the process by maintaining a constant temperature of 65°C. There was no settling observed thereafter, and thus, the prepared composites were stable.

Parameter	Alumina nanoparticles	Paraffin wax, ϕ = 0	Nanocomposite, ϕ = 10 vol%
Latent heat of fusion, λ		121.9 J/g*	119.9 J/g*
Melting Temperature, $_{Tm}$		58.9°C*	58.6°C*
Solid density, ρ	3600 kg/m^3	860 kg/m^3	930.692 kg/m^3
Liquid density, ρ	—	780 kg/m^3	
Thermal conductivity, k	40 W/m K	0.24 (*s*) W/m K 0.15 (*l*) W/m K	0.42 W/mK @ 59°C
Specific heat, C_p	765 J/kg K	2.9 kJ/kg K (*s*) 2.1 kJ/kg K (*l*)	2686 J/kg K
Dynamic Viscosity,μ	—	0.205 Ns/m^2	0.2188 Ns/m^2

*Measured values (DSC)

Table 1. Physical properties of paraffin, alumina nanoparticles, and nanocomposite.

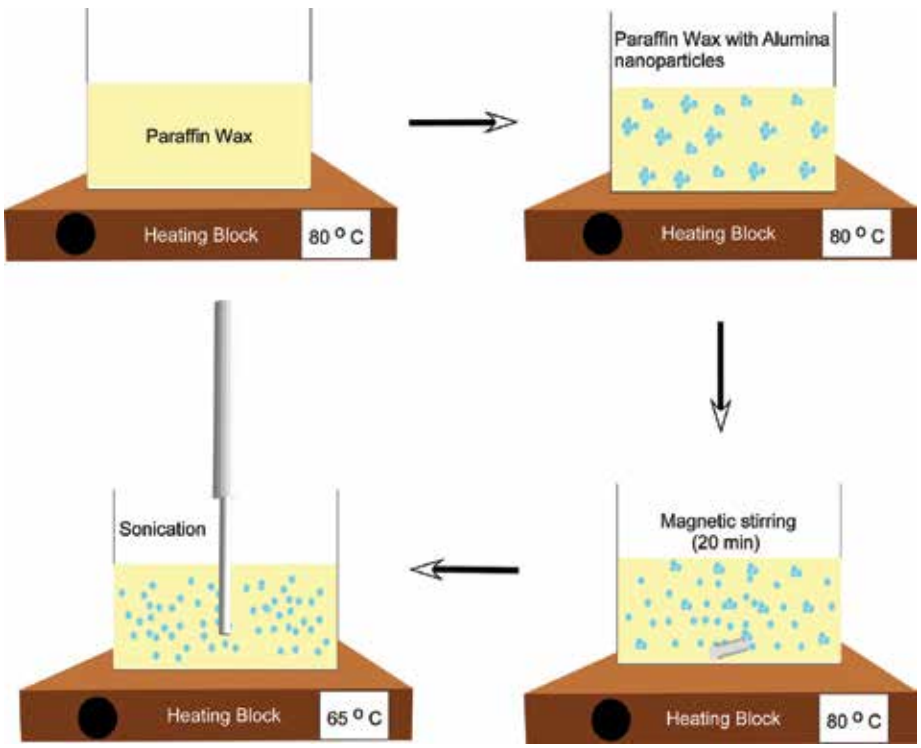

Figure 1. Preparation procedure of latent heat storage nanocomposite made of paraffin wax and alumina.

3. Thermal stability of nanocomposite PCMs

3.1. Differential scanning calorimetry

The phase change behavior of paraffin and paraffin/alumina composite involves two parameters: the latent heat and the phase change temperature, which can be measured by DSC (NETZSCH DSC 204) analysis. DSC thermogram of the paraffin and paraffin/alumina composite with 5 and 10 vol% of alumina nanoparticle is shown in **Figure 2a**, **b**, and **c**. The test results infer that nanocomposite exhibited only a single peak confirming to the solid-liquid transition, and no traces of solid-solid secondary peak were observed. These aspects are especially good for PCMs to maximize their heat storage and release capabilities at one stretch during melting and freezing cycles [11]. In DSC, the main peak represents the phase-change behavior of paraffin and paraffin/alumina composite. Phase change temperature is taken as onset temperature in DSC curve. With an increase in the volume fraction of alumina nanoparticle, the phase change temperature of paraffin/alumina composite increases and latent heat capacity of paraffin/alumina composite reduces compared to paraffin wax (heating curve) as shown in **Figure 2b** and **c**. The DSC results of paraffin, 5 vol%, and 10 vol% of alumina nanoparticle are presented in **Table 2**.

The melting temperature of 10 vol% of alumina shifted to 58.6°C, whereas paraffin was 58.9°C. On the other hand, the freezing temperature of 10 vol% of alumina shifted to 47°C, whereas paraffin wax was 44.4°C. The latent solid-liquid phase change for the composites are around 121 J/g, which is very close to the value of 124.4 J/g for pure paraffin. This is because no chemical reaction takes place between paraffin and nanoparticles in the preparation of nanocomposites. This is consistent with observations made by Ho and Gao [12] and Kim and Drzal [13]. Nanoparticle dispersions neither agree to affect the melting/freezing behavior nor the phase change temperature. The measured and calculated latent heat of paraffin/alumina composite is shown in **Table 3**. Using a simple mixture theory, the latent heat of fusion of the composite PCMs is calculated by:

$$\Delta H_{eff} = \Delta H_m \left(1 - \phi_v\right) \tag{1}$$

where ΔH_{eff} and ΔH_m stand for the calculated effective latent heat of fusion of composite PCMs and the measured latent heat of the fusion of the pure paraffin is 124.4 J/g (obtained by DSC at a scan rate of 1°C/min), respectively, and ϕ_v is the equivalent volume fraction of alumina. From **Table 3**, it is observed that latent heat of composite decreases with increase in volume fraction of alumina nanoparticle.

3.2. Comparison of DSC thermograms based on latent heat of nanoparticle embedded PCM with present study

3.2.1. Comparison of latent heat of Al_2O_3 nanoparticles in n-octadecane emulsion with present study

DSC thermograms of pure paraffin ($C_{18}H_{38}$) and Al_2O_3 nanoparticles in paraffin emulsion in various mass fractions 5 and 10 wt% are shown in **Figure 3**. The latent heat and phase change temperature are significantly different for paraffin-alumina emulsion composites.

http://dx.doi.org/10.5772/intechopen.77177

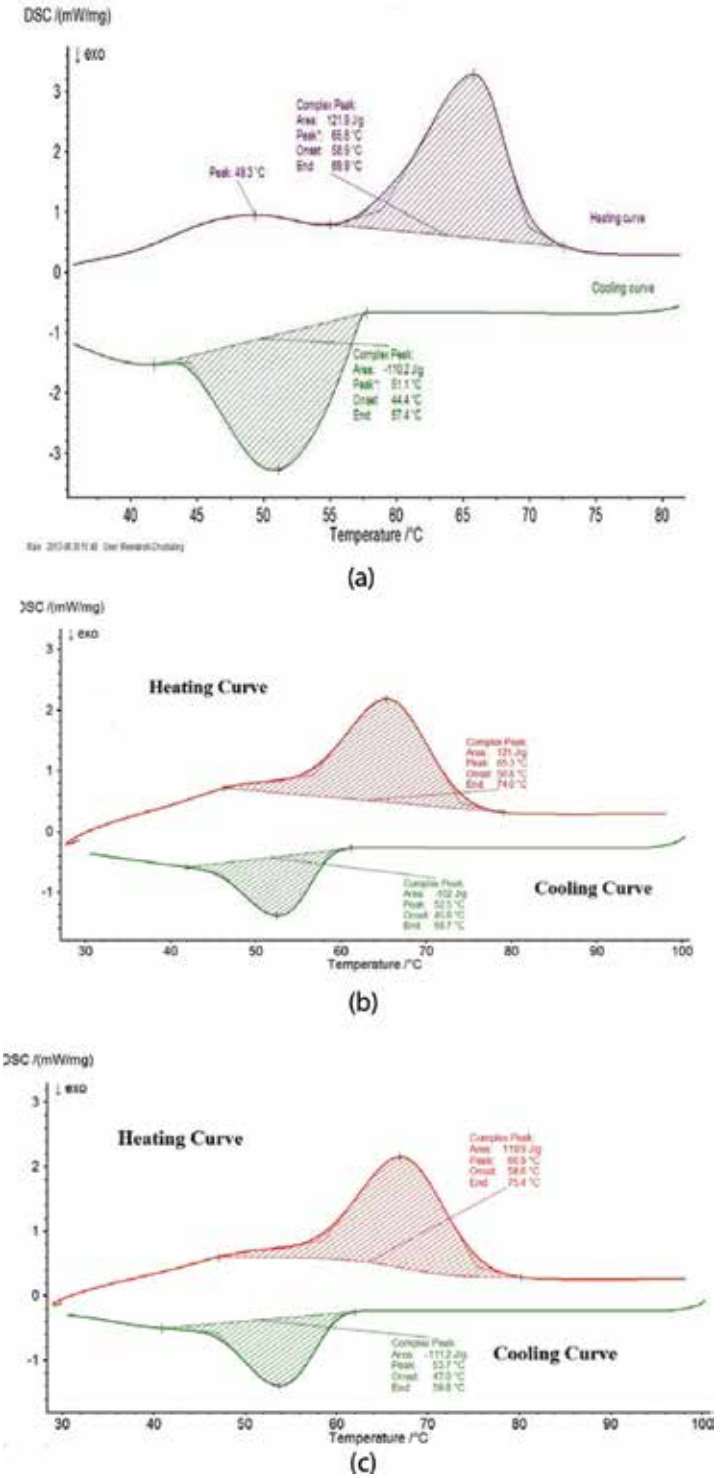

Figure 2. (a) DSC thermogram of paraffin wax, (b) DSC thermogram of composite with 5 vol% of alumina nanoparticle, and (c) DSC thermogram of composite with 10 vol% of alumina nanoparticle.

PCM/Composite	Melting temperature, T_m (°C)	Freezing temperature, T_f (°C)	Latent heat of fusion on heating curve (J/g)	Latent heat of fusion on cooling curve (J/g)
0 (paraffin wax)	58.9	44.4	121.9	−110.2
5 vol%	56.8	45.8	121	−102
10 vol%	58.6	47	119.9	−111.2

Table 2. Melting/freezing temperatures and latent heat of fusion of paraffin and composite.

Volume fraction of alumina, ϕ (%)	Phase change latent heat	
	Calculated value (J/g)	Experimental value (J/g)
5	122.85	121
10	121.90	119.9

Table 3. Experimental and calculated values of latent heat of fusion.

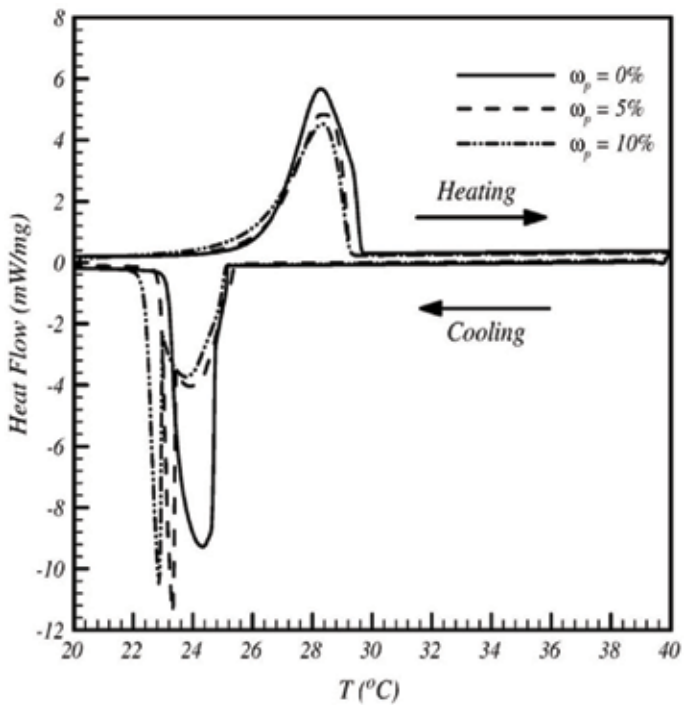

Figure 3. DSC thermograms of heating and cooling curves for Al_2O_3 in paraffin emulsions and pure paraffin ($C_{18}H_{38}$) in the range of 20–40°C [12].

Table 4 compares the latent heat of fusion of alumina nanoparticles in the *n*-octadecane emulsion with paraffin/alumina composites (scan rate @ 1°C/min). Latent heat of alumina-in-octadecane emulsion ($H_{Solid\text{-}liquid}$ = 212.3 kJ/kg) decreases with the increase in the mass fraction of alumina nanoparticles compared with that of the pure paraffin ($H_{Solid\text{-}liquid}$ = 243.1 kJ/kg), and the same trend is observed in our present study (**Table 2**). The measured values of the latent heat capacity of composites with 5 and 10 wt% are lower than that of pure paraffin ($C_{18}H_{38}$) by 7 and 13%, whereas the present study of latent heat of fusion of paraffin/alumina nanocomposites is nearly 8 and 14% for paraffin containing 5 and 10 vol% of alumina nanoparticles.

3.2.2. Comparison of latent heat of 10 wt% CNEP with present study

Figure 4 shows the DSC heating and cooling curve of 10 wt% copper oxide nanoparticle-enhanced paraffin (CNEP). The heating and cooling curve indicate two phase transition peaks.

Nanoparticle mass fraction (W_p)	Latent heat of fusion on heating curve (kJ/kg)	Nanoparticle volume fraction (ϕ)	Latent heat of fusion on heating curve (J/g)
0	243.1	0	124.4
5 wt%	225.6	5 vol%	114.3
10 wt%	212.3	10 vol%	107.2

Table 4. Comparison of latent heat of fusion of Al_2O_3—in octadecane emulsion with present study.

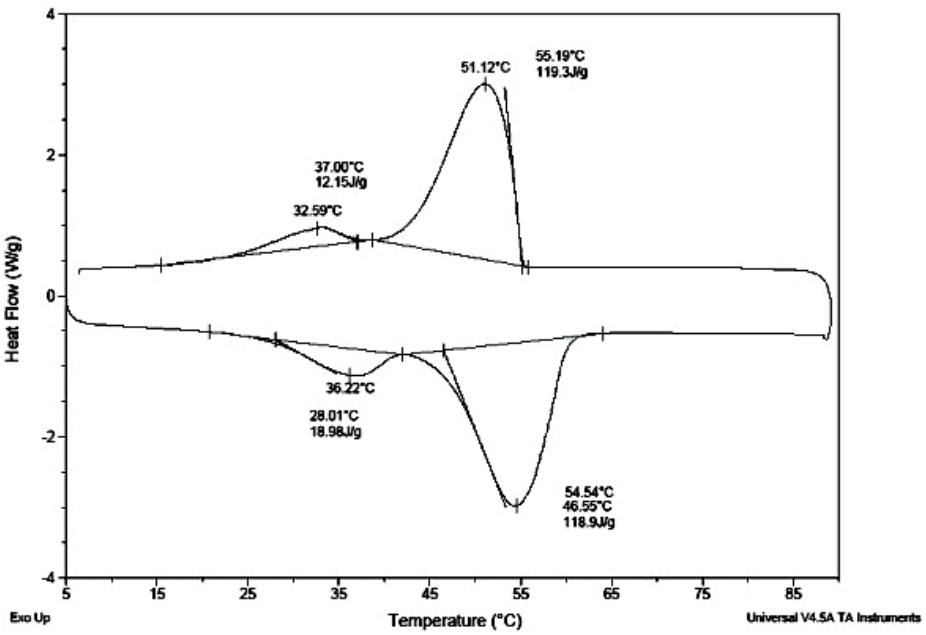

Figure 4. DSC thermograms of 10 wt% copper oxide nanoparticle enhanced paraffin [5].

The primary peak at around 35°C corresponds to the solid-solid phase change in paraffin, and the secondary peak at around 55°C corresponds to the solid-liquid phase change. The latent heat solid-liquid of 10 wt% **c**opper oxide nanoparticle-enhanced paraffin is 119.3 J/g, which is very close to the value of 119.9 J/g for 10 vol% of alumina nanoparticle-enhanced paraffin.

4. Thermophysical properties of nanocomposite PCMs

4.1. Specific heat capacity

The specific heat is one of the important properties and plays an important role in influencing heat transfer rate in nanocomposite. Predicted specific heat values (C_p) of the nanocomposite for various volume fraction can be calculated using mixture formula Eq. (2), and it is shown in **Table 5**. This formula is valid for homogenous mixtures.

$$C_{p\ nanocomposite} = \frac{(1-\phi)(\rho C_p)_{bf} + \phi(\rho C_p)_{np}}{\rho_{ANEP}} \tag{2}$$

As the thermal conductivity of nanocomposites is expected to be higher due to high thermal conductivity of Al_2O_3 particles, the nanocomposites show higher ability to conduct heat. This obviously results in lower heat storage capacity. From **Table 5**, it is depicted that the specific heat of nanocomposites decreases, the volume fraction of nanoparticle will be increased.

4.2. Improvement in thermal conductivity of nanocomposite

4.2.1. Thermal conductivity measurement

Thermal conductivity is measured by the procedure given in the literature [14]. However, a constant temperature hot water bath was also incorporated to maintain the composite at constant temperature to avoid solidification of the samples during the measurement. Thermal conductivity measurement of nanocomposite was made by KD2 Pro thermal property analyzer (Decagon Devices, Inc.; USA). Schematic view of KD2 Pro thermal property analyzer is shown in **Figure 5**. The KD2 Pro analyzer consists of a handheld microcontroller along with sensor needles. The sensor needle is composed of a heating element and thermistor. The controller module consists of three sets of batteries, a 16 bit microcontroller/AD converter, and power control circuit. The sensor needle (KS-1) made of stainless steel is 60 mm long and has a diameter of 1.3 mm and closely approximates an infinite line heat source. Each measurement cycle lasts for 90 s and consists of three stages. The instrument will equilibrate during the first

Volume fraction (ϕ) (vol%)	Specific heat capacity of nanocomposite (J/kg K)
5	2793
10	2686

Table 5. Specific heat capacity of nanocomposite.

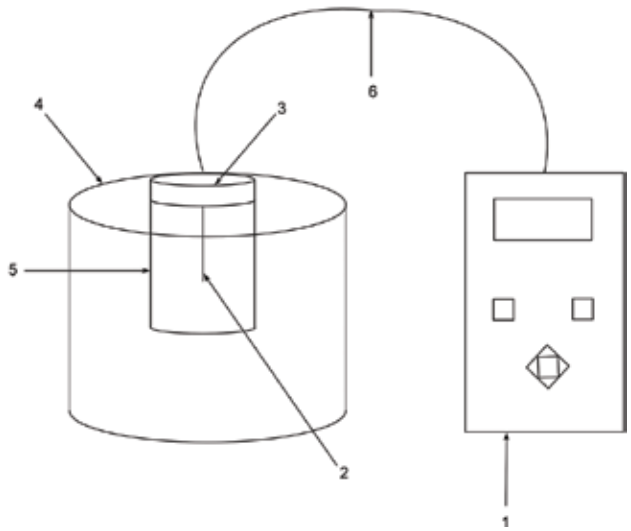

Figure 5. Schematic sketch of KD2 pro thermal property analyzer. 1-Microcontroller, 2-Sensor, 3-Septum, 4-Hot water bath, 5-Vial, 6-Cable.

30 seconds, which is followed by heating and cooling of the sensor needles for 30 seconds each. At the end of the reading, the controller computes the thermal conductivity using the change in temperature (ΔT)-time data as per Eq. (3).

$$k = \frac{q(\ln T_2 - \ln T_1)}{4\pi(\Delta T_2 - \Delta T_1)} \tag{3}$$

where q is the constant heat rate applied to an infinitely long and small "line" source, ΔT_1 and ΔT_2 are the changes in the temperature at times t_1 and t_2, respectively.

Thermal conductivity is the most important property of phase change materials and need detailed investigation. The thermal conductivity was measured as a function of temperature with respect to nanoparticle loading. **Figure 6** depicts the thermal conductivities of paraffin and composite assessed at various temperatures. It is explicit from the **Figure 6** that the influence of temperature on the thermal conductivity of paraffin as well as composites is less significant in solid and liquid states.

However, an atypical rise in thermal conductivity was observed near the solid - liquid phase change temperature, and the same suddenly falls down when the paraffin wax and nanocomposite PCM turned completely into liquid state. Thermal conductivity of paraffin wax and composites of various volume concentration is summarized in **Table 6**. The increase in thermal conductivity near the phase change is attributed to the accelerated molecular vibrations in the matrix of ordered solid structure when the temperature was increased [15]. The thermal conductivity of the composite with 5 vol% of alumina is 0.2677 W/mK at 45°C in the solid state and 0.24 W/mK at 65°C in the liquid state. After phase change, there is a breakage of the orderly solid structure into a disorderly liquid structure, and therefore, the thermal conductivity of

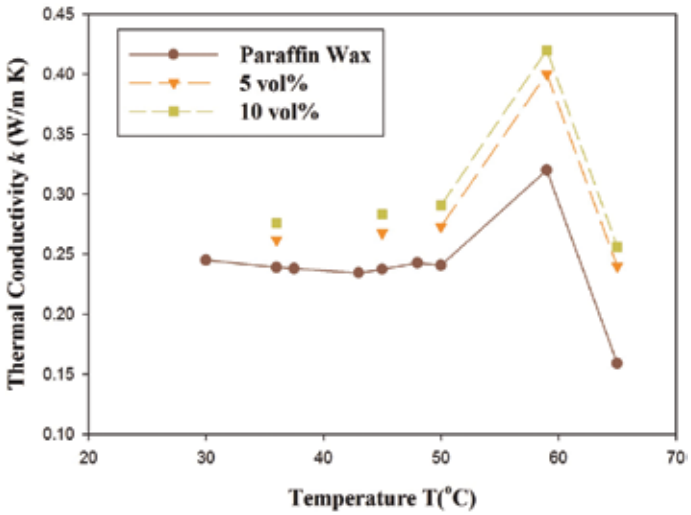

Figure 6. Thermal conductivity of paraffin wax and composite versus temperature.

paraffin wax and composite has become less than that in the solid state. The thermal conductivity of the paraffin wax is 0.2375 W/mK (45°C) in solid state and 0.1590 W/mK (65°C) in the liquid state. Thermal conductivity of composite with 10 vol% of alumina is higher than paraffin wax by 0.2834 W/mK at 45°C and 0.2560 W/mK at 65°C. However, higher thermal conductivity measured, i.e., k = 0.42 W/mK for 10 vol% of alumina at 59°C (close to the phase change temperature), is desirable for LHTES applications.

Thermal conductivity enhancement ratio was calculated by $\Psi = (k_c - k_p)/k_p$ with k_c being the thermal conductivity of composite and k_p thermal conductivity of paraffin wax, respectively. The thermal conductivity ratio of composites assessed at different temperatures for various volume concentration is depicted in **Figure 7**. The thermal conductivity enhancement of

Temperature (°C)	Thermal Conductivity (W/mK)		
	Paraffin wax	ϕ = 5 vol%	ϕ = 10 vol%
30	0.2450		
36	0.2390	0.2620	0.2760
37.5	0.2380		
43	0.2344		
45	**0.2375**	**0.2677**	**0.2834**
48	0.2427		
50	0.2406	0.2729	0.2906
59	0.3200	0.4000	0.4200
65	**0.1590**	**0.2400**	**0.2560**

Note: Show the temperature values in solid and liquid state (Bold).

Table 6. Thermal conductivity of paraffin and various volume fraction of alumina at different temperature.

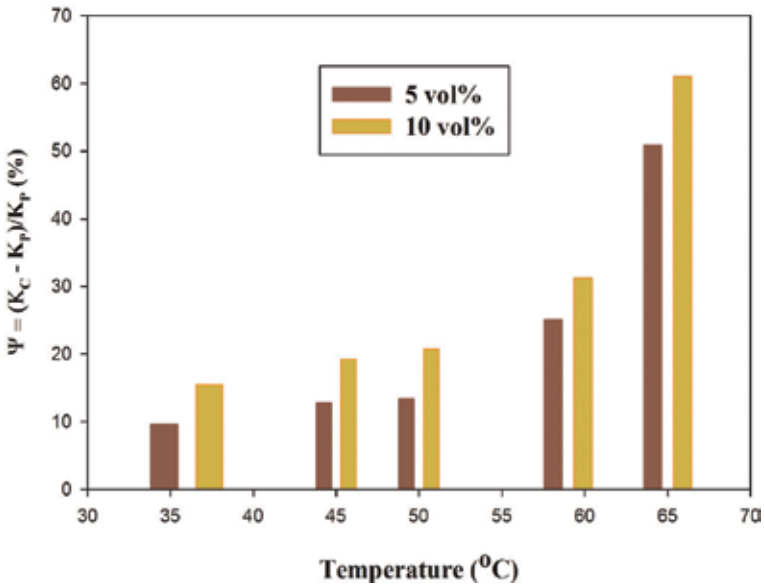

Figure 7. Thermal conductivity of composite as a function of temperature.

composite (5 vol% of alumina) is 12.71% at 45°C in solid state and 50.94% at 65°C in liquid state. For example, in 10 vol% of alumina, the enhancement ratio of composite is 19.32% at 45°C and 61% at 65°C in solid and liquid state, respectively. The thermal conductivity of the composite increased with an increase in the volume fraction of Al_2O_3, and also, the enhancement in liquid state (at 65°C) was higher than that in the solid state. The higher enhancement of the composite is attributed to more alumina addition. However, in the present study, the enhancement ratio of paraffin/alumina composite has improved from 9.62 to 61% for 5 and 10 vol% of alumina, respectively. Thermal conductivity of alumina is (k = 36 W/mK); the composites are expected to have considerable higher thermal conductivity than that of the paraffin wax. The higher enhancement in liquid state was primarily due to the enhanced Brownian motion of nanoparticles within the base fluid having considerably reduced viscosity due to increase in temperature, and it is discussed in detail in Section 4.5.1. Enhancement of thermal conductivity is due to deposition of nanoparticles in melting interface and agglomeration of the nanoparticle.

The liquid molecule close to particle surfaces is known to form layered structures and behave much like a solid. The results also showed that the thermal conductivity of paraffin could be achieved further by the addition of alumina more than 10 vol% of alumina nanoparticle. However, this volume fraction is adequate to obtain form-stable composite PCM, and further increase in alumina over 10 vol% of alumina nanoparticle will result in an increase in a latent heat capacity of the composite.

4.2.2. Comparison of thermal conductivity with Maxwell model

The theoretical thermal conductivity of solid phase paraffin/alumina composite PCMs was calculated using Maxwell's model [16].

$$k_{pred} = k_{bf\times} \frac{k_p + 2k_{bf} - 2\phi_v\left(k_{bf} - k_p\right)}{k_p + 2k_{bf} + \phi_v\left(k_{bf} - k_p\right)} \tag{4}$$

where k_p is the thermal conductivity of the dispersed nanoparticles, thermal conductivity of alumina nanoparticle (k_p) is 36 W/mK, k_{bf} is the thermal conductivity of the base fluid in liquid medium, and ϕ_v is the equivalent volume fraction of the nanoparticles.

Table 7 shows the measured and predicted thermal conductivity of various ANEP samples at 45°C, and it is compared with Arasu [9] predicted Maxwell model at 47°C. Enhancement of thermal conductivity measurement is slightly higher than the theoretical predicted result. This is attributed to the fact that the interaction between the high-conductive alumina nanoparticles and the matrix molecule affecting the relative thermal conductivity of NEPCMs [17]. The predicted thermal conductivity values of Arasu (@ 47°C) were 1ower than our recent study.

4.3. Comparison of thermal conductivity enhancement of various nanocomposite-based PCMs with present study

4.3.1. Thermal conductivity enhancement of Al_2O_3 nanoparticle-in-octadecane emulsion

Table 8 compares the increase in thermal conductivity of pure paraffin($C_{18}H_{38}$)-nanoparticle composites of various phases with the present study. Relative thermal conductivity enhancement of more than 2 and 6% for the paraffin containing 5 and 10 wt% of alumina nanoparticle at temperature 30°C. The enhancement of thermal conductivity in a liquid state of Al_2O_3 nanoparticle in n-octadecane (W_p = 10 wt%) was found to be more than 17% as the temperature is increased up to 60°C. Thermal conductivity enhancement of Ho and Gao [12] was lower than our present study (**Table 8**). Ho and Gao used n-octadecane with the melting point of 25.1–26.5°C, whereas in the recent study, paraffin wax was used as a phase change material with a melting point of 58–60°C.

Volume fraction (ϕ)	k_{meas} (W/mK)	k_{pred} (W/mK)	Predicted Maxwell model with Arasu (W/mK)
0	0.2375	0.2375	0.12
5 vol%	0.2677	0.2462	0.17
10 vol%	0.2834	0.2559	0.22

Table 7. Measured and calculated ANEP samples at 45°C (solid state).

State	Temperature (°C)	10 vol% ANEP	Temperature (°C)	10 wt%(n-octadecane-alumina emulsion)
Solid	45	19.32%	30	6%
Liquid	65	61%	60	17%

Table 8. Percentage increase in thermal conductivity during solid and liquid phases.

4.3.2. Comparison of thermal conductivity enhancement of 10 wt% CuO nanoparticle enhanced paraffin of different phases with present study (10 vol% of ANEP)

Figure 8 compares the percentage increase in thermal conductivity of 10 wt% CNEP with the present study. Enhancement in thermal conductivity in the liquid state was more pronounced than in the solid state or during phase change.

A maximum of 61% (0.2560 W/mK for ANEP as compared to 0.1590 W/mK for pure paraffin) and 16.35% (0.185 W/mK for CNEP as compared to 0.1590 W/mK for pure paraffin) enhancement of thermal conductivity in the liquid state at 65°C have been achieved in 10 vol% ANEP and 10 wt% CNEP respectively. A maximum of 31.25% (0.42 W/mK for ANEP as compared to 0.32 W/mK for pure paraffin) and 14.37% (0.35 W/mK for CNEP as compared to 0.3060 W/mK for pure paraffin) enhancement of thermal conductivity during phase change (59°C) was achieved in 10 vol% ANEP and 10 wt% CNEP, respectively. A maximum of 19.32% (0.2834 W/mK for ANEP as compared to 0.2375 W/mK for pure paraffin) and 13.04% (0.26 W/mK for CNEP as compared to 0.23 W/mK for pure paraffin) enhancement of thermal conductivity in the solid state at 45°C was found in 10 vol% ANEP and 10 wt% CNEP, respectively. It can be clearly seen that aluminum oxide nanoparticles lead to a higher thermal conductivity enhancement than copper oxide nanoparticles, even though the size of the copper nanoparticles was less than that of the alumina nanoparticles.

4.4. Density of the nanocomposite PCMs

The density of nanocomposite is determined using density-correlation equation developed by Pak and Cho [18].

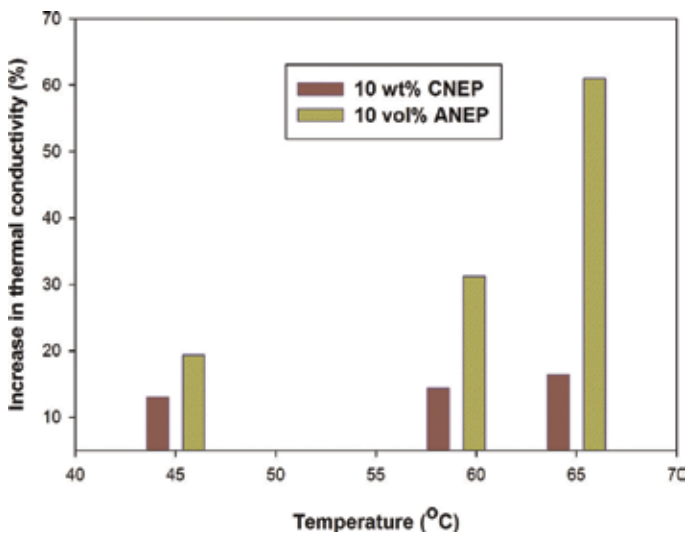

Figure 8. Comparison of percentage increase in thermal conductivity during different phases.

$$\rho_{Nanocomposite} = \varphi\rho_{np} + (1-\varphi)\rho_{bf} \quad (5)$$

where

ρ_{np}—Density of Al_2O_3 nanoparticle, kg/m^3.

ϕ_v—Equivalent volume concentration of alumina nanoparticle.

ρ_{bf}—Density of the base fluid, kg/m^3.

The density of the nanocomposites is calculated using the correlation and is presented in **Table 9**.

Since the density of Al_2O_3 particles is much higher than paraffin wax, the quantity of nano particles replacing equivalent volume of paraffin wax in the composite would add more mass. Hence, the density of nanocomposites increases with increase in volume fraction of nano particles.

4.5. Viscosity measurement

The viscosity of the composite was measured by using Brookfield cone and plate viscometer (LVDV-I PRIME C/P) equipped with a 2.4 cm 0.8°cone supplied by Brookfield Engineering Laboratories, USA, is shown in **Figure 9**. In Brookfield cone and plate viscometer, the cone is connected to the spindle drive, whereas the plate is mounted in the sample cup. Water at a constant temperature of 60°C, 65°C, and 70°C was circulated to the outer surface of the sample cup from a constant temperature hot water bath to prevent the solidification of the samples in the cup, maintain the temperature constant, and measure the viscosity. Measurements were done at three different temperatures for each sample. To measure viscosity in the range of 0.3–1028 cP, spindle CPE-40 was used. Between the plate and cone, a gap of 0.013 is maintained. An adjusting feature of the cone and plate Viscometer is an electronic gap, which is used to place the test fluid in the gap. To rotate the spindle, the viscous drag of the fluid is measured by spring deflection. To attain the temperature equilibrium quickly within a minute, the sample volume required is 0.5–2 ml. To obtain adequate results in spindle/speed combination when applied torque is between 10 and 100% of maximum permissible torque. Measurement can be taken as superfluous if the applied torque does not fall within the possible range. Readings were discarded if the applied torque did not fall within this prescribed range. In cone and plate viscometer, the spindle speed is in the range of 0–100 rpm, and the shear rate is 0–750 s^{-1}.

Volume fraction (ϕ) (vol%)	Equivalent volume fraction (ϕ_v)	Density of nanocomposite (kg/m^3)
5	0.0124	893.976
10	0.0258	930.692

Table 9. Density of nanocomposite.

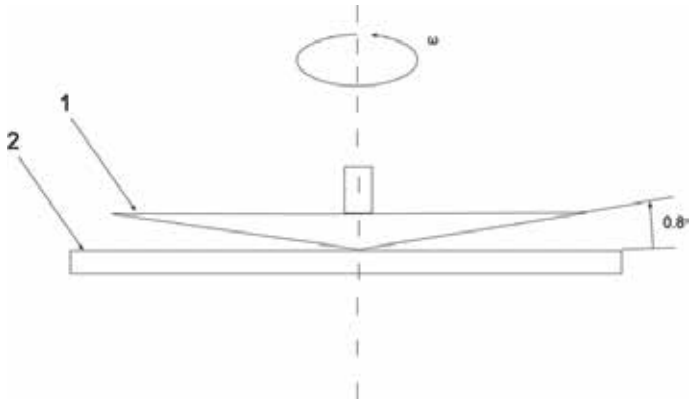

Figure 9. Cone and plate assembly. 1. Cone; 2. Plate.

4.5.1. Experimental measurement on dynamic viscosity

Figure 10 shows the measured dynamic viscosity of paraffin and volume fraction of alumina at various temperatures, respectively. The dynamic viscosity decreases with temperature and increases with an increasing volume fraction of alumina nanoparticles is shown in **Figure 10**. This shows that the addition of nanoparticles makes paraffin more viscous. **Table 10** presents the dynamic viscosity of paraffin and various volume fractions of alumina at different temperatures, respectively. **Figure 10** indicates that the dynamic viscosity has a nonlinear increase with nanoparticle concentration for paraffin-nanoparticle composites. In the liquid state, dynamic viscosity decreases sharply with temperature, while the thermal conductivity has a weak dependence on temperature. For a particular concentration of nanoparticles,

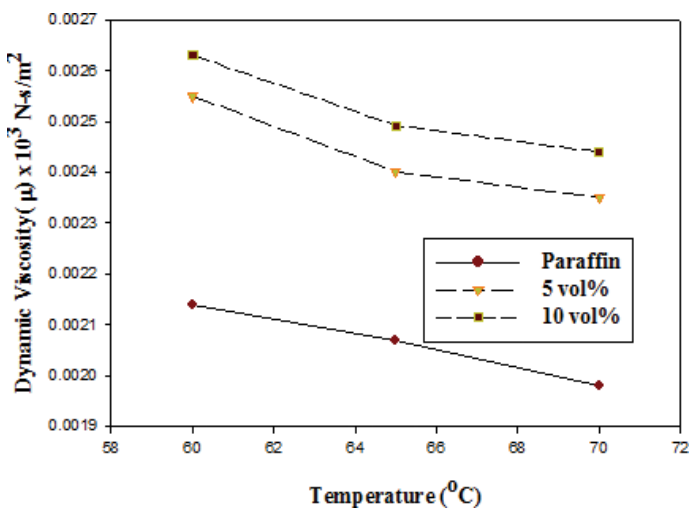

Figure 10. Measured dynamic viscosity for various volume fraction of alumina from 60 to 70°C.

Temperature (°C)	Dynamic viscosity (Cp)		
	Paraffin wax	5 vol%	10 vol%
60	2.14	2.55	2.63
65	2.07	2.401	2.492
70	1.98	2.35	2.44

Table 10. Dynamic viscosity of paraffin and various volume fractions of alumina at different temperature.

Volume fraction (ϕ) (vol%)	Dynamic viscosity of nanocomposite (Ns/m^2)
5	0.2114
10	0.2188

Table 11. Dynamic viscosity of nanocomposite.

the increase in dynamic viscosity is almost the same at different temperatures, while the enhancement of thermal conductivity increases with increase in temperature. So, at higher temperatures, the thermal conductivity enhancement will shoot over the percentage increase in dynamic viscosity.

4.5.2. Comparison of viscosity with Brinkman's correlation

The viscosity of the ANEP samples is predicted using the Brinkman's correlation [19] and is given by:

$$\mu_{Pred} = \mu_{bf} \times \frac{1}{(1-\phi_v)^{2.5}} \tag{6}$$

where μ_{Pred} is predicted viscosity, μ_{bf} is viscosity of the base fluid, and ϕ_v is the eqivalent volume fraction of particles in base fluid. The dynamic viscosity of the composites is shown in **Table 11**. From **Table 11**, it is depicted that dynamic viscosity increases with increase in volume concentration of the nanoparticle.

5. Conclusion(s)

1. Nanoparticle enhanced paraffin composites were then prepared by dispersing the aluminum oxide nanoparticles in liquid paraffin under the intense signification to make the mixture stable.
2. The effect of nanoparticle volume concentration and the temperature was also investigated. Differential scanning calorimetry reveals that there is only one peak during meting/freezing cycle in paraffin/alumina composites and latent heat decreased with the addition of alumina nanoparticles compared to paraffin wax. There is no significant difference in latent heat value between the 10 vol% ANEP and 10 wt% CNEP.

3. Relative thermal conductivity enhancement of Ho and Gao (17%) was lower than our present study. Compared to Ho and Gao, the latent heat of paraffin/alumina composites was nearly 8 and 14%.
4. It was found that increase in thermal conductivity of ANEP is consistently higher than that of CNEP. The maximum increase in thermal conductivity (61%) was observed for 10 vol% ANEP in the liquid state at 65°C. The maximum increase in dynamic viscosity (23%) was observed for 10 vol% ANEP at 70°C.
5. Maxwell's model of the predicted result (k = 0.22 W/mK @ 47°) in Arasu was higher than that of recent studies (k = 0.2559 W/mK @ 45°)

6. Final suggestion

This chapter is presented to be only a baseline study to study the charging and discharging characteristics of horizontal double pipe latent heat energy storage system. This is a very important topic and will be addressed in later chapter.

Nomenclature

A	external surface area of heat transfer fluid pipe (m^2)
C_p	specific heat of PCM/alumina (kJ/kg°C)
H	latent heat of paraffin/composite (J/g or kJ/kg)
M	mass of PCM (kg)
T	temperature (°C)
t	time (min)

Greek symbols

μ	dynamic viscosity of paraffin wax(kg/m s)
ρ	density (kg/m^3)
W	weight
ϕ	volume fraction
Ψ	thermal conductivity enhancement ratio

Subscripts

eff	effective
bf	base fluid
m	melting temperature/composite

v	volume fraction or volume
l	liquid
s	solid
w	water
f	freezing temperature
c	nanocomposite
p	paraffin wax/copper oxide nanoparticle/alumina nanoparticle
k	thermal conductivity (W/m K)

Abbreviations

DSC	differential scanning calorimetry
LHTESS	latent heat thermal energy storage system
ANEP	alumina nanoparticle enhanced paraffin
CNEP	copper-oxide nanoparticle enhanced paraffin
PCM	phase change material

Author details

Ponnuraj Stella Jesumathy

Address all correspondence to: jesumathy81@gmail.com

Independent Scientist, Erode, India

References

[1] Francis A, Neil H, Philip E. A review of materials, heat transfer and phase change problem formulation for latent heat thermal energy storage systems (LHTESS). Renewable Sustainable Energy Review. 2010;**14**:615-628

[2] Atul S, Tyagi VV, Chen CR. Review on thermal energy storage with phase change materials and applications. Renewable Sustainable Energy Review. 2009;**13**:318-345

[3] Zalba B, Martin JM, Cabeza LF, Mehling H. Review on thermal energy storage with phase change: Materials, heat transfer analysis and applications. Applied Thermal Engineering. 2003;**23**:251-283

[4] Shukla A, Buddhi D, Sawhney RL. Solar water heaters with phase change material thermal energy storage medium. Renewable Sustainable Energy Review. 2009;**13**(8):2119-2125

[5] Jesumathy S, Udayakumar M, Suresh S. Experimental study of enhanced heat transfer by addition of CuO nanoparticle. Heat and Mass Transfer. 2012;**48**:965-978

[6] Elgafy A, Lafdi K. Effect of carbon nanofiber additives on thermal behavior of phase change materials. Carbon. 2005;**43**(15):3067-3074

[7] Jegadheeswaran PSD. Performance enhancement of latent heat thermal storage system: A review. Renewable and Sustainable Energy Reviews. 2009;**13**:2225-2244

[8] Zeng JL, Zhu FR, Yu SB, Zhu L, Cao Z, Sun LX, Deng GR, Yan WP, Zhang L. Effects of copper nanowires on the properties of an organic phase change material. Solar Energy Materials and Solar Cells. 2012;**105**:174-178

[9] Arasu AV, Agus Sasmito P, Arun MS. Numerical study of paraffin wax dispersed with alumina in a concentric pipe latent heat storage system. Thermal Science. 2013;**17**(2):419-430

[10] Arasu AV, Agus Sasmito P, Arun Mujumdar S. Numerical evaluation of laminar heat transfer enhancement in nanofluid flow in coiled square tubes. Nanoscale Research Letters. 2011;**6**(1):376

[11] Aydin AA, Okutan H. High chain fatty acid esters of myristyl alcohol with odd carbon number: Novel organic phase change materials for thermal energy storage-2. Solar Energy Materials and Solar Cells. 2011;**95**:2417-2423

[12] Ho CJ, Gao JY. Preparation and thermophysical properties of nanoparticles in paraffin emulsions phase change material. International Communications in Heat and Mass Transfer. 2009;**36**:467-470

[13] Kim S, Drzal LT. High latent heat storage and high thermal conductive phase change materials using exfoliated graphite nanoplatelets. Solar Energy Material and Solar Cells. 2009;**93**:136-142

[14] Chandrasekar M, Suresh S, Chandra Bose A. Experimental investigation and theoretical determination of thermal conductivity and viscosity of Al_2O_3/water nanofluid. Experimental Thermal and Fluid Science. 2010;**34**:210-216

[15] Wang J, Xie H, Xin Z, Li Y, Chen L. Enhancing thermal conductivity of palmitic acid based phase change materials with carbon nanotubes as fillers. Solar Energy. 2010;**84**:339-344

[16] Hashin Z, Shtrikman S. A variational approach to the theory of the effective magnetic permeability of multiphase materials. Journal of Applied Physics. 1962;**33**:3125-3131

[17] Xue Q. Model for effective thermal conductivity of nanofluids. Physics Letters. 2003; **307**:313-317

[18] Pak BC, Cho YI. Hydrodynamic and heat transfer study of dispersed fluids with submicron metallic oxide particles. Experimental Heat Transfer. 1998;**11**:151-170

[19] Brinkman HC. The viscosity of concentrated suspensions and solutions. Chemical Physics. 1952;**20**:571

Section 5

Applications of Phase Change Material

Chapter 5

Thermodynamic Properties of the Polyols as Phase Change Materials for Thermal Energy Storage

Zhicheng Tan, Quan Shi and Xin Liu

Additional information is available at the end of the chapter

http://dx.doi.org/10.5772/intechopen.78800

Abstract

In this chapter, four natural polyhydroxy alcohols (polyols), including xylitol, sorbitol, adonitol, and erythritol were selected as the subject of study on phase change materials for thermal energy storage application. The thermodynamic study on these polyols was performed by adiabatic calorimetry (AC), differential scanning calorimetry (DSC), and thermogravimetric analysis (TG). The heat capacities of these polyols were measured in the temperature range from 80 to 400 K by a fully automated high-precision adiabatic calorimeter. The experimental heat capacities of these polyols were fitted to the polynomial equations of heat capacities as a function of temperatures. The thermodynamic property data, such as temperatures, enthalpies, and entropies of the phase transitions, were obtained based on the experimental heat capacities in the phase transition temperature range. According to the thermodynamic relation equations, the standard thermodynamic functions of these polyols, relative to the standard reference temperature 298.15 K, $[H_T–H_{298.15}]$ and $[S_T–S_{298.15}]$, were calculated with the interval of 5 K. The thermal stability and heat storage capacity of the polyols were also investigated by thermal analysis.

Keywords: phase change material (PCM), polyhydroxy alcohol (polyol), natural polyol, thermodynamic properties, heat capacity, temperature of phase transition, enthalpy and entropy of phase transition, adiabatic calorimetry (AC), thermal analysis, DSC, TG

1. Introduction

In recent two decades, the phase change materials (PCMs) have attracted much attention due to their remarkable effects to thermal energy storage applications. It has been demonstrated that the research of PCMs is becoming one of the most hot research topic in the world. The basic theory of PCMs application is utilizing the heat energy being absorbed or released when

the phase transition processes take place at a constant temperature. Consequently, the thermodynamic properties of PCMs, especially the heat capacity, phase transition temperature, and enthalpy would play a crucial role in both theoretically and technically investigating the thermal energy storage unit and its performance by using PCMs [1].

Thermal energy storage technology has wide application prospects in solar energy utilization, power generation, waste heat recovery, and utilization. Phase change material is the prerequisite for the development of thermal energy storage system, so the study of phase change materials for latent thermal energy storage application is the core subject in this field.

The polyhydroxy alcohols (polyols) have multiple hydroxyl structures, so hydrogen bonds can be formed between the molecules, and then the enthalpy of phase transition is larger. Polyols as heat storage material have many advantages, such as high phase change enthalpy, wide phase change temperature range, high mass heat storage capacity, lower super cooling degree, long service life, nontoxic, noncorrosive, etc. [2]. Therefore, as a new kind of PCMs for energy storage, polyols have been paid more and more attention. The research on basic theory and practical application of polyols has been widely carried out in the world [3–25].

The thermodynamic properties are significant for practical application of PCMs in thermal energy storage. Hence, the thermodynamic studies of PCMs have been performed in our thermochemistry laboratory for nearly 20 years long [1]. In the last decade, we have carried out the thermodynamic study of polyol as phase change materials [2]. A series of polyols, which are easily obtained and have great technical and economic potential for application, were selected as PCMs for energy storage application. The thermodynamic properties of these polyols were studied in detail using high-precision automatic adiabatic calorimeter (AC), differential scanning calorimeter (DSC), and thermogravimetric analyzer (TG), respectively [2, 16–23].

In this chapter, we report our research results on thermodynamic properties of four natural polyols: xylitol, sorbitol, adonitol, and erythritol, and introduce the modern advanced experimental calorimetric techniques used for thermodynamic studies of phase change materials.

2. Experimental

2.1. Adiabatic calorimetry and heat capacity measurements

Adiabatic calorimetry is the most accurate approach to obtain the heat capacity data. In the present study, heat capacity measurements were carried out by a high-precision automatic adiabatic calorimeter over the temperature range 80–400 K. The adiabatic calorimeter was established by Thermochemistry Laboratory of Dalian Institute of Chemical Physics, Chinese Academy of Sciences in PR China. The structure and principle of the adiabatic calorimeter have been described in detail elsewhere [26, 27]. The schematic diagram of the adiabatic calorimeter is shown in **Figure 1**. Briefly, the automatic adiabatic calorimeter is mainly composed of a sample cell, a miniature platinum resistance thermometer, an electric heater, the inner and outer adiabatic shields, two sets of six-junction chromel-constantan thermopiles installed between the calorimetric cell and the inner shield and between the inner and the

http://dx.doi.org/10.5772/intechopen.78800

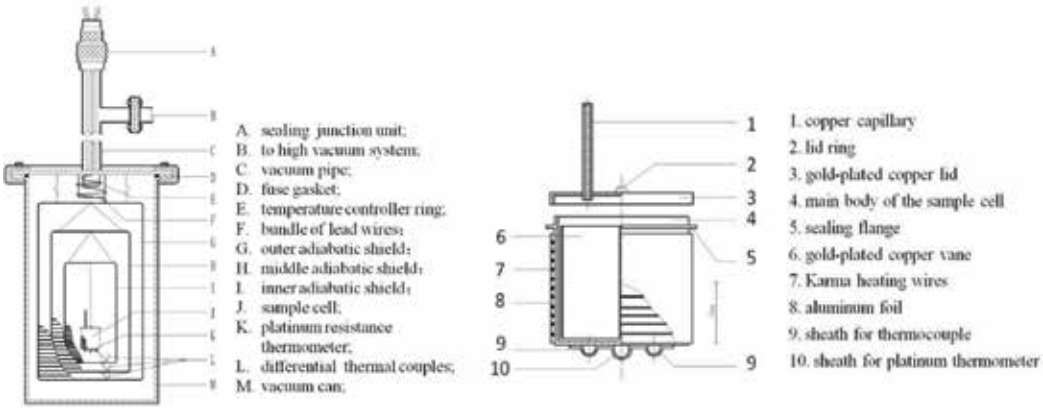

Figure 1. Schematic diagram of main body of the adiabatic calorimeter (left); schematic diagram of sample cell of the adiabatic calorimeter (right).

outer shields, respectively, and a high vacuum can. The working temperature range is 78–400 K and, if necessary, it can be cooled by liquid nitrogen. The heat capacity measurements were conducted by the standard procedure of intermittently heating the sample and alternately measuring the temperature. The heating rate and the temperature increments of the experimental points were generally controlled at 0.1–0.4 $K \cdot min^{-1}$ and at 1–4 K, respectively, during the whole experimental process. The heating duration was 10 min, and the temperature drift rates of the sample cell measured in an equilibrium period were kept within 10^{-3}–10^{-4} $K \cdot min^{-1}$ during the acquisition of heat capacity data.

In order to verify the reliability of the adiabatic calorimeter, the molar heat capacities $C_{p,m}$ of the Standard Reference Material (SRM-720) (α-Al_2O_3) were measured in the range from 78 to 400 K. The deviation of our calibration data from those of NIST [28] was within ±0.1% (standard uncertainty).

In the present study, the heat capacity measurements were conducted by means of the standard method of intermittently heating the sample and alternately measuring the temperature. The temperature difference between the sample and adiabatic shield was automatically kept to be about 10^{-3} K during the whole experiment. The temperature increment for a heating period was about 3 K, and temperature drift was maintained about 10^{-4} $K \cdot min^{-1}$ during each equilibrium period. The data were automatically collected through a Data Acquisition/Switch Unit (Model: 34420, Agilent USA) and processed online by a personal computer according to the program developed in our thermochemistry laboratory [26].

2.2. DSC and TG analysis

A differential scanning calorimeter (Model: DSC141, SETARAM, France) was used to perform the thermal analysis of the natural polyols under high-purity nitrogen (99.999%) with a flow rate of 40 $ml \cdot min^{-1}$ and heating rate of 10 $K \cdot min^{-1}$. The DSC141 was calibrated with indium and zinc standards.

The thermogravimetric measurements of the natural polyols were carried out by a TG analyzer (Model: Setaram setsys 16/18, SETARAM, France) under high-purity nitrogen (99.999%) with a flow rate of 40 ml·min^{-1} and heating rate of 10 K·min^{-1}. The TG analyzer was calibrated by calcium oxalate standards.

3. Thermodynamic properties of nature xylitol: $C_5H_{12}O_5$ [$(CH_2\ OH)(CHOH)_3\ (CH_2OH)$, CAS No. 87-99-0]

3.1. Sample

The xylitol sample was purchased from ACROS ORGANICS company with labeled purity >99% mass fraction. The sample was recrystallized and then purified by sublimation. It was handled in a dry N_2 atmosphere to avoid possible contamination by moisture. The chemical structure of xylitol is as follows:

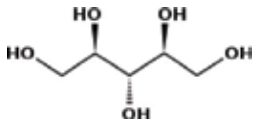

The mass of the xylitol sample, used for heat capacity measurement was 4.87213 g, which is equivalent to 32.022 m mol based on its molar mass of 152.1457 g·mol^{-1}.

The mass of the xylitol sample used in the DSC experiment was 3.48 mg, and in the TG analysis was 8.35 mg, respectively.

3.2. Results and discussion

3.2.1. Heat capacity

Experimental molar heat capacities of xylitol measured by the adiabatic calorimeter over the temperature range from 80 to 390 K are plotted in **Figure 2**. From **Figure 2**, a phase transition was observed in the range of 360–375 K with the peak heat capacity at 369.04 K. According to its melting point 365.7 K [7], this transition corresponds to a solid-liquid phase change.

The values of experimental heat capacities can be fitted to the following polynomial equations with least square method:

For the solid phase over the temperature range 80–360 K:

$$C^0_{p,m}/\mathrm{J\cdot K^{-1}\cdot mol^{-1}} = 165.87 + 105.19x + 1.8011x^2 - 41.445x^3 - 41.851x^4 + 65.152x^5 + 66.744x^6 \quad (1)$$

where X is the reduced temperature x = [T − (T_{max} + T_{min})/2]/[(T_{max} − T_{min})/2], T is the experimental temperature, thus, in the solid state (80–360 K), x = [(T/K) − 220]/140, T_{max} is the upper limit (360 K) and T_{min} is the lower limit (80 K) of the above temperature region. The correlation coefficient of the fitting R^2 = 0.9947.

For the liquid phase over the temperature range 370–390 K:

$$C^0_{p,m}/\mathrm{J\cdot K^{-1}\cdot mol^{-1}} = 426.19 + 5.6366x \tag{2}$$

where x is the reduced temperature, x = [(T/K) − 380]/10, T is the experimental temperature, 380 is obtained from polynomial $(T_{max} + T_{min})/2$, 10 is obtained from polynomial $(T_{max} - T_{min})/2$. T_{max} and T_{min} are the upper (390 K) and lower (370 K) limit temperatures, respectively. The correlation coefficient of the fitting R^2 = 0.993.

3.2.2. The temperature, enthalpy, and entropy of solid-liquid phase transition

The standard molar enthalpy and entropy of the solid-liquid transition $\Delta_{fus}H^0_m$ and $\Delta_{fus}S^0_m$ of the compound were derived according to Eqs. (3) and (4):

$$\Delta_{fus}H^0_m = \frac{Q - n\int_{T_i}^{T_m} C^0_{p,m}(s)dT - n\int_{T_m}^{T_f} C^0_{p,m}(l)dT - \int_{T_i}^{T_f} H^0 dT}{n} \tag{3}$$

$$\Delta_{fus}S^0_m = \frac{\Delta_{fus}H^0_m}{T_m} \tag{4}$$

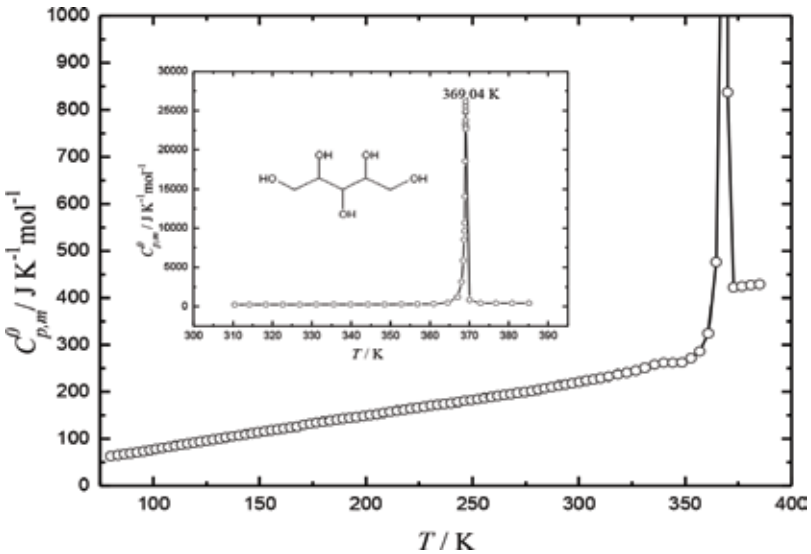

Figure 2. Experimental molar heat capacity of xylitol as a function of temperature.

where T_i is the temperature that is somewhat lower than the temperature of the onset of a solid-liquid transition and T_f is the temperature slightly higher than that of the transition completion. Q is the total energy introduced into the sample cell from T_i to T_f, H^0, the standard heat capacity of the sample cell from T_i to T_f, $C^0_{p,m}$ (s), the standard heat capacity of the sample in solid phase from T_i to T_m, $C^0_{p,m}$ (l), the standard heat capacity of the sample in liquid phase from T_m to T_f, and n is the molar amount of the sample. The heat capacity polynomials mentioned above were used to calculate the smoothed heat capacities, and were numerically integrated to obtain the values of the standard thermodynamic functions above T = 298.15 K. The calculated results can be found in our previous publication [17].

The thermodynamic functions of the xylitol relative to the reference temperature 298.15 K were calculated in the temperature range 80–390 K with an interval of 5 K, using the polynomial equation of heat capacity and thermodynamic relationships as follows:

Before melting,

$$H^0_T - H^0_{298.15} = \int_{298.15}^{T} C^0_{p,m}(s)dT \tag{5}$$

$$S^0_T - S^0_{298.15} = \int_{298.15}^{T} \frac{C^0_{p,m}(s)}{T}dT \tag{6}$$

After melting,

$$H^0_T - H^0_{298.15} = \int_{298.15}^{T_i} C^0_{p,m}(s)dT + \Delta_{fus}H^0_m + \int_{T_f}^{T} C^0_{p,m}(l)dT \tag{7}$$

$$S^0_T - S^0_{298.15} = \int_{298.15}^{T} [\frac{C^0_{p,m}(s)}{T}]dT + \frac{\Delta_{fus}H^0_m}{T_m} + \int_{T_f}^{T} [\frac{C^0_{p,m}(l)}{T}]dT \tag{8}$$

where T_i is the temperature at which the solid-liquid phase transition started; T_f is the temperature at which the solid-liquid phase transition ended; $\Delta_{fus}H^0_m$ is the standard molar enthalpy of fusion; T_m is the temperature of solid-liquid phase transition. The standard thermodynamic functions, $H^0_T - H^0_{298.15}$ and $S^0_T - S^0_{298.15}$ can be consequently calculated based on the equations [17].

3.2.3. The result of TG and DSC analysis

From the DSC curve in **Figure 3**, a sharply endothermic peak corresponding to melting process was observed, with the peak temperature of 367.52 K and the enthalpy of 33.68 ± 0.34 kJ·mol^{-1}, which are consistent with the values 369.04 K, 33.26 ± 0.17 kJ·mol^{-1} observed from the adiabatic calorimetric measurements. The results were listed in Ref. [17], from which, it can be seen that the standard thermodynamic parameters obtained from adiabatic calorimetry and DSC in the present research are in accordance with each other and slightly lower than those reported in literature [4].

http://dx.doi.org/10.5772/intechopen.78800

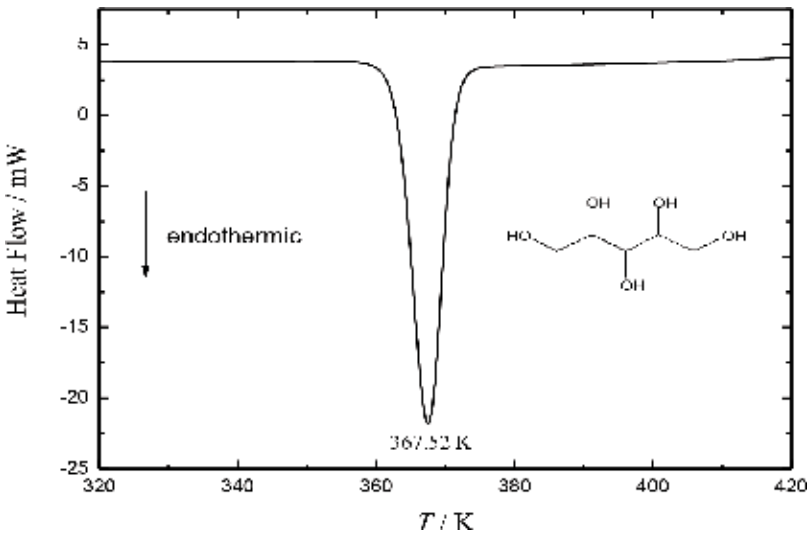

Figure 3. DSC curve of xylitol under high-purity nitrogen.

From the TG curve in **Figure 4**, it can be seen that the mass loss of the sample was completed in a single step. The sample keeps thermostable below 400 K. It begins to lose weight at 451.20 K, reaches the maximum rate of weight loss at 617.13 K, and completely loses its weight when the temperature reaches 675.30 K.

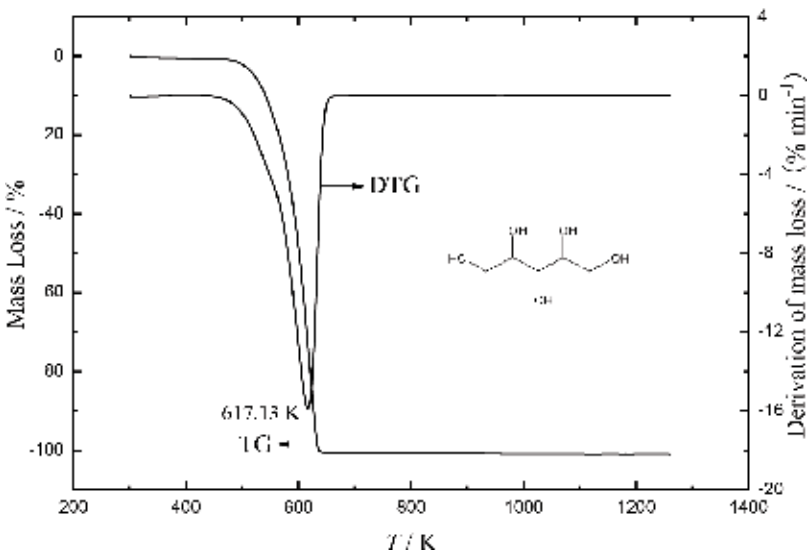

Figure 4. TG-DTG curve of xylitol under high-purity nitrogen.

4. Thermodynamic properties of nature sorbitol: $C_6H_{14}O_6$ [$(CH_2OH)(CHOH)_4(CH_2OH)$, CAS No. 50-70-4]

4.1. Sample

The sorbitol sample was purchased from YuanJu Bio-Tech Co. Ltd. Shanghai, in PR China with batch number 040603 and labeled purity >99.0% mass fraction. The sample was recrystallized and then purified by sublimation. It was handled in a dry N_2 atmosphere to avoid possible contamination by moisture.

The chemical structure of sorbitol is as follows:

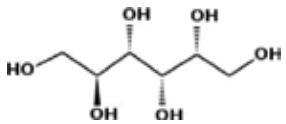

The mass of the sorbitol sample used for the heat capacity measurement is 3.71682 g, which is equivalent to 20.403 m mol based on its molar mass of 182.17165 g·mol^{-1}.

The mass of the sorbitol sample used in the DSC and TG experiment is 3.01 mg and 13.15 mg, respectively.

4.2. Results and discussion

4.2.1. Heat capacity

Experimental molar heat capacities of sorbitol measured by the adiabatic calorimeter over the temperature range from 80 to 390 K are listed in Ref. [18] and plotted in **Figure 5**. From **Figure 5**, a phase transition was observed in the range of 360–375 K with a peak temperature of 369.157 K. According to its melting point 366.5 K [7], this transition corresponds to a solid-liquid phase change.

The values of experimental heat capacities can be fitted to the following polynomial equations with least square method:

For the solid phase over the temperature range 80–355 K:

$$C_{p,\,m}/J \cdot K^{-1} \cdot mol^{-1} = 170.17 + 157.75x + 128.03x^2 - 146.44x^3 - 335.66x^4 + 177.71x^5 + 306.15x^6 \quad (9)$$

where X is the reduced temperature $x = [T - (T_{max} + T_{min})/2]/[(T_{max} - T_{min})/2]$, T is the experimental temperature, thus, in the solid state (80–355 K), $x = [(T/K) - 217.5]/137.5$, T_{max} is the upper limit (355 K) and T_{min} is the lower limit (80 K) of the above temperature region. The correlation coefficient of the fitting $R^2 = 0.9966$.

For the liquid phase over the temperature range 375–390 K:

$$C_{p,\,m}/\mathrm{J}\cdot\mathrm{K}^{-1}\cdot\mathrm{mol}^{-1} = 518.13 + 3.2819\,x \tag{10}$$

where x is the reduced temperature, x = [(*T*/K)−382.5]/7.5, *T* is the experimental temperature, 382.5 is obtained from polynomial $(T_{max} + T_{min})/2$, 7.5 is obtained from polynomial $(T_{max} - T_{min})/2$. T_{max} and T_{min} are the upper (390 K) and lower (375 K) limit temperatures, respectively. The correlation coefficient of the fitting $R^2 = 0.9968$.

The heat capacity polynomials (9), (10) were used to calculate the smoothed heat capacities, and were numerically integrated to obtain the values of the standard thermodynamic functions above *T* = 298.15 K. The calculated results are listed in Ref. [18].

4.2.2. The temperature, enthalpy, and entropy of solid-liquid phase transition

The molar enthalpies and entropies of the solid-liquid phase transition $\Delta f_{us}H_m$ and $\Delta f_{us}S_m$ of sorbitol were derived according to the thermodynamic equations (see Section 4.2.2 in this chapter). The derived thermodynamic parameters were listed in Ref. [18].

4.2.3. Thermodynamic functions of sorbitol

The thermodynamic functions of the sorbitol relative to the reference temperature 298.15 K were calculated in the temperature range 80–390 K with an interval of 5 K, using the polynomial equations of heat capacity (9), (10) and thermodynamic relationships (see Section 2.2.2. in this chapter).

The calculated thermodynamic functions, H_T–$H_{298.15}$, S_T–$S_{298.15}$, are listed in Ref. [18].

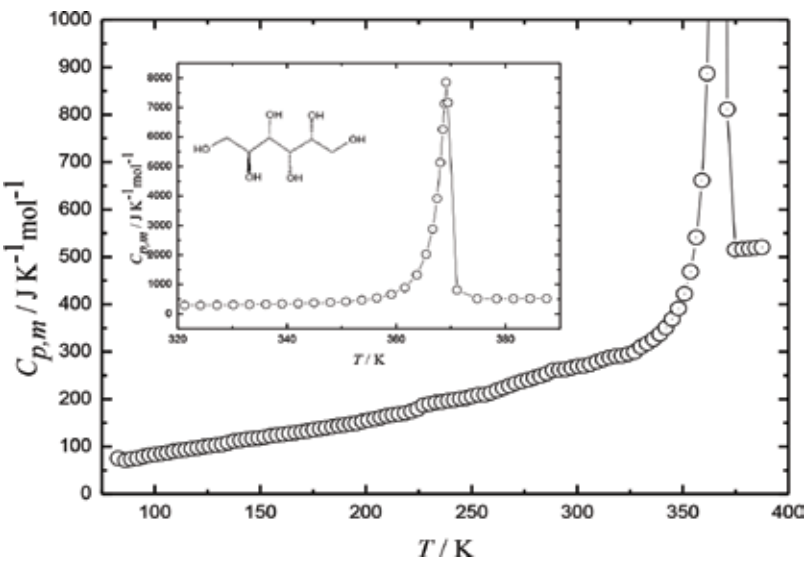

Figure 5. Experimental molar heat capacity of sorbitol as a function of temperature.

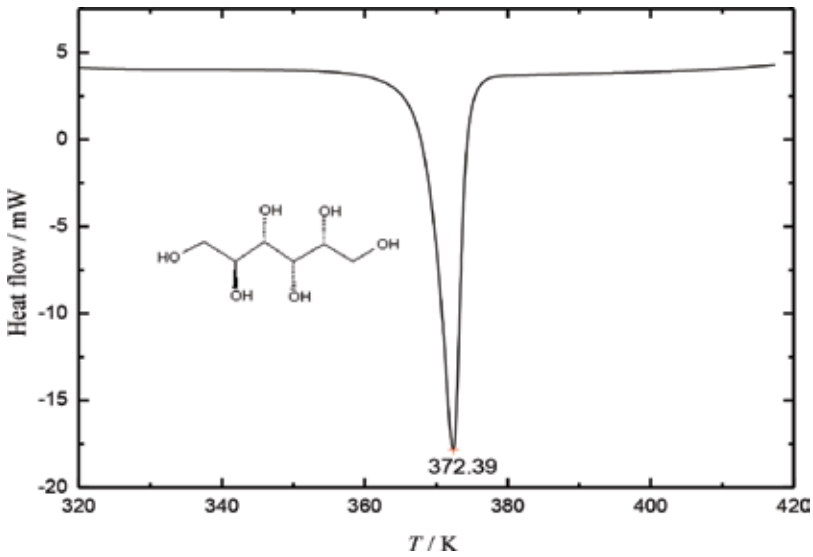

Figure 6. DSC curve of sorbitol under high-purity nitrogen.

4.2.4. The result of TG and DSC analysis

From the DSC curve in **Figure 6**, a sharply endothermic peak corresponding to melting process was observed, with the peak temperature of 372.39 K and the enthalpy of 30.66 ± 0.31 kJ·mol^{-1}, which are consistent with the values (369.157 K, 30.35 ± 0.15 kJ·mol^{-1}) observed from the adiabatic calorimetric measurements. The results were listed in Ref. [18], from which it can be seen that the thermodynamic parameters obtained from adiabatic calorimetry and DSC in the present research are in accordance with each other and slightly higher than those reported in literature [7].

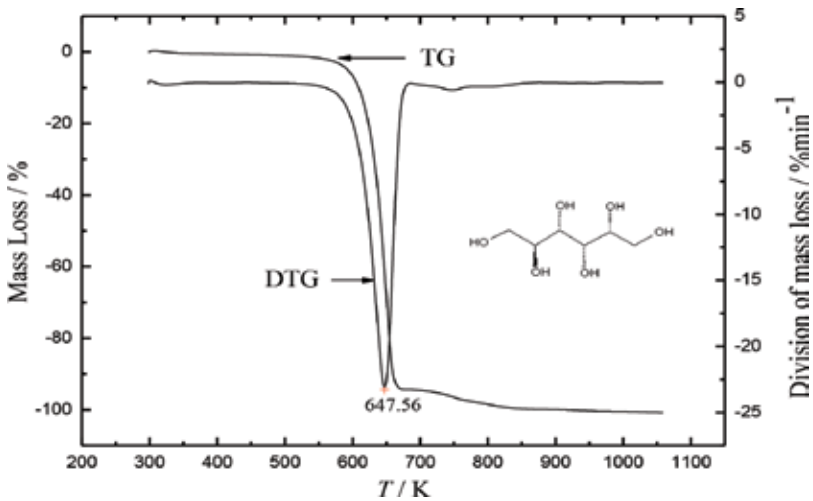

Figure 7. TG-DTG curve of sorbitol under high-purity nitrogen.

From the TG-DTG curve in **Figure 7**, it can be seen that the mass loss of the sample was completed in a single step. The sample keeps thermostable below 500 K. It begins to lose weight at 529.50 K, reaches the maximum rate of weight loss at 647.56 K, and completely loses its weight when the temperature reaches 764.50 K.

5. Thermodynamic properties of nature adonitol: $C_5H_{12}O_5$ [$(CH_2OH)(CHOH)_3(CH_2OH)$, CAS No. 488-81-3]

5.1. Sample

The adonitol sample was purchased from ACROS ORGANICS Company with labeled purity of 99.0% mass fraction and was handled in a dry N_2 atmosphere to avoid possible contamination by moisture. GC analyses of the samples gave purities >99.0% in agreement with their specifications. The sample was used without additional purification. The chemical structure of adonitol is as follows:

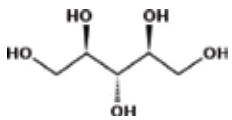

The sample amount used for the heat capacity measurement is 2.27977 g, which is equivalent to 14.984 mmol based on its molar mass of 152.1457 $g \cdot mol^{-1}$.

The mass of the sample used in the DSC experiment was 6–8 mg.

The mass of the sample used in the TG experiment was 11.72 mg.

5.2. Results and discussion

5.2.1. Heat capacity

Experimental molar heat capacities of adonitol measured by the adiabatic calorimeter over the temperature range from 78 to 400 K are listed in Ref. [21] and plotted in **Figure 8**. From **Figure 8**, a phase transition was observed at the peak temperature of 369.08 K. According to its melting point 374.7 K [7], this transition corresponds to a solid-liquid phase change. The values of experimental heat capacities can be fitted to the following polynomial equations with least square method: For the solid phase over the temperature range 78–360 K:

$$C^0_{p,m}/\mathrm{J \cdot K^{-1} \cdot mol^{-1}} = 170.000 + 98.817x + 23.846x^2 - 56.366x^3 - 92.259x^4 + 71.865x^5 + 82.678x^6 \quad (11)$$

where x is the reduced temperature $x = [T - (T_{max} + T_{min})/2]/[(T_{max} - T_{min})/2]$, T is the experimental temperature, thus, in the solid state (78–360 K), $x = [(T/K) - 219]/141$, T_{max} is the

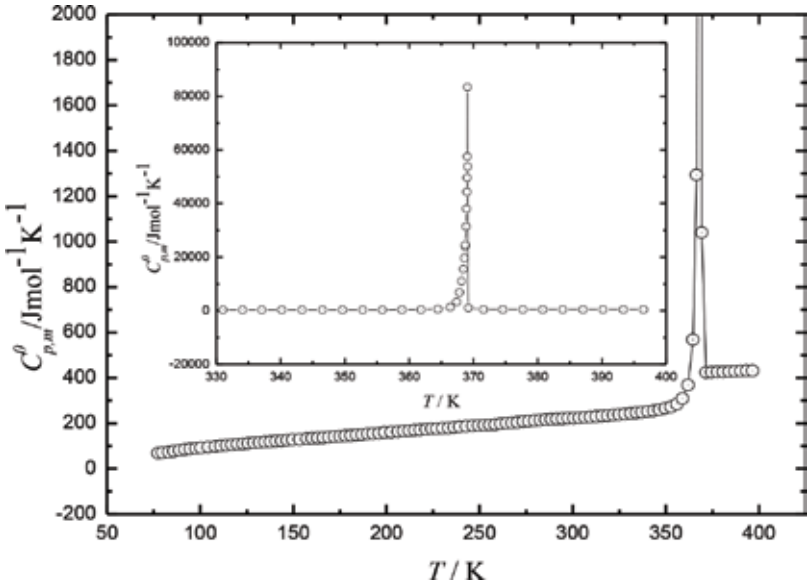

Figure 8. Experimental molar heat capacity of adonitol as a function of temperature.

upper limit (360 K), and $T_{\min}$ is the lower limit (78 K) of the above temperature region. The correlation coefficient of the fitting $R^2 = 0.9986$.

For the liquid phase over the temperature range 375–400 K:

$$C^0_{p,m}/\mathrm{J}\cdot\mathrm{K}^{-1}\cdot\mathrm{mol}^{-1} = 428.460 + 3.821\mathrm{x} \tag{12}$$

where x is the reduced temperature, x = [(*T*/K) − 387.5]/12.5, *T* is the experimental temperature, 387.5 is obtained from polynomial $(T_{\max} + T_{\min})/2$, 12.5 is obtained from polynomial $(T_{\max} - T_{\min})/2$. $T_{\max}$ and $T_{\min}$ are the upper (400 K) and lower (375 K) limit temperatures, respectively. The correlation coefficient of the fitting $R^2 = 0.9954$.

5.2.2. The temperature, enthalpy, and entropy of solid-liquid phase transition

The molar enthalpies and entropies of the solid-liquid phase transition $\Delta f_{\mathrm{us}}H_{\mathrm{m}}$ and $\Delta f_{\mathrm{us}}S_{\mathrm{m}}$ of adonitol were derived according to the thermodynamic equations (see Section 2.2.2 in this chapter). The derived thermodynamic parameters were listed in Ref. [21].

5.2.3. Thermodynamic functions of adonitol

The thermodynamic functions of the adonitol relative to the reference temperature 298.15 K were calculated in the temperature range 80–400 K with an interval of 5 K, using the polynomial equations of heat capacity (11), (12) and thermodynamic relationships (see Section 3.2.2. in this chapter).

The calculated thermodynamic functions, $H_{\mathrm{T}} - H_{298.15}$ and $S_{\mathrm{T}} - S_{298.15}$, are listed in Ref. [21].

5.2.4. The result of TG and DSC analysis

From the DSC curve in **Figure 9**, a sharply endothermic peak corresponding to melting process was observed, with the melting temperature of 373.61 ± 0.55 K and the enthalpy of 38.89 ± 1.17 kJ·mol^{-1}, which are slightly higher than the values 369.08 K, 36.42 ± 0.18 kJ·mol^{-1} observed from the adiabatic calorimetric measurements and slightly lower than the values

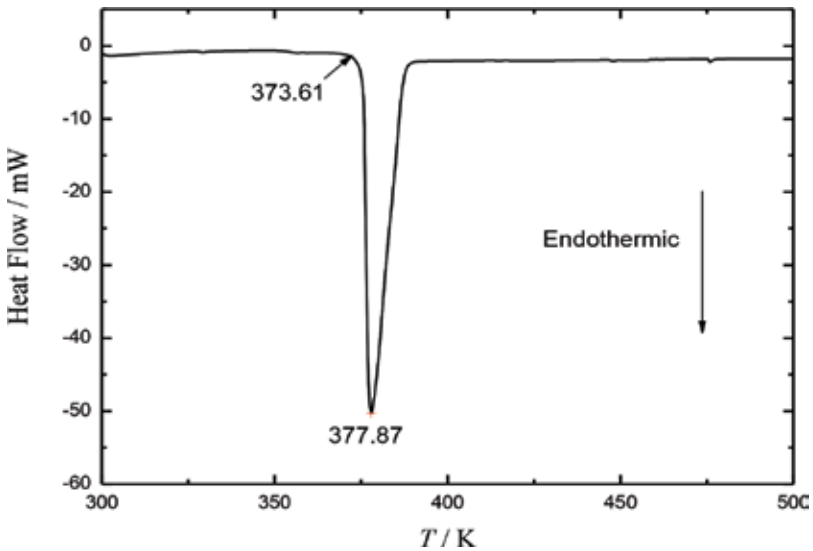

Figure 9. DSC curve of adonitol under high-purity nitrogen.

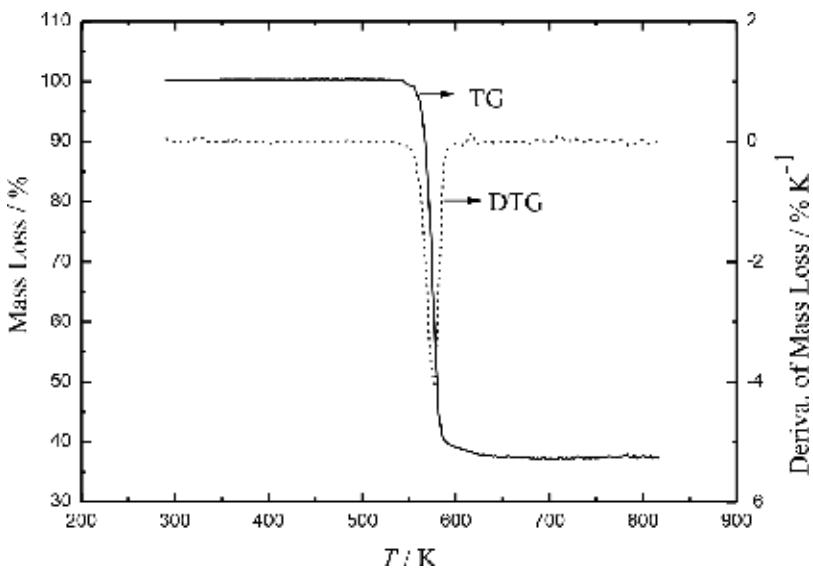

Figure 10. TG-DTG curve of adonitol under high-purity nitrogen.

observed from DSC (374.7 K, 37.6 kJ·mol^{-1}) from G. Barone et al. in literature [7]. The results were listed in Ref. [21]. The data from DSC are obtained at a 10 K·min^{-1} scanning rate, in which the sample could not reach thermal balance. However, the data of adiabatic calorimetry are obtained by means of the standard method of intermittently heating the sample and alternately measuring the temperature. The temperature difference between the sample and adiabatic shield was automatically kept to be about 10^{-3} K during the whole experiment. The temperature increment for a heating period was about 3 K, and temperature drift was maintained about 10^{-4} Kmin^{-1} during each equilibrium period. Therefore, this process is much more near to "adiabatic" and "balanced" than DSC method. Generally, the phase change temperature obtained from AC is lower than that from DSC.

From the TG-DTG curve in **Figure 10**, it can be seen that the mass loss of the sample was completed in a single step. The sample keeps thermostable below 550 K. It begins to lose weight at 551.55 K, reaches the maximum rate of weight loss at 577.38 K, and completely loses its weight when the temperature reaches 601.82 K.

6. Thermodynamic properties of nature erythritol: $C_4H_{10}O_4$ [$(CH_2OH)(CHOH)_2(CH_2OH)$, CAS No. 149-32-6]

6.1. Sample

The erythritol sample was purchased from Shandong Baolingbao Biotechnology Co. Ltd. in PR China with batch number 060715 and labeled purity >99.0% mass fraction. The sample was recrystallized and then purified by sublimation. It was handled in a dry N_2 atmosphere to avoid possible contamination by moisture. Erythritol's molecular formula is $C_4H_{10}O_4$ with molar mass of 122.11975 g·mol^{-1} and structural formula as follows:

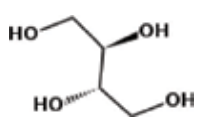

The mass of the erythritol sample used for the heat capacity measurement is 4.76575 g, which is equivalent to 39.025 m mol based on its molar mass of 122.11975 g·mol^{-1}. The mass of the erythritol sample used in the DSC experiment was 9.70 mg. The mass of the erythritol sample used in the TG measurements was 18.35 mg.

6.2. Results and discussion

6.2.1. Heat capacity

Experimental molar heat capacities of erythritol measured by the adiabatic calorimeter over the temperature range from 80 to 410 K are listed in Ref. [20] and plotted in **Figure 11**. From

Figure 11, a phase transition was observed in the temperature range of 385–395 K with a peak temperature of 390.254 K.

The values of experimental heat capacities can be fitted to the following polynomial equations with least square method:

For the solid phase over the temperature range 80–385 K:

$$C_{p,\mathrm{m}}/\mathrm{J}\cdot\mathrm{K}^{-1}\cdot\mathrm{mol}^{-1} = 118.22 + 72.424\mathrm{X} + 4.6835\mathrm{X}^2 - 4.7788\mathrm{X}^3 - 8.1937\mathrm{X}^4 + 11.476\mathrm{X}^5 + 4.48\mathrm{X}^6 \quad (13)$$

where X is the reduced temperature X = $[T - (T_{\max} + T_{\min})/2]/[(T_{\max} - T_{\min})/2]$, T is the experimental temperature, thus, in the solid state (80–385 K), X = $[(T/\mathrm{K}) - 232.5]/152.5$, $T_{\max}$ is the upper limit (385 K) and $T_{\min}$ is the lower limit (80 K) in the above temperature region. The correlation coefficient of the fitting $R^2 = 0.9998$.

For the liquid phase over the temperature range 395–410 K:

$$C_{p,\mathrm{m}}/\mathrm{J}\cdot\mathrm{K}^{-1}\cdot\mathrm{mol}^{-1} = 322.1 + 0.7507\mathrm{X} \quad (14)$$

where X is the reduced temperature, X = $[(T/\mathrm{K}) - 402.5]/7.5$, T is the experimental temperature, 402.5 is obtained from polynomial $(T_{\max} + T_{\min})/2$, 7.5 is obtained from polynomial $(T_{\max} - T_{\min})/2$. $T_{\max}$ and $T_{\min}$ are the upper (410 K) and lower (395 K) limit temperatures, respectively. The correlation coefficient of the fitting $R^2 = 0.9985$.

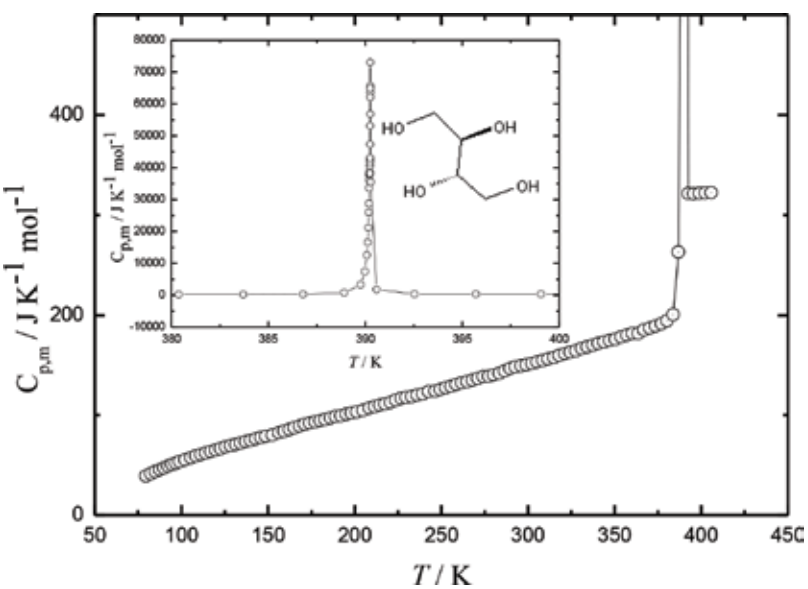

Figure 11. Experimental molar heat capacity of erythritol as a function of temperature.

6.2.2. The temperature, enthalpy, and entropy of solid-liquid phase transition

The molar enthalpies and entropies of the solid-liquid phase transition $\Delta f_{us}H_m$ and $\Delta f_{us}S_m$ of erythritol were derived according to the thermodynamic equations (see Section 3.2.2 in this chapter). The derived thermodynamic parameters were listed in Ref. [20].

6.2.3. Thermodynamic functions of erythritol

The thermodynamic functions of erythritol relative to the reference temperature 298.15 K were calculated in the temperature range 80–411 K with an interval of 5 K, using the polynomial equations of heat capacity (13), (14) and thermodynamic relationships (see Section 3.2.3. in this chapter).

The calculated thermodynamic functions, $H_T - H_{298.15}$ and $S_T - S_{298.15}$, are listed in Ref. [20].

6.2.4. The result of TG and DSC analysis

From the DSC curve in **Figure 12**, a sharply endothermic peak corresponding to melting process was observed, with the peak temperature of 397.33 K and the enthalpy of 34.89 ± 0.35 kJ·mol^{-1}, which are slightly lower than the values (390.254 K, 39.92 ± 0.20 kJ·mol^{-1}) observed from the adiabatic calorimetric measurements. The results were listed in Ref. [20], from which it can be seen that the thermodynamic parameters obtained from adiabatic calorimetry and DSC in the present research are in accordance with each other and slightly lower than those reported in literature [7].

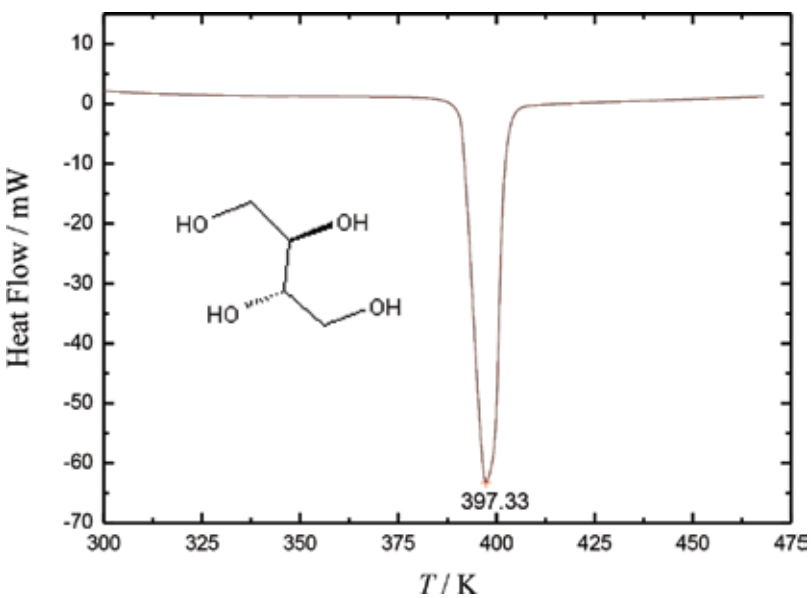

Figure 12. DSC curve of erythritol under high-purity nitrogen.

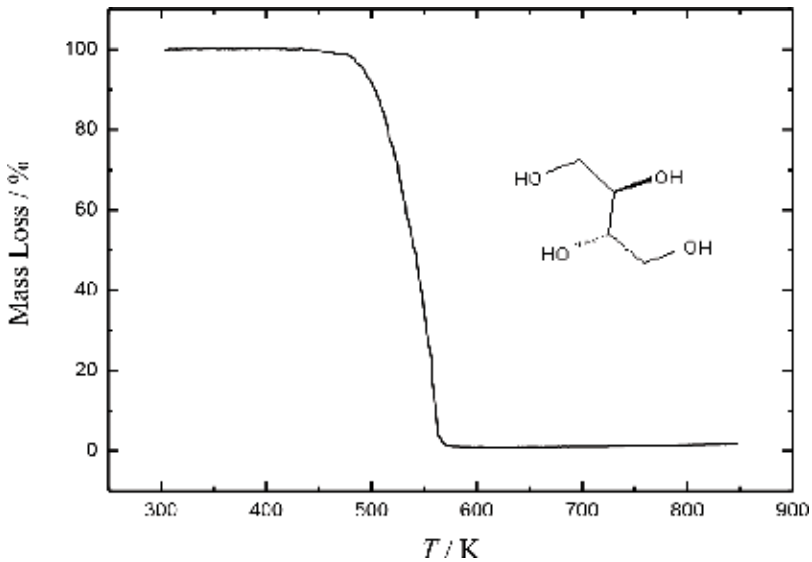

Figure 13. TG curve of erythritol under high-purity nitrogen.

From the TG-DTG curve in **Figure 13**, it can be seen that the mass loss of the sample was completed in a single step. The sample keeps thermostable below 450 K. It begins to lose weight at 476.75 K, reaches the maximum rate of weight loss at 557.44 K, and completely loses its weight when the temperature reaches 582.35 K.

7. Conclusion

In this chapter, the heat capacities of four kind of natural polyols, including xylitol, sorbitol, adonitol, and erythritol were measured in the temperature range from 80 to 400 K using a fully automated and high-precision adiabatic calorimeter constructed in our thermochemistry laboratory. The thermal stabilities of these polyos were also determined by thermal analysis techniques, differential scanning calorimeter (DSC), and thermogravimetric analyzer (TG). The heat capacity and thermodynamic property data presented in this chapter would provide a significant thermodynamic basis for understanding the thermal characteristics in both theory and practical designing of thermal energy storage units by using these polyols as PCMs. According to the above research results, the following conclusions can be drawn:

1. As the temperature of the polyols gradually increases, the solid-liquid phase change takes place, and the enthalpies of phase change are relatively large, hence, the polyols can be used as solid-liquid PCMs for thermal energy storage.

2. The phase change and thermostable temperature zone of the natural polyols covers 300 ~ 400 K, which is suitable for temperature control of human life and industrial production.

3. In the solid-liquid phase transition process, the thermodynamic properties of the natural polyols are stable, so their service life is long and convenient for practical application.

4. The natural polyols do not form plastic crystals, they are not volatile, are nontoxic, noncorrosive, so they can be used as a green and environment-friendly PCMs for thermal energy storage.

5. The key thermodynamic property data reported in this chapter for practical application of the four natural polyols as PCMs are finally summarized in **Table 1**.

Thermodynamic properties	Phase change temperature (K)	Enthalpy of phase change ($kJ \cdot mol^{-1}$)	Thermal stable temperature (<K)
Xylitol	369.04	33.26	450
Sorbitol	369.16	30.35	500
Adonitol	369.08	36.42	550
Erythritol	390.25	39.92	450

Table 1. Comparison of heat storage capacity of four natural polyols as solid-liquid phase change materials.

Acknowledgements

This work was financially supported by the National Natural Science Foundation of China under the grant NSFC No.21473198. Q. Shi would like to thank Hundred-Talent Program founded by Chinese Academy of Sciences.

Author details

Zhicheng Tan*, Quan Shi and Xin Liu

*Address all correspondence to: tzc@dicp.ac.cn

Thermochemistry Laboratory, Dalian Institute of Chemical Physics, Chinese Academy of Science, Dalian, China

References

[1] Lan X-Z. A study on gelatinization and microencapsulation of low-temperature phase change materials for energy storage. Dalian Institute of Chemical Physics, Chinese Academy of Sciences, Dalian, China, 2003

[2] Tong B. Preparation of polyols as phase change materials and studies on their themodynamic properties. Dalian Institute of Chemical Physics, Chinese Academy of Sciences, Dalian, China, 2008

[3] Tan ZC, Zhou LX, Chen SX, Li XY, Sun Y, Yin AX. A precision adiabatic calorimeter for measurement of heat capacities of aqueous solution of ethylene glycol. Chinese Science Bulletin. 1979;**24**:835-839

[4] Benson DK, Burrows RW, Webb JD. Solid state phase transitions in pentaerythritol and related polyhydric alcohols. Solar Energy Materials. 1986;**13**:133-152

[5] Zhang ZY, Yang ML. Heat capacities and phase transitions of 1,1,1-trihydroxymethylpropane and pentaerythritol over the superambient temperature range. Themochimica Acta. 1989;**156**: 157-161

[6] Zhang ZY, Yang ML. Heat capactiy and phase transition of 2-amino-2-methyl-1,3-propanediol from 280K to the melting point. Thermochimica Acta. 1990;**169**:263-226

[7] Barone G, Gatta GD. Enthalpies and entropies of sublimation, vaporization and fusion of nine polyhydric alcohols. Journal of Chemical Sociality Faraday Transaction. 1990;**86**(1):75-79

[8] Granzow B. Hydrogen bonding and phase transitions of a group of alcohols derived from 2, 2-dimethylpropane. Journal of Molecular Structure. 1996;**381**:127-131

[9] Takeda K, Yamamur O, Tsukushi I, Matsuo T, Suga H. Calorimetric study of ethylene glycol and 1,3-propanediol: Configurational entropy in supercooled polyalcohols. Journal of Molecular Structure. 1999;**479**:227-235

[10] Li L, Tan ZC, Meng SH, Song YJ. A thermochemical study of 1,10-decanediol. Thermochimica Acta. 1999;**342**:53-57

[11] Wang X, Lu ER, Lin WX, Liu T, Shi ZS, Tang RS, et al. Heat storage performance of the binary systems neopentyl glycol/pentaerythritol and neopentyl glycol/trihydroxy methyl-aminomethane as solid-solid phase change materials. Energy Conversion & Management. 2000;**41**:129-134

[12] Wang XW, Lu ER, Lin WX, Wang CZ. Micromechanism of heat storage in a binary system of two kinds of polyalcohols as a solid-solid phase change material. Energy Conversion & Management. 2000;**41**:135-144

[13] Feng HY, Xd L, He SM, Wu KZ, Zhang J. Studies on solid-solid phase transitions of polyols by infrared spectroscopy. Thermochimica Acta. 2000;**348**:175-179

[14] Talja RA, Roos YH. Phase and state transition effects on dielectric, mechanical, and thermal properties of polyols. Thermochimca Acta. 2001;**380**:109-121

[15] Romero CM, Páez M. Thermodynamic properties of aqueous alcohol and polyol solutions. Journal of Thermal Analysis and Calorimetry. 2002;**70**:263-267

[16] Tong B, Tan ZC, Lv XC, Sun LX, Xu F, Shi Q, et al. Low-temperature heat capacities and thermodynamic properties of 2, 2-dimethyl-1, 3-Propanediol. Journal of Thermal Analysis and Calorimetry. 2007;**90**:217-222

[17] Tong B, Tan ZC, Shi Q, Li YS, Wang SX. Thermodynamic investigation of several natural polyols (I). Heat capacities and thermodynamic properties of xylitol. Thermochimica Acta. 2007;**457**:20-26

[18] Tong B, Tan ZC, Shi Q, Li YS, Wang SX. Thermodynamic investigation of several natural polyols (II). Heat capacities and thermodynamic properties of sorbitol. Journal of Thermal Analysis and Calorimetry. 2008;**91**:463-469

[19] Tong B, Tan ZC, Wang SX. Low temperature heat capacities and thermodynamic properties of 2-methyl-2-Butanol. Chinese Journal of Chemistry. 2008;**26**:1561-1566

[20] Tong B, Tan ZC, Zhang JN, Wang SX. Thermodynamic investigation of several natural polyols (III). Heat capacities and thermodynamic properties of Erythritol. Journal of Thermal Analysis and Calorimetry. 2009;**95**(2):469-475

[21] Tong B, Yu Y, Tan ZC, Meng CG, Cuia LJ, Liu RB. Thermodynamic investigation of several natural polyols (IV):Heat capacities and thermodynamic properties of adonitol. Thermochimica Acta. 2010;**499**:117-122

[22] Tong B, Tan ZC, Liu RB, Meng CG, Nan ZJ. Thermodynamic investigation of polyhydroxy solid-solid phase change materials (I): Heat capacities and standard molar enthalpy of formation of 2-Amino-2-methyl-1,3-propanediol ($C_5H_{11}NO_2$). Energy Conversion and Management. 2010;**51**:1905-1910

[23] Tong B, Liu RB, Meng CG, Yu FY, Ji SH, Tan ZC. Heat capacities and nonisothermal thermal decomposition reaction kinetics of D-mannitol. Journal of Chemical and Engineering Data. 2010;**55**:119-124

[24] Jia R, Sun KY, Li RC, Zhang YY, Wang WX, Yin H, Fang DW, Shi Q, Tan ZC. Heat capacities of some sugar alcohols as phase change materials for thermal energy storage applications. Journal of Chemical Thermodynamics. 2017;**115**:233-248

[25] Sun KY, Kou Y, Li YS, Zheng H, Liu X, Tan ZC, Shi Q. Using silicagel industrial wastes to synthesize polyethylene glycol/silica-hydroxyl form-stable phase change materials for thermal energy storage applications. Solar Energy Materials and Solar Cells. 2018;**178**:139-145

[26] Tan ZC, Liu BP, Yan JB, Sun LX. A fully automated high precision adiabatic calorimeter workable between 80 and 400 K. Computers and Applied Chemistry. 2003;**20**:264-268

[27] Tan ZC, Shi Q, Liu BP, Zhang HT. A fully automated adiabatic calorimeter for heat capacity measurement between 80 and 400 K. Journal of Thermal Analysis and Calorimetry. 2008;**92**(2):367-374

[28] Donald GA. Thermodynamic properties of synthetic sapphire standard reference material 720 and the effect of temperature-scale difference on thermodynamic properties. Journal of Physical and Chemical Reference Data. 1993;**22**:1441-1452

Chapter 6

Graphene Aerogel-Directed Fabrication of Phase Change Composites

Guangyong Li, Xiaohua Zhang and Xuetong Zhang

Additional information is available at the end of the chapter

http://dx.doi.org/10.5772/intechopen.74616

Abstract

Although phase change materials have been extensively used for thermal energy storage, various shortcomings such as low thermal conductivity, leakage during work, and shortage of multiple driving ways greatly hinder their practical applications. Among the new materials that can overcome these problems, graphene aerogel has attracted special interest owing to its 3D conductive network and extraordinary capillary force. In this chapter, we review recent progress of graphene-aerogel-based phase change composites (PCCs) and provide a brief introduction on the following topics: 1) why graphene aerogels can be used for PCCs, 2) the sol-gel transition synthesis of graphene aerogels, 3) the fabrication of graphene-aerogel-based PCCs, and 4) their applications in thermal energy storage, electric-thermal conversion and storage, solar-thermal conversion and storage, and thermal buffer. Finally, we also discuss the limitation and future development of these graphene-based materials.

Keywords: phase change materials, aerogel, graphene, sol-gel, thermal energy

1. Introduction

Thermal energy storage technologies have played a broad and critical role in sustainable utilization of energy in heating and cooling apparatus, including vehicles and buildings, smart textiles with thermal comfort, electrochemical and electronic devices [1–3]. Phase change materials (PCMs) have been widely used in thermal energy storage technologies because they can absorb or release a great amount of energy as latent heat during the solid-solid or solid-liquid phase transitions over a narrow temperature range. In general, PCMs can be classified into organic (e.g., paraffin, fatty acids, and polyethylene oxide) and inorganic types (inorganic salts and their hydrates). The organic PCMs have attracted great attention in phase change

system as they exhibit high phase change enthalpy, wide melting temperature for convenient use, chemical stability and abundance in natural resources, besides the common properties of the inorganic ones. However, their practical applications are still hindered by various shortcomings of PCMs [4], such as the low thermal conductivity, leakage during melting process, and weak responsiveness to optical or electrical stimuli.

To resolve these disadvantages, scientists have tried to embed various PCMs into a lot of matrices, such as microcapsules and 3D porous materials (aerogel, foam, and sponge) with interconnected network [5–10]. The matrices can give the PCMs improved thermal conductivity, shape stability during melting process, and high absorption of sunlight or sufficient electrical conductivity for multiple driving ways. In principle, the ideal matrix should possess excellent thermal conductivity to improve the power capacity, extensive capillary force and high mechanical property to avoid leakage during working, lightweight framework to maintain high latent heat, and dark color and high electrical conductivity to store thermal energy via multi-driven ways (sunlight absorbing or Joule heating).

Graphene, a novel nanomaterial with two-dimensional (2D) planar crystal consisting of a single carbon atom layer, has many extraordinary properties including superior flexibility, strong mechanical strength, and excellent electrical and thermal conductivities [11]. However, graphene sheets usually tend to irreversibly aggregate or even re-stack back to graphite due to their intrinsic 2D conjugated structure, making it difficult to efficiently exploit the inherent properties of graphene [12]. There are several ways to resolve such problem by designing porous assemblies of graphene with a 3D interconnected network, namely, assembling into aerogel microspheres by a micro-droplet technology, into aerogel fiber with the help of spinning technology, and even into aerogel film and monolith. These different forms of graphene aerogel have the following common characters: low mass density, high porosity, robust mechanical performance, blackbody-like absorptive performance, electrically and thermally conducting, and extraordinary capillarity [12–14]. Therefore, multifunctional phase change composites (PCCs) can be developed based on these graphene aerogels, and are expected to exhibit superior performances including excellent conductivity, high latent heat, multiple driving ways (thermal, electrical, and optical), and no leakage for melt PCMs.

This chapter reviews recent and rapid progress on graphene-aerogel-based PCCs and discusses their future development. First, the fabrication of graphene aerogels based on sol-gel transition is described in Section 2. Then, Section 3 discusses in detail the synthesis of graphene-aerogel-based PCCs including microspheres, fiber, film, and monolith. Finally, the typical applications of PCCs are introduced in Section 4. This chapter may inspire many new explorations surrounding the PCM-based thermal energy storage.

2. Fabrication of graphene aerogel

Graphene aerogels can be prepared via both solution assembly and chemical vapor deposition (CVD) growth. The solution assembly technology is based on a sol-gel reduction process of graphene oxide (GO) solution and a subsequent specific drying [12, 14]. GO sheets are rich in

oxygen-containing functional groups that allow excellent dispersibility in water and polar organic solvent, promising the possibility to operate graphene sheets into aerogels. The CVD growth technology is usually performed on specific template (e.g., Ni foam or SiO_2 aerogel) during high temperature atmosphere that contains carbon source (e.g., CH_4 and ethanol), and the aerogel is obtained after removing the template [15, 16].

The solution assembly has become the most popular method to prepare graphene aerogels due to its cost-effective progress, high yield from cheap graphite, amenability to operation, and efficient utilization of the inherent properties of graphene [12]. The solution fabrication mainly involves the synthesis of graphene hydrogel, the aerogel precursor, and the subsequent drying process.

2.1. Synthesis of graphene hydrogel

The graphene hydrogel can be synthesized via a sol-gel transition of GO solution, together with a reduction process. After the reduction, the oxygen-containing functional groups on GO sheets can be removed, resulting in the recovery of strong π-π interaction and a transition from hydrophilicity to hydrophobicity [12]. It can also promote the gelation process to form a uniform graphene hydrogel, based on the partial overlapping and π-π stacking between the reduced GO (rGO) sheets [12]. Such sol-gel transition can be realized via a variety of reduced routes, such as chemical reduction [17], hydrothermal reduction [18], and electrochemical reduction [19].

Chemical reduction is a versatile and mild method, and can be performed in acidic or alkaline media by using different reducing agents, such as L-ascorbic acid (L-AA), HI, $NaHSO_3$, NaI/oxalic acid, dopamine, ethane diamine, and even metals (Zn) [14]. Notably, the agents used here should be mild and green, and can promote the formation of uniform graphene hydrogel without generating any gas. For example, by introducing L-AA into GO solution, mixing them uniformly, and then heating the mixture for a period of time without stirring, a uniform graphene hydrogel was obtained (**Figure 1a-b**) [17]. To understand the sol-gel transition, various factors like GO concentration, GO/L-AA mass ratio, temperature, time, and pH of the sol-gel reaction were investigated systematically [20]. For the GO/L-AA mixed solution, the GO concentration and L-AA/GO mass ratio are two key factors; the optimal GO concentration was found to be 1.0–6.0 mg/mL and the mass ratio could be in a very wide range 1:2–832:1. When the amount of GO was too small (<1.0 mg/mL) or L-AA was insufficient (L-AA/GO <1:2), it was difficult to induce the partial stacking and overlapping; on the contrary (GO >6 mg/mL or L-AA/GO >832:1), the uniform dispersion of GO or L-AA became difficult. Other parameters like a pH value of 7.0-3.0, a high temperature of 25–80°C, and a long aging time were also found to benefit the gelation rate and the hydrogel quality. Besides L-AA, other reducing agents have also been investigated. By using a similar sol-gel treatment, ethane diamine was dissolved in a GO solution to reduce the GO during the formation of graphene hydrogel, after being aged in 95°C for 6 h [21]. Such hydrogel was electrically conducting and mechanically robust, and exhibited a uniform gel network, being able to serve as an ideal precursor for aerogel.

However, under a low GO concentration, such as the aforementioned optimal 1.0–6.0 mg/mL, the obtained graphene aerogel usually exhibited a disordered porous network. For a better performance, is it possible to assemble GO sheets to an anisotropic graphene hydrogel with a

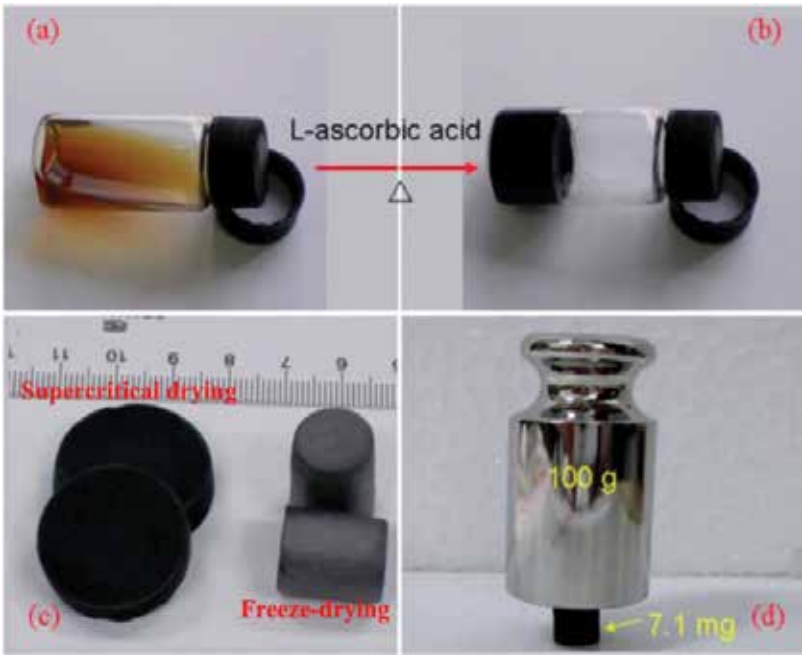

Figure 1. Digital photos of the aqueous suspension of graphene oxide (a), the graphene hydrogel in a vial (b), the graphene aerogels obtained by supercritical CO_2 drying and freeze-drying (c), and a graphene aerogel supporting a counterpoise (d) [17].

certain alignment or orientation of the pore or graphene sheets? As a successful demonstration, under a high-speed centrifugation, a highly concentrated GO dispersion exhibited a novel fluid crystal phase, namely, a GO liquid crystal (GO-LC). The GO sheets tended to orient parallel with each other, resulting in the ordered arrangement of GO sheets [22, 23]. However, the high viscosity of GO-LC brought new problems toward the uniform sol-gel transition, making the application of the conventional reduction routes no longer suitable for the preparation of graphene hydrogel.

Very recently, a novel sol-gel strategy was proposed to synthesize the anisotropic graphene hydrogel, by an in situ gelation of GO-LC using the gaseous hydrogen chloride (HCl (g)), and a subsequent chemical reduction as well (**Figure 2**) [24]. When a GO-LC is placed in HCl atmosphere, the HCl molecule can dissolve and diffuse slowly into the GO-LC, together with an immediate ionization, which promised the "in situ freezing" of dynamic hydrogen-bonding network and resulted in the generation of GO-LC hydrogel (**Figure 2**). Interestingly, the HCl treatment can also induce a typical colorful texture between crossed polarizers, due to the directional arrangement of GO sheets. Then, the GO-LC hydrogel can be immersed into HI (aq) to obtain an anisotropic graphene hydrogel with different macro-sizes and shapes. As no stirring and mixing operations are involved, the original arrangement of GO sheets can be well maintained in the final graphene hydrogel.

Importantly, the shape of graphene hydrogel can simply be controlled by changing the reactor or introducing a certain confinement effect. From the former way, graphene hydrogels with various shapes including cylinder, sphere, and rectangular solid have been reported. For the

http://dx.doi.org/10.5772/intechopen.74616

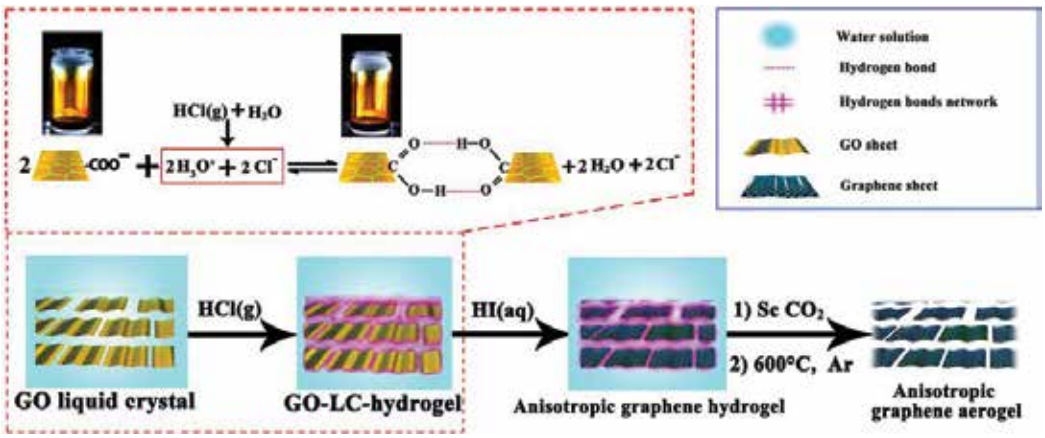

Figure 2. Schematic description of the synthesis of anisotropic graphene aerogels, derived from liquid crystals under the assistance of the solid hydrogen-bonded network, based on a vapor diffusion and sol-gel process [24].

latter, the micro-droplet, filming, and spinning techniques have been used to obtain the graphene hydrogel microsphere, film, and fibers.

2.2. Drying process

The obtained graphene hydrogel can be dried via some specific drying treatment to form a graphene aerogel. During the normal drying method, the graphene hydrogel undergoes a direct liquid-gas transition, where the remarkable change in capillary force causes the shrink and collapse of the porous network [25]. Therefore, in order to maintain the porous network, supercritical fluid drying or freeze-drying is suggested to replace the liquid solvent of graphene hydrogel with air, rather than by the direct liquid-gas transition [17, 25].

The supercritical fluid drying is realized in a supercritical state where the temperature and pressure are beyond the critical point. Supercritical CO_2 (Sc CO_2) has become the most widely used method due to its low critical temperature (31.1°C), no risk of combustion and toxic gas, and a moderate critical pressure (7.38 MPa). By the Sc CO_2 drying, graphene hydrogel can be converted into graphene aerogel successfully [17, 24]: 1) the liquid component of the original graphene hydrogel is replaced by an organic solvent (ethanol, acetone, methanol, etc.); 2) the obtained organogel is placed in a pressure vessel and then soaked in a flowing Sc CO_2 for a period time, until all the solvent in the porous network was replaced by Sc CO_2; and 3) a graphene aerogel is finally obtained after recovering the pressure vessel to ambient pressure.

For example, as shown in **Figure 1c**, a graphene aerogel with Sc CO_2 drying was obtained, which exhibited a certain darkness, high porosity, high specific surface area (512 m^2/g), large pore volume (2.48 cm^3/g), high electrical conductivity (~10^2 S/m), and high mechanical property; it could support at least 14,000 times its own weight (**Figure 1d**) [17].

The freeze-drying mainly involves the freezing and sublimate processes, and this drying can induce a solid-gas transition [25]. To prepare a graphene aerogel, a graphene hydrogel that contains plenty of water is first frozen at a low temperature (liquid N_2 or freezer), and then the

ice inside the pore starts to sublimate directly under vacuum, with the pore being filled by air [17, 26–28]. During the freeze-drying process, the growth of ice crystal usually causes reconstruction of the original network of hydrogel, together with an aggregation of the mesopores into a macropore. Then the resulting graphene aerogel usually shows a poor mechanical strength, high brittleness, low specific surface area, and little mesopore volume. As shown in **Figure 1c**, the graphene aerogel by freeze-drying showed a metal luster, but it could only support 3300 times its own weight [17]. Based on a N_2 adsorption/desorption test, the pore volume was 0.04 cm^3/g in the size range of 1.5–55 nm, which was much lower than that of the graphene aerogel by Sc CO_2 drying (2.48 cm^3/g), corresponding to the disappearance of mesopores.

3. The fabrication of graphene-aerogel-based PCCs

According to the different macroscopic architectures of graphene aerogels, the graphene-aerogel-based PCCs can be developed in forms of 0D microspheres, 1D fibers, 2D films, and 3D monoliths. The two widely used strategies for the fabrication of aerogel-based PCCs (e.g., carbon aerogel, carbon nanotube sponge, carbon nanotube array, graphene aerogel, and other aerogel matrices) are the melted filling and solvent-assisted filling [7–9, 24].

Above the melting point, the conventional PCMs will become liquid state. The melted PCMs can be infiltrated directly into the porous network of aerogel owing to aerogel's extraordinary capillary force, similar to the simple process of "sponge absorbing water". Thus, graphene aerogel could direct the fabrication of PCCs [24, 29]: immerse a graphene aerogel into a melted PCM, allow the pore space of aerogel be filled by the PCM, promise the melted PCM to be cooled inside the aerogel network, and then by removing the residue paraffin on the surface of composite, the relevant graphene aerogel-directed PCC could be obtained.

The solvent-assisted filling strategy can be performed by introducing a PCM solution into the internal space of aerogel. This method could avoid the limitation of temperature and high viscosity of the melted PCM [7]. First, a graphene aerogel is immersed into a PCM solution such as polyethylene glycol (PEG)/water, wax/CH_2Cl_2, stearic acid/C_2H_5OH. Then the PCM solution will flow into the porous network of aerogel, and then stay in the pores or get absorbed on the walls. After removing the solvent via natural volatilization, a PCC can be obtained. Notice that the densification and solidification effects from the solvent evaporation process may bring many fascinating properties.

Both the melted filling and solvent-assisted filling are based on the similar driving force—the capillary force of aerogel. There are also slight differences between these two methods, and they have their own scope of application. In the following sections, more detailed introduction is provided according to the shapes of microspheres, fibers, films, and monoliths.

3.1. 0D composite microsphere

To prepare graphene-aerogel-based PCC microspheres, the mono-dispersed graphene aerogel microspheres (GAMs) with 3D interconnected porous network should be produced first.

Unfortunately, the traditional strategies, including injection prilling, emulsion polymerization, and spray granulation, are not suitable for the fabrication of mono-dispersed GAMs [30–32], because the gelation should be realized in microdroplets and a long aging process is necessary.

Herein, based on the original sol-gel principle, a novel and programmable strategy has been developed, namely, an ink jetting-liquid marbling-supercritical fluid drying coupling technique, to produce mono-dispersed GAMs (**Figure 3a**) [33]. Typically, the valve ink jetting was used to synthesis the GO/L-AA droplets because it had a much wider size window and could precisely control the droplet size. The obtained mixed microdroplets were then dropped into a specific container fully filled with hydrophobic nanoparticles to form liquid marble. The liquid marbling technology could keep individual droplets separated from each other and maintain spherical structure without amalgamation. Once the injection was completed, the container

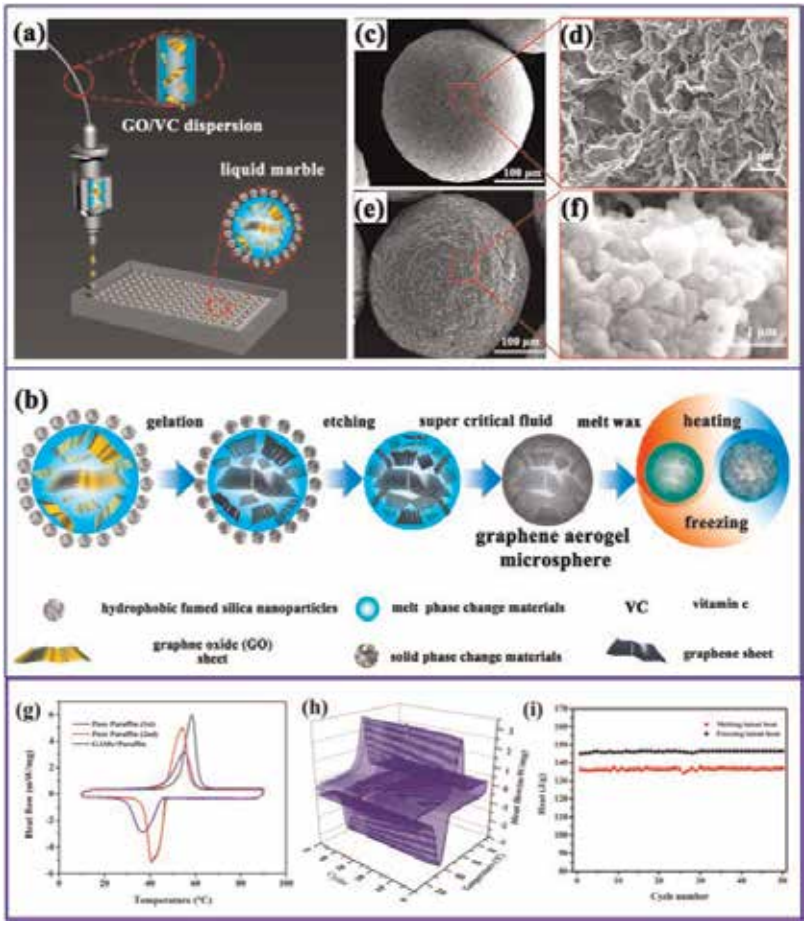

Figure 3. Schematic and results of the "ink jetting−liquid marbling−supercritical drying" coupling approach to make graphene aerogel microspheres and phase change microspheres [33]. (a) the ink jetting of sol droplet precursor. (b) the preparation of GAMs and phase change microspheres. (c-f) SEM images of a GAM (c,d) and a PCC microsphere (e,f). (g) Cyclic DSC curves of the paraffin and GAM-based PCC microspheres. (h,i) DSC curves and the corresponding latent heats of the PCC microspheres tested in 50 cycles.

was sealed and a sol-gel transition was triggered. Thus, GAMs with 3D interconnected graphene porous network could be fabricated by supercritical drying (**Figure 3c-d**). By adjusting the size of microdroplets, the size of graphene hydrogel microspheres could be efficiently controlled. Based on a statistical analysis on the size distribution of graphene hydrogel microspheres, the variation coefficients were 6.4, 4.9, and 5.6%, for the graphene hydrogel microspheres with an average size of 170, 200, and 230 μm, respectively, indicating that the ink jetting and liquid marbling techniques showed a superior advantage to produce uniform-sized GAMs.

By the melted filling, the PCM could be introduced into the inner pore spaces of GAMs, and the relevant graphene aerogel-directed PCC microspheres were obtained [33]. These microspheres exhibited good sphericity, and owing to the continuous conducting network of graphene aerogel and phase change ability of paraffin, they also exhibited a high latent heat (136 J/g, **Figure 3g**), excellent cyclic stability (**Figure 3h** and **i**). Furthermore, the microspheres (diameter ~700 μm) could respond to a weak heat (as low as 0.027 J) very sensitively, together with fascinating electrical properties, remarkable mutation of electrical resistance; the resistance was about 1370 Ω for the solid and 4850 Ω after being melted.

3.2. 1D composite fiber

Phase change fiber, also named as smart thermoregulating fiber, can buffer the environmental temperature variation by absorbing/releasing thermal energy. So far, the preparation of PCC fiber is mainly based on composite spinning, including wet-spinning, melt-spinning, and electrospinning [34–36]. For example, pure PCM or microencapsulated PCM can be mixed into polymer solution or its melt, which can be later spun into fibers [37]. However, the obtained fibers did not show a high enthalpy and their repeatability was quite low. It is still of strong requirement to develop new-type PCC fibers, via a novel and facile approach.

Graphene aerogel fiber (GAF) consisting of aligned graphene porous network can provide a successful template toward such development. The GAF can be prepared by both freeze-dry spinning and wet-spinning based on GO-LC. Such aerogel fibers usually contain interconnected porous network of aligned graphene sheets, and thus also exhibit high porosity, large specific surface area, excellent conductivity, and high flexibility. For example, a GAF with a unique "porous core-dense shell" structure was produced by a freeze-dry spinning, a combination of spinning and ice-templating strategy [38]. The obtained GAF showed a high electrical conductivity of 2.0×10^3 S/m, high mechanical strength (11.1 MPa), and large specific surface area (~884 m^2/g). At the same time, another GAF with aligned porous network was obtained by spinning GO-LC into specific coagulation bath which contained a reducing agent, such as HCl/L-AA (aq), HCl/HI (aq), acetone/HI (aq), $CaCl_2$/HI (aq), aniline hydrochloride/HI, followed by an aging process and specific drying. Such aerogel fiber exhibited a high mechanical strength (up to 18.1 MPa), high specific surface area (~548 m^2/g) and a large pore volume (~2.28 cm^3/g). In a different way, by injecting a GO/L-AA or GO/HI mixed solution into a micro-tube, after aging for a period of time under water bath and a following supercritical drying or freeze-drying, GAFs with excellent electrical conductivity and high flexibility property can be obtained [39].

Based on the obtained aerogel fiber, the aerogel-directed PCC fibers with variable phase change enthalpy and other thermal properties can be fabricated, by a solvent-assisted filling. By carefully adjusting the PCM materials and filling process (concentration, temperature, aging time, etc.), the mechanical, electrical, and thermal properties were tunable. For example, after introducing PEG-4000 (average molecular weight 4000), the obtained graphene/PEG PCC fiber exhibited a tunable phase change enthalpy of 28–116 J/g, depending on the PEG fraction, at a constant melting point of 54°C of the pure PEG-4000, see **Figure 4b**. The phase change enthalpy and melting point can also be efficiently adjusted in a wide temperature range by using different PCMs. For example, by using n-eicosane, the melting point could be just 36°C, and the enthalpy was as high as 186 J/g (**Figure 4c**).

3.3. 2D composite film

As compared to the 0D and 1D PCCs, a planar phase change film could provide a larger thermal exchange interface for thermal management in portable electronic devices. By combining the conventional filming technique [40–42], such as wet-spinning and blade-coating, with sol-gel transition and specific drying processes, graphene aerogel films with interconnected porous network can be produced.

Typically, GO-LC was spun via a wide spinning channel into a coagulation bath containing reducing agent (e.g., HCl/HI (aq), $CaCl_2$/HI (aq)) [41]. By such treatment, the fluid GO-LC would convert to a gel film, which was then being aged for 12 h. After a supercritical drying or

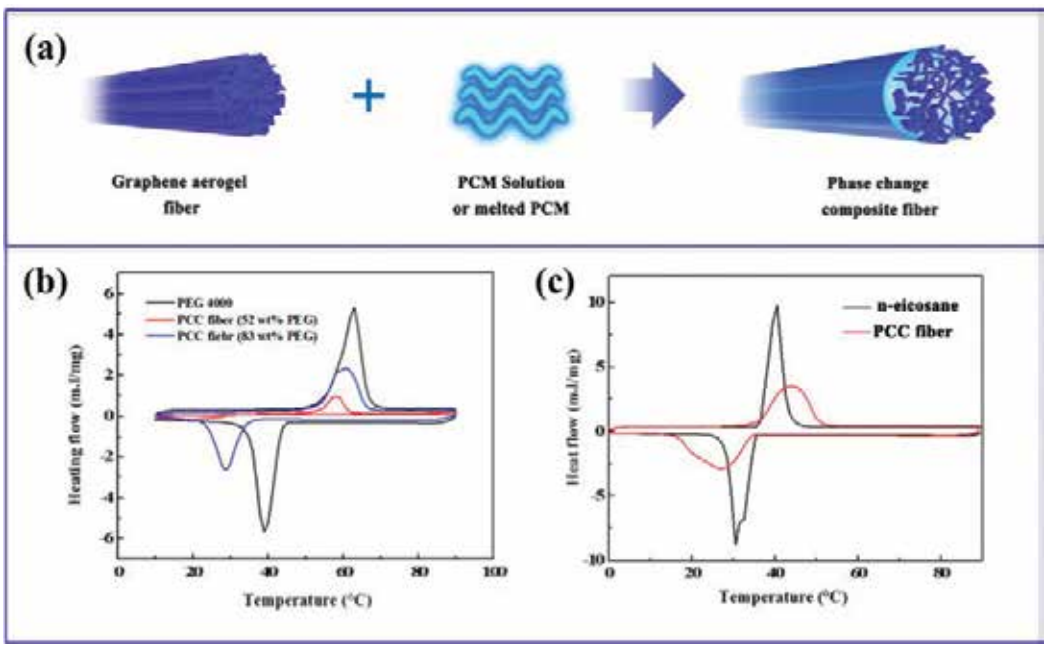

Figure 4. Aerogel-directed fabrication of graphene-aerogel-based PCC fiber. (a) Schematic description of the fabrication. (b,c) DSC curves of the PCC fibers, and for a comparison, the DSC result of PEG4000, and n-eicosane are plotted.

freeze-drying, a continuous graphene aerogel film was obtained. In another method, a high concentration GO dispersion or GO hydrogel was spread onto a glass substrate and a uniform GO hydrogel film could be obtained [42]. To reduce the GO, such hydrogel film was immersed into HI solution to obtain a flexible and free-standing graphene aerogel film by a supercritical drying process.

Based on the melted filling or solvent-assisted filling, the PCMs could be introduced for fabricating flexible and free-standing PCC films (**Figure 5**). For example, by immersing a graphene aerogel film into melted n-eicosane for about 3 h, a flexible composite film with a high latent heat (161 J/g) and low melting point (about 36°C) was obtained. As shown in **Figure 5b**, the PCC film exhibited a similar phase change behavior to pure n-eicosane.

3.4. 3D composite monolith

PCC monolith is the most widely used form for thermal energy storage due to their intrinsic bulk energy density. For a good heat transfer through a bulk PCC, the continuous and thermal conductive network is necessary. By considering its 3D porous network and high ability to conduct heat and current, graphene aerogel can serve as an important template to develop PCC monoliths.

The graphene-based PCC monoliths have been synthesized by melted filling. By immersing a bulk graphene aerogel into a melted PCM with the aid of vacuum, the inner pore spaces of aerogel can be fully filled by the PCM molecules. After a following cooling treatment, a PCC monolith can be obtained. For example, an anisotropic composite monolith was reported based on a composition of paraffin with a graphene aerogel with aligned pore structure, as shown in **Figure 6** [24]. Such PCC monolith contained a high paraffin loading up to 93.6 wt% with an enthalpy of 193.7 J/g. This special alignment of graphene network also induced a high anisotropy of the thermal conductivity, along the graphene sheet, the thermal conductivity could reach to 2.99 W/mK, about 15-fold higher than that of pure paraffin, higher than that of carbon nanotube array/n-eicosane composite; in other direction, the thermal conductivity exhibited a lower value of 1.2 W/mK.

A different method of hydrothermal reduction was also used to synthesize PCC monoliths [43]. To do so, a GO solution was mixed with a paraffin/cyclohexane solution, under a violent

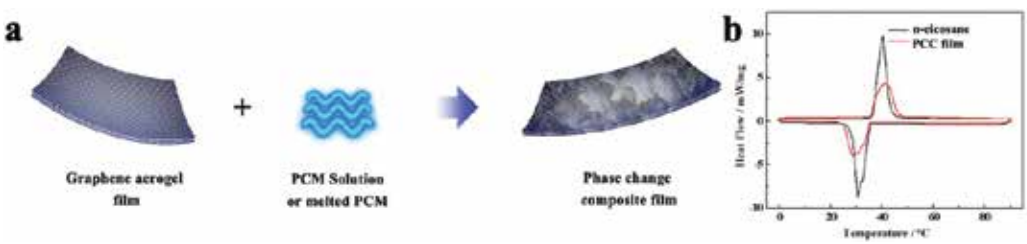

Figure 5. The preparation and thermal property of graphene-aerogel-based PCC film. (a) Schematic of preparation. (b) DSC curves of PCC film and n-eicosane.

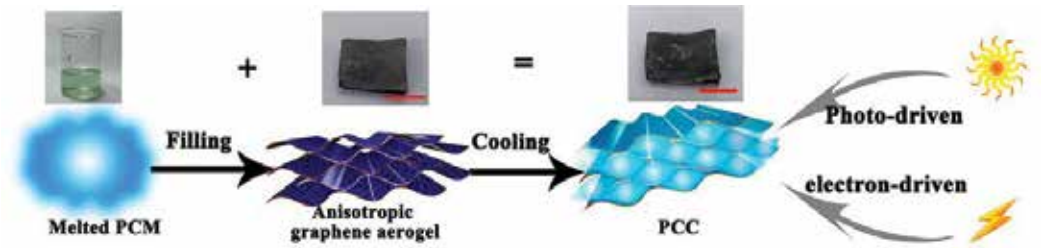

Figure 6. Illustration of the fabrication process in which the melting paraffin fills in the anisotropic graphene aerogel to make a composite that can be driven either electrically or optically for heat storage [24].

shaking to make the mixture (emulsion) homogeneous. Then, by a high temperature-induced reduction under a hydrothermal condition, and a following freeze-drying process, a PCC with encapsulated structure and continuous graphene network was obtained. By adjusting the concentration of the paraffin solution, a high PCM loading could be up to 97 wt%. Under such high loading, a good shape stability was still maintained as reflected by the zero PCM leakage, because the paraffin was encapsulated into the closed pore shell of graphene aerogel, to form micrometer-scaled droplets. Unfortunately, the thermal conductivity of such PCC monolith was just 0.274 W/mK, just comparable to that of the pure PCM (0.207 W/mK) [43].

4. Applications of graphene-aerogel-based PCCs

An intrinsic phase transition and high latent heat of PCMs, and their excellent physicochemical properties, would allow these graphene-aerogel-based PCCs to be applied in many fields with extraordinary performances.

4.1. Thermal energy storage

Among the various applications, thermal energy storage is the most fundamental application. It requires a superior thermal performance of PCM, including high thermal conductivity, high latent heat, excellent thermal cycling stability, and no leakage during work [24]. So far, graphene-aerogel-based PCCs have shown many advantages in thermal energy storage owing to the synergistic effect between graphene network and PCM.

Thermal conductivity is the most important property as it determines severely the power capacity of PCMs. Owing to the graphene network, the conductivity of graphene-aerogel-based PCCs were all much higher than that of pure PCMs. For example, based on a CVD-based graphene foam, the conductivity of the graphene/paraffin PCCs was up to 3.61 W/mK, 18 times higher than that of paraffin (0.2 W/mK) [3]. The similar enhancement was also observed for a rGO/octadecanoic acid PCC (from 0.18 W/mK for the pure octadecanoic acid to 2.6 W/mK) [44]. By using an anisotropic graphene aerogel, there was also an anisotropy in thermal conductivity (**Figure 7a**) [24]: the in-plane thermal conductivity was up to 2.99 W/mK,

while along the perpendicular direction it was just 1.2 W/mK (**Figure 7b**). Such anisotropy could provide a chance for rapidly storing heat along the parallel direction, and slowly releasing the heat along the other direction, making the heat usage more efficiently.

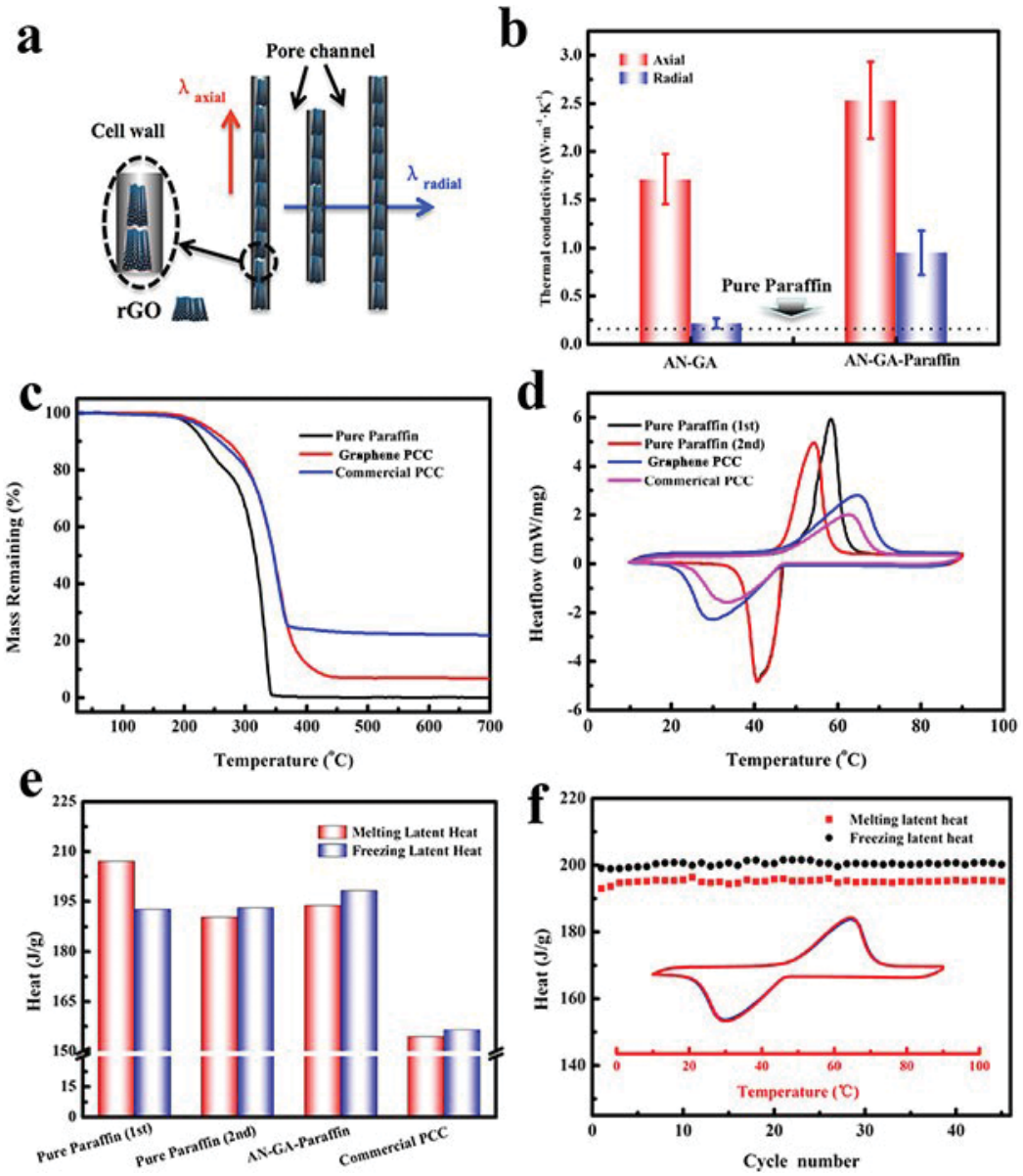

Figure 7. Thermal properties of an anisotropic graphene-based PCC monolith. (a) Schematic illustration of anisotropic heat transfer. (b) Thermal conductivities of the anisotropic graphene aerogel and the relevant PCC. (c,d) TGA and DSC curves of the pure paraffin, the commercial composite and the anisotropic graphene aerogel/paraffin PCC. (e) the measured latent heats obtained from (d). (f) Cyclic behaviors of the latent heat of the PCC during 45 melting-freezing cycles. The inset shows the 45th DSC curve which is fully identical to the first one in (d) [24].

Phase change enthalpy is another important characteristic, as it corresponds to the energy density. Although the introduction of graphene aerogel might affect the enthalpy of PCM slightly, the enthalpy of the overall PCC could be as high as the pure PCM. On the other hand, the presence of graphene could also benefit the crystallization of PCM, as a remedy to the enthalpy loss. Therefore, the full potential of PCM could still be realized in the PCC. For example, for a PCC monolith at a paraffin loading of 94 wt% (**Figure 7c**), the enthalpy was measured to be 193 J/g (**Figure 7d-e**), just ~6 wt% smaller than that of pristine paraffin (208 J/g). Nevertheless, such value was slightly higher than the secondary crystallization of pure paraffin (190.2 J/g) [24]. Furthermore, the porous network of graphene aerogel could promise the PCC to possess an excellent thermal stability between cyclic heating and cooling, as confirmed by the cyclic DSC curves (**Figure 7f**), and this excellent thermal stability also be found in other forms of PCC (0D, 1D, and 2D), as shown in **Figures 3–5** [26].

4.2. Electric-thermal conversion and storage

Electric-thermal conversion and storage based on PCM technique is important for effective utilization of power from off-peak electricity and renewable energy sources (e.g., wind and solar) [45]. As the basic property for electric-thermal conversion, high electrical conductivity of PCM is required. Unfortunately, the conventional PCMs are usually not an electrical conductor, and thus not available for electric-thermal conversion. For graphene-aerogel-based PCCs, the graphene network not only improves the thermal conductivity, but also exhibits many advantages in the electrical performances. As a result, when a current is passing thorough a PCC, the electric-thermal effect can be triggered by the graphene porous network, and the converted energy will be absorbed and stored by the PCM in the PCC [24].

Figure 8a shows the setup to evaluate the electro-thermal conversion and energy storage: a cylinder PCC monolith was connected into a DC circuit, and then the temperature evolution of PCC was recorded by a data collection system [24]. Under a constant voltage of 1.5 V, the PCC temperature increased rapidly during the first 45 s, and then reached a plateau until ~190 s, corresponding to the melting of paraffin (**Figure 8b**). After the full melting, the temperature started to increase again and much more rapidly. When the voltage was turned off, the

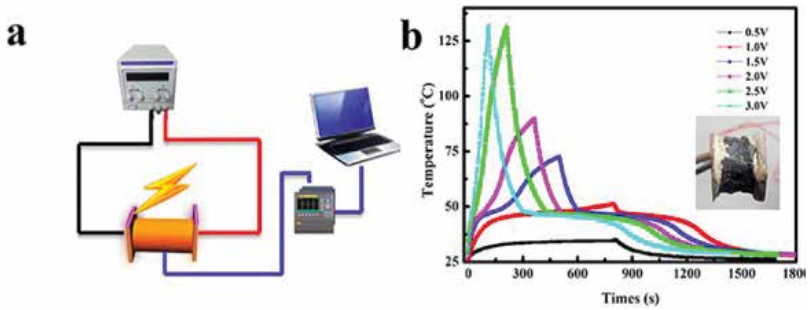

Figure 8. (a) Schematic illustration of the electro-driven phase change composite device circuit. (b) the temperature-time relationship of AN-GA-paraffin under different voltages [24].

temperature declined immediately to the freezing point (about 48°C) of paraffin, and another plateau was formed, corresponding to the solidification of paraffin. After the solidification stopped, the temperature would decrease again to room temperature. Via the temperature curves under different voltages, a critical voltage for a complete phase change was found to be about 1.0 V, which was a quiet low threshold compared to carbon aerogel (15 V) [8] and carbon nanotube sponges (1.5 V) [7].

4.3. Solar-thermal conversion and storage

Solar-thermal energy conversion and storage were essential for harvesting and utilizing of abundant solar energy. Both graphene aerogel and its directed PCC exhibited black appearance and high thermal conductivity, promising the application in solar energy.

To characterize the ability to convert solar energy [24], the graphene-aerogel-based PCC was placed under a solar simulator, by a tungsten-halogen lamp (**Figure 9a**). Without infiltrating any PCM into the graphene aerogel, the temperature of aerogel could increase up to 40–75°C under different light intensities, indicating that the graphene was a nice photo absorber (**Figure 9b**). For the graphene-aerogel-based PCC, due to the phase change, temperature plateaus (around 48°C) were observed during the solar-induced heating and cooling processes (**Figure 9c**), corresponding to an efficient energy storage. By dividing the stored thermal energy (from the product of enthalpy and PCC mass) by the irradiating energy overall received during the working time for the plateau, the conversion-storage efficient could reach to 77% (1.0 sun).

4.4. Thermal buffer

Graphene-aerogel-based PCC microspheres could serve as thermal buffer in electronic devices, as besides the ability to store the energy by Joule heating, they have also shown a fascinating electrical property.

To show such effect, a single graphene-based PCC microsphere was connected to a DC power by Cu wires (**Figure 10a**) [33]. Upon increasing the voltage, the current passing through the microsphere increased linearly until a critical point, where the Joule heating could have increased the temperature up to the melting temperature of PCM. Due to the PCM melting,

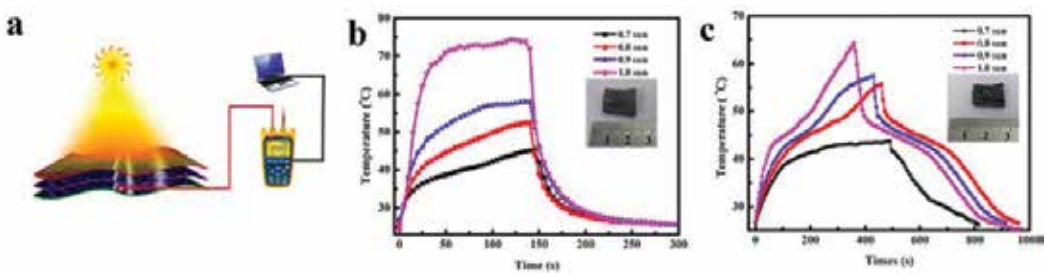

Figure 9. (a) Schematic of the characterization of solar-thermal conversion. (b,c) Temperature-time relationship under simulated sunlight (AM 1.5) at intensities of 0.7 sun, 0.8 sun, 0.9 sun, and 1.0 sun, for the anisotropic graphene aerogel and the corresponding PPC, respectively [24].

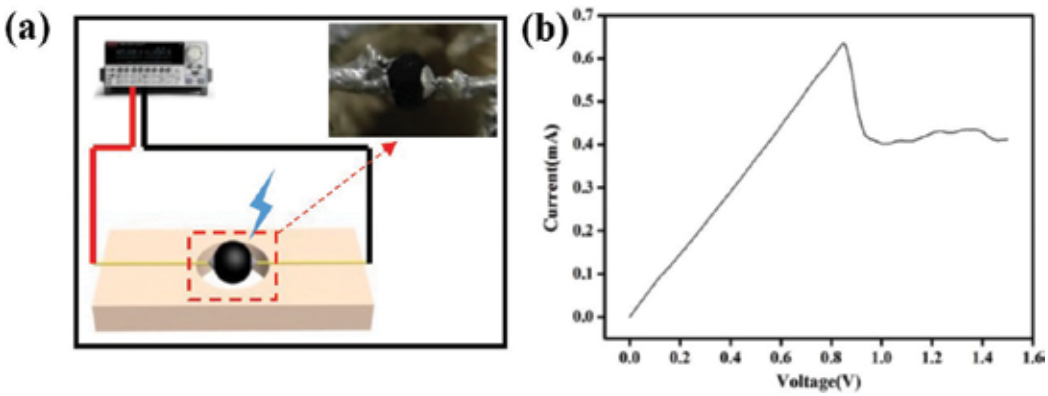

Figure 10. (a) Illustration of the testing process of thermal buffer, (b) current-voltage curve of a single graphene-aerogel-based PCC microsphere [33].

the resistance of the PCC microsphere increased very rapidly, as reflected by the current drop shown in **Figure 10b**. With further increasing the voltage, more PCMs melted, with the current suppressed at the finite value. Clearly, such effect of thermal buffer can effectively protect the circuit upon the overloading of voltage.

5. Conclusion and outlook

We have reviewed recent progresses of graphene-aerogel-based PCCs, in different forms with different dimensions, introduced in detail the sol-gel-based fabrication methods, and demonstrated their potential applications.

Besides these successful achievements, there are still many problems and challenges. For example, it is still easy to cause the reopening of the porous network of graphene under the external strike, leading to the leakage during the service. A higher thermal conductivity is still of strong request for high-performance applications, especially for the directional thermal conductivities. Furthermore, besides the thermal performance, more focus should be paid to the electrical and mechanical properties of PCC. Based on the multifunctionalities of graphene assemblies, smart PCCs are expected to respond to magnetic, heat, moisture, and abrasion. Furthermore, for the stored thermal energy, it is also important to convert it into electrical or mechanical energies by developing PCM-based actuators.

Acknowledgements

This work was financially supported by the National Natural Science Foundation of China (51572285, 21373024), the National Key Research and Development Program of China (2016YFA0203301) and the Natural Science Foundation of Jiangsu Province (BK20170428).

Author details

Guangyong Li[1,2], Xiaohua Zhang[1] and Xuetong Zhang[1]*

*Address all correspondence to: xtzhang2013@sinano.ac.cn

1 Suzhou Institute of Nano-Tech and Nano-Bionics, Chinese Academy of Sciences, Suzhou, P. R. China

2 School of Materials Science and Engineering, Beijing Institute of Technology, Beijing, P. R. China

References

[1] Liu C, Li F, Ma L-P, Cheng H-M. Advanced materials for energy storage. Advanced Materials. 2010;**22**:E28-E62. DOI: 10.1002/adma.200903328

[2] Pielichowska K, Pielichowski K. Phase change materials for thermal energy storage. Progress in Materials Science. 2014;**65**:67-123. DOI: 10.1016/j.pmatsci.2014.03.005

[3] Ji H, Sellan DP, Pettes MT, Kong X, Ji J, Shi L, Ruoff RS. Enhanced thermal conductivity of phase change materials with ultrathin-graphite foams for thermal energy storage. Energy & Environment Science. 2014;**7**:1185-1192. DOI: 10.1039/c3ee42573h

[4] Farid MM, Khudhair AM, Razack SAK, Al-Hallaj S. A review on phase change energy storage: Materials and applications. Energy Conversion and Management. 2004;**45**:1597-1615. DOI: 10.1016/j.enconman.2003.09.015

[5] Wang C., Feng L., Li W., Zheng J., Tian W., Li X.: Shape-stabilized phase change materials based on polyethylene glycol/porous carbon composite: The influence of the pore structure of the carbon materials. Solar Energy Materials & Solar Cells. 2012;**105**:21-26. DOI: 10.1016/j.solmat.2012.05.031

[6] Xiao X, Zhang P, Li M. Preparation and thermal characterization of paraffin/metal foam composite phase change material. Applied Energy. 2013;**112**:1357-1366. DOI: 10.1016/j.apenergy.2013.04.050

[7] Chen L, Zou R, Xia W, Liu Z, Shang Y, Zhu J, Wang Y, Lin J, Xia D, Cao A. Electro- and Photodriven phase change composites based on wax-infiltrated carbon nanotube sponges. ACS Nano. 2012;**6**:10884-10892. DOI: 10.1021/nn304310n

[8] Li Y, Samad YA, Polychronopoulou K, Alhassan SM, Liao K. From biomass to high performance solar-thermal and electric-thermal energy conversion and storage materials. Journal of Materials Chemistry A. 2014;**2**:7759-7765. DOI: 10.1039/c4ta00839a

[9] Liu Z, Zou R, Lin Z, Gui X, Chen R, Lin J, Shang Y, Cao A. Tailoring carbon nanotube density for modulating electro-to-heat conversion in phase change composites. Nano Letter. 2013;**13**:4028-4035. DOI: 10.1021/nl401097d

[10] Liu C, Rao Z, Zhao J, Huo Y, Li Y. Review on nanoencapsulated phase change materials: Preparation, characterization and heat transfer enhancement. Nano Energy. 2015;**13**:814-826. DOI: 10.1016/j.nanoen.2015.02.016

[11] Novoselov KS, Geim AK, Morozov S, Jiang D, Zhang Y, Dubonos S, Grigorieva I, Firsov A. Electric field effect in atomically thin carbon films. Science. 2004;**306**:666-669. DOI: 10.1126/science.1102896

[12] Li C, Shi G. Functional gels based on chemically modified Graphenes. Advanced Materials. 2014;**26**:3992-4012. DOI: 10.1002/adma.201306104

[13] Zeng M, Wang WL, Bai XD. Preparing three-dimensional graphene architectures: Review of recent developments. Chinese Physics B. 2013;**22**: 098105. DOI: 10.1088/1674-1056/22/9/098105

[14] Li Z, Liu Z, Sun H, Gao C. Superstructured assembly of Nanocarbons: Fullerenes, nanotubes, and Graphene. Chemical Reviews. 2015;**115**:7046-7117. DOI: 10.1021/acs.chemrev.5b00102

[15] Chen Z, Ren W, Gao L, Liu B, Pei S, Cheng H-M. Three-dimensional flexible and conductive interconnected graphene networks grown by chemical vapour deposition. Nature Materials. 2011;**10**:424-428. DOI: 10.1038/NMAT3001

[16] Bi H, Lin T, Xu F, Tang Y, Liu Z, Huang F. New Graphene form of Nanoporous monolith for excellent energy storage. Nano Letters. 2015;**16**:349-354. DOI: 10.1021/acs.nanolett.5b03923

[17] Zhang X, Sui Z, Xu B, Yue S, Luo Y, Zhan W, Liu B. Mechanically strong and highly conductive graphene aerogel and its use as electrodes for electrochemical power sources. Journal of Materials Chemistry. 2011;**21**:6494-6497. DOI: 10.1039/c1jm10239g

[18] Xu Y, Sheng K, Li C, Shi G. Self-assembled graphene hydrogel via a one-step hydrothermal process. ACS Nano. 2010;**4**:4324-4330. DOI: 10.1021/nn101187z

[19] Sheng K, Sun Y, Li C, Yuan W, Shi G. Ultrahigh-rate supercapacitors based on eletrochemically reduced graphene oxide for ac line-filtering. Scientific Reports. 2012;**2**: 247. DOI: 10.1038/srep00247

[20] Sui Z, Zhang X, Lei Y, Luo Y. Easy and green synthesis of reduced graphite oxide-based hydrogels. Carbon. 2011;**49**:4314-4321. DOI: 10.1016/j.carbon.2011.06.006

[21] Hu H, Zhao ZB, Wan WB, Gogotsi Y, Qiu JS. Ultralight and highly compressible graphene aerogels. Advanced Materials. 2013;**25**:2219-2223. DOI: 10.1002/adma.201204530

[22] Xu Z, Gao C. Aqueous liquid crystals of graphene oxide. ACS Nano. 2011;**5**:2908-2915. DOI: 10.1021/nn200069w

[23] Kim JE, Han TH, Lee SH, Kim JY, Ahn CW, Yun JM, Kim SO. Graphene oxide liquid crystals. Angewandite Chemite International Edition. 2011;**50**:3043-3047. DOI: 10.1002/anie.201004692

[24] Li G, Zhang X, Wang J, Fang J. From anisotropic graphene aerogels to electron- and photo-driven phase change composites. Journal of Materials Chemistry A. 2016;**4**:17042-17049. DOI: 10.1039/c6ta07587h

[25] Tsotsas E, Mujumdar AS. Modern Drying Technology, Volume 3: Product Quality and Formulation. Chichester: Wiley; 2011. 394 p. DOI: 10.1002/9783527631667

[26] Yang M, Zhao N, Cui Y, Gao W, Zhao Q, Gao C, Bai H, Xie T. Biomimetic architectured graphene aerogel with exceptional strength and resilience. ACS Nano. 2017;**11**:6817-6824. DOI: 10.1021/acsnano.7b01815

[27] Zhang P, Li J, Lv L, Zhao Y, Qu L. Vertically aligned graphene sheets membrane for highly efficient solar thermal generation of clean water. ACS Nano. 2017;**11**:5087-5093. DOI: 10.1021/acsnano.7b01965

[28] Zhao X, Yao W, Gao W, Chen H, Gao C. Wet-spun superelastic graphene aerogel millispheres with group effect. Advanced Materials. 2017;**29**. DOI: 10.1002/adma.201701482

[29] Zhang L, Li R, Tang B, Wang P. Solar-thermal conversion and thermal energy storage of graphene foam-based composites. Nanoscale. 2016;**8**:14600-14607. DOI: 10.1039/c6nr03921a

[30] Cai H, Sharma S, Liu W, Mu W, Liu W, Zhang X, Deng Y. Aerogel microspheres from natural cellulose nanofibrils and their application as cell culture scaffold. Biomacromolecules. 2014;**15**:2540-2547. DOI: 10.1021/bm5003976

[31] Zhang C, Zhai T, Turng L-S. Aerogel microspheres based on cellulose nanofibrils as potential cell culture scaffolds. Cellulose. 2017;**24**:2791-2799. DOI: 10.1007/s10570-017-1295-9

[32] Park SH, Kim HK, Yoon SB, Lee CW, Ahn D, Lee SI, Roh KC, Kim KB. Spray-assisted deep-frying process for the in situ spherical assembly of graphene for energy-storage devices. Chemistry of Materials. 2015;**27**:457-465. DOI: 10.1021/cm5034244

[33] Wang X, Li G, Hong G, Guo Q, Zhang X. Graphene aerogel templated fabrication of phase change microspheres as thermal buffers in microelectronic devices. ACS Applied Materials & Interfaces. 2017;**9**:41323-41331. DOI: 10.1021/acsami.7b13969

[34] Mondal S. Phase change materials for smart textiles - an overview. Applied Thermal Engineering. 2008;**28**:1536-1550. DOI: 10.1016/j.applthermaleng.2007.08.009

[35] Jesse TMC, Manuel M, Xia Y. Melt coaxial electrospinning: A versatile method for the encapsulation of solid materials and fabrication of phase change nanofibers. Nano Letters. 2006;**6**:2868-2872. DOI: 10.1021/nl0620839

[36] Chen C, Wang L, Huang Y. Electrospun phase change fibers based on polyethylene glycol/cellulose acetate blends. Applied Energy. 2011;**88**:3133-3139. DOI: 10.1016/j.apenergy.2011.02.026

[37] Wen GQ, Xie R, Liang WG, He XH, Wang W, Ju XJ, Chu LY. Microfluidic fabrication and thermal characteristics of core–shell phase change microfibers with high paraffin content. Applied Thermal Engineering. 2015;**87**:471-480. DOI: 10.1016/j.applthermaleng.2015.05.036

[38] Xu Z, Zhang Y, Li PG, Gao C. Strong: Conductive, lightweight, neat graphene aerogel fibers with aligned pores. ACS Nano. 2012;**6**:7103-7113. DOI: 10.1021/nn3021772

[39] Yu D, Goh K, Wang H, Wei L, Jiang W, Zhang Q, Dai L, Chen Y. Scalable synthesis of hierarchically structured carbon nanotube-graphene fibres for capacitive energy storage. Nature Nanotechnology. 2014;**9**:555. DOI: 10.1038/NNANO.2014.93

[40] Liu Z, Li Z, Xu Z, Xia Z, Hu X, Kou L, Peng L, Wei Y, Gao C. Wet-spun continuous graphene films. Chemistry of Materials. 2014;**26**:6786-6795. DOI: 10.1021/cm5033089

[41] Kou L, Liu Z, Huang T, Zheng B, Tian Z, Deng Z, Gao C. Wet-spun, porous, orientational graphene hydrogel films for high-performance supercapacitor electrodes. Nanoscale. 2015;**7**:4080-4087. DOI: 10.1039/c4nr07038k

[42] Xiong Z, Liao C, Han W, Wang X. Mechanically tough large-area hierarchical porous Graphene films for high-performance flexible Supercapacitor applications. Advanced Materials. 2015;**27**:4469-4475. DOI: 10.1002/adma.201501983

[43] Ye S, Zhang Q, Hu D, Feng J. Core-shell-like structured graphene aerogel encapsulating paraffin: Shape-stable phase change material for thermal energy storage. Journal of Materials Chemistry A. 2015;**3**:4018-4025. DOI: 10.1039/c4ta05448b

[44] Zhong Y, Zhou M, Huang F, Lin T, Wan D. Effect of graphene aerogel on thermal behavior of phase change materials for thermal management. Solar Energy Materials & Solar Cells. 2013;**113**:195-200. DOI: 10.1016/j.solmat.2013.01.046

[45] Zhang K, Han B, Xun Y. Electrically conductive carbon nanofiber/paraffin wax composites for electric thermal storage. Energy Conversion & Management. 2012;**64**:62-67. DOI: 10.1016/j.enconman.2012.06.021

Chapter 7

Optimization of the Phase Change Random Access Memory Employing Phase Change Materials

Daolin Cai, Zhitang Song and Yifeng Chen

Additional information is available at the end of the chapter

http://dx.doi.org/10.5772/intechopen.74786

Abstract

Phase-change random access memory (PCRAM) is a semiconductor device based on phase change material (PCM). The SET speed is the bottleneck of limiting the speed of PCRAM. Extract the electrical parameters of the SET operation of the PCRAM test chip and analyze the process of the SET operations. It is found that adding a high and narrow pulse before a single pulse (SP) benefits the SET resistance reduction and the SET speed improvement. A dual pulses SET (D-SET) method is proposed and optimized. The mechanism of D-SET is that the first pulse forms a large optimum temperature field cover over all regions of the PCM material. When the first pulse is converted to the second pulse, the optimum temperature field shrinks and causes the amorphous regions to rapidly crystallize from the edge to the center. On the 40 nm PCRAM test chip, the SET time of D-SET method is under 300 ns. Compared with the conventional SET method such as SP and staircase down pulses (SCD), the D-SET method is optimal for SET performance such as SET resistance distribution, SET speed, and the anti-drift ability.

Keywords: PCRAM, phase change material (PCM), SET operation, resistance distribution, anti-drift

1. Introduction

Phase-change random access memory (PCRAM) is widely investigated as one of the most promising candidates for nonvolatile memory [1]. The storage cell in PCRAM is based on a phase change material (PCM). Interest in PCRAM technology was renewed by the discovery of fast recrystallizing materials, GeTe [2], $Ge_{11}Te_{60}Sn_4Au_{25}$ [3], $Ti_{0.4}Sb_2Te_3$ [4], and $Cr_{0.2}Sb_2Te_3$ [5]. A pseudo-binary alloys along the GeTe-Sb_2Te_3 tie line, such as $Ge_1Sb_2Te_4$, $Ge_1Sb_4Te_7$, and the most commonly applied material for both optical and electrical applications, $Ge_2Sb_2Te_5$ (GST) [6].

Employing PCM, in 2006, 512 MB PCRAM chip was reported. Intel and Micron recently announced a new 128 GB "3D XPoint memory" technology [7]. High speed, high density, low voltage, and compatibility with standard CMOS technology performance ensure PCRAM superiority [8–10]. The storage cell is constituted by a thin-film PCM layer in contact with a metallic heater. When a programming voltage or current is applied to the storage cell, a high current density will flow into the resistive heater, raising the temperature by Joule effect. PCM in the active region close to the heater heats up, thus causing the phase transition between the RESET and SET states. The PCM can be changed from low resistive (crystalline) to high resistive (amorphous) state, named as RESET operation; vice versa, from high resistive (amorphous) to low resistive (crystalline) state named as SET operation.

Conventionally, SET program operation is achieved by means of a single pulse (SP) of a couple of hundreds of nanoseconds. The resulting SET-state cell resistance distribution (hereafter referred to as SET distribution) typically turns out to be affected by spreads in cell physical parameters, which can degrade the SET distribution width. This leads to a reduced spacing between the SET and the RESET distribution and, hence, to a decreased safe margin for read operations. Compared with the RESET speed of PCRAM, the SET speed of PCRAM is much slower; so the SET speed is the bottleneck of limiting the speed of PCRAM. This chapter focuses on the SET operation optimization of PCRAM, mainly research on the influence of the relevant factors of SET operation pulse on SET operation and how to optimize the SET operation pulse. The SET operation speed is improved by optimizing the SET operation pulse. The mechanism of the SET process is analyzed, and the improved SET operation pulse is proposed and implemented. It is mainly divided into three aspects as follows: (1) the influence of the magnitude and width of the SET pulse on PCRAM; (2) study on the dual pulse SET (D-SET) operation; (3) comparison of D-SET with the common SET methods.

Many improved SET operation methods are proposed and applied in the PCRAM chip. In 2005, the multiple step-down pulse generator (MSPG) SET technique (**Figure 1(a)**) was applied to the 64 MB PCRAM chip released by Samsung [11]. Because of the influence of the path resistance, different address storage cells require a different SET pulse to full crystallization. In the MSPG technology, the SET current pulse is swept to cover all the cell-to-cell variations of the SET current windows, so the probability of the SET failure can be reduced. Not only can the SET success rate but also the consistency of SET resistance can be improved. **Figure 1(b)** illustrates that the utilization of MSPG to the SET operation reduces the broadness of the right side of SET distribution and widens the margin for reading window.

In 2007, Samsung reported an arbitrary slow-quench (ASQ) pulse scheme to improve the write time of the SET data in a 512 MB PCRAM chip based on 90 nm process [12]. It is composed of a maximum current decision part, a slow-quench slop decision part, a minimum current decision part, and a voltage driver with wide operation range as shown in **Figure 2(a)**. The scheme is used effectively to enhance distributions and reliability of cell data through write-verify process. **Figure 2(b)** shows a measured data of voltage level of SET signal and output of the ASQ, which has a slow quench waveform with 500 ns pulse width.

In addition, STMicroelectronics proposed a technology similar to ASQ technology knows as Set-Sweep Programming (SWP) [13, 14], as shown in **Figure 3**. It consists in applying a conventional RESET pulse to melt the GST but with a very slow-stepped or linear quenching so that, thanks to the slow falling edge, the material has time enough to crystallize and to move into the low resistance state.

http://dx.doi.org/10.5772/intechopen.74786

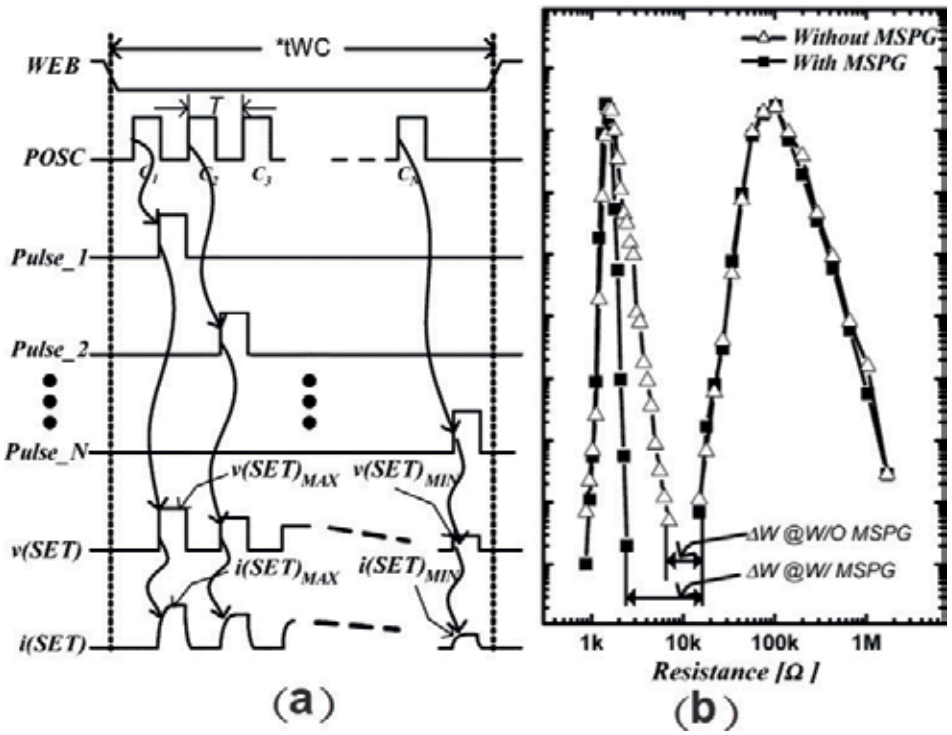

Figure 1. (a) Multiple and step-down pulse generator (MSPG); (b) GST resistance distribution without/with MSPG [11].

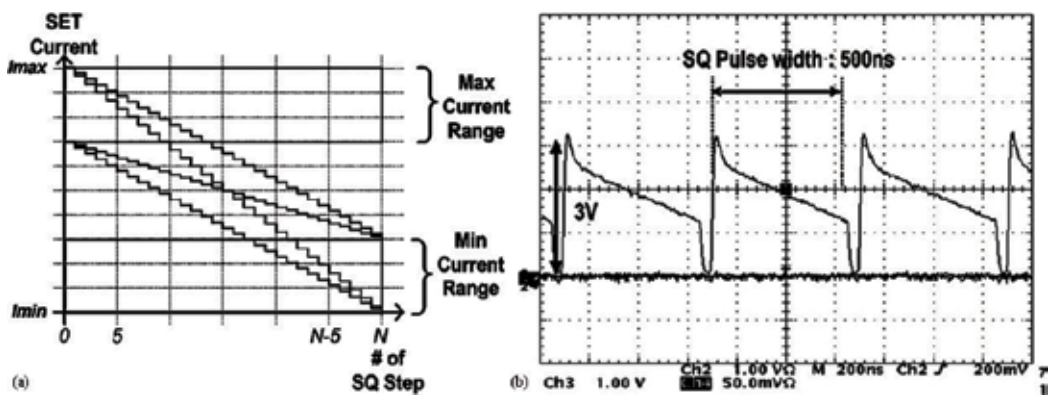

Figure 2. Arbitrary slow-quench shaper. (a) Versatile SQ pulse waveforms. (b) Measured waveform of SET node [12].

A staircase-down (SCD) SET pulse is reported [15], which can be seen as the sequence of N elementary pulses having the same length T_S and decreasing magnitudes S_{N-1}, S_{N-2},…, S_0 (**Figure 4**). This SCD technique allows different optimum SET voltages to be applied to different cells being programmed simultaneously. It can compensate for spreads in cell physical parameters, thus obtaining narrow SET distributions and improved read margin.

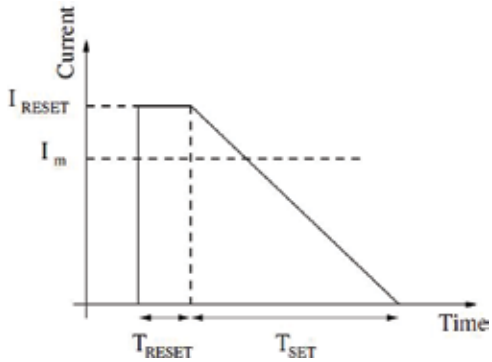

Figure 3. Set program pulse. The constant current level IRESET is higher than the melting current Im in order to melt the chalcogenide before the slow cooling [13].

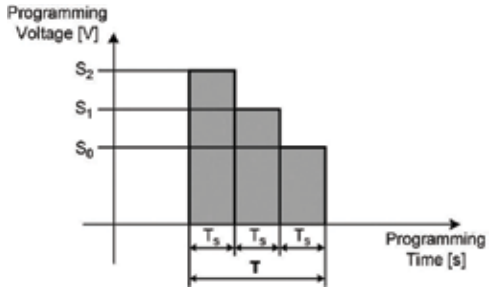

Figure 4. Staircase-down programming pulse (N = 3) [15].

2. SET pulse magnitude and width

2.1. Thermal properties

In order to RESET the PCRAM cell into its amorphous state, a short electrical pulse is applied to the bottom electrode contact (BEC). The thermal pulse is quenched rapidly to cause the molten region to cool to its amorphous state. For the case of SET programming, an electrical pulse is applied to the PCRAM cell that is sufficient to increase the temperature of the programming region above the crystallization temperature (Tcryst) over a time period sufficiently long to crystallize the phase change material. Typically, a material offering high Tcryst generally leads to a better thermal stability and thus longer data retention of stored data. Note that at Tx, crystallization occurs in microseconds. In contrast, at the higher temperature of Tcryst shown in **Figure 5**, sufficient recrystallization of the amorphized portion to create a high conductance path through a memory cell can occur in less than 1 μs. This crystallization temperature Tx can be readily measured on blanket films of PCRAM using electrical techniques. Thus, Tx is widely used to characterize new candidate PCRAM [16].

http://dx.doi.org/10.5772/intechopen.74786

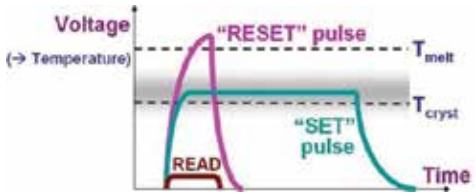

Figure 5. Programming of a PCM device involves application of electrical power through applied voltage, leading to internal temperature changes that either melt and then rapidly quench a volume of amorphous material (RESET), or hold this volume at a slightly lower temperature for sufficient time for recrystallization (SET). The temperature at which recrystallization is very rapid (<1 μs), Tcryst ~ 400°C, is lower than the melting temperature, Tmelt ~ 600–650°C. A low voltage is used to sense the device resistance (READ), so that the device state is not perturbed [16].

2.2. SET pulse magnitude

In order to study the effects of the SET pulse magnitude on the resistance of the PCRAM cell, a fixed width SET pulse is used to SET operation for the RESET state of PCRAM test chip samples. The SET distributions with the different SET pulse magnitudes are shown in **Figure 6(a)**. The cell percent of the SET resistance value less than 100 kΩ (log(resistance) < 5) is listed in **Table 1**.

From the perspective of the SET distribution of array with SET resistance less than 100 kΩ as the standard, it can be seen that 0.3 mA SET current is the optimal SET pulse magnitude. For each cell, its optimal SET current is inconsistent, and its optimal SET current (obtaining the minimum SET resistance) is shown in **Figure 6(b)**. The cell proportion with 0.3 mA SET current operation as the optimal SET current is majority, and the optimal SET current of most cells (98.94%) in the array is between 0.2 and 0.6 mA. It is obvious that the optimal SET conditions are in favor of the array resistance distribution.

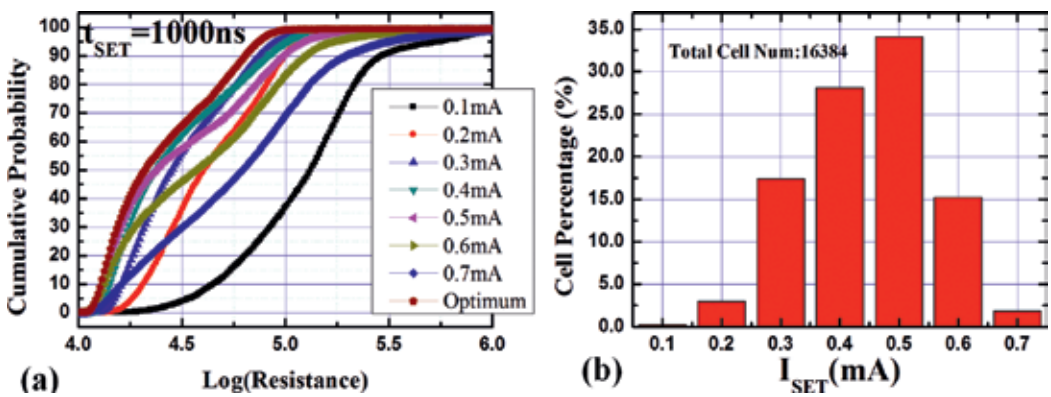

Figure 6. (a) SET distribution with the different SET pulse magnitude; (b) histogram statistics of the cell percent with the different SET current [21].

SET current (mA)	0.1	0.2	0.3	0.4	0.5	0.6	0.7
Cell percent (%)	37.183	90.55	96.58	94.75	91.06	83.41	69.54

Table 1. Cell percent of the SET resistance value (<100 kΩ) with the different SET pulse magnitude.

2.3. SET pulse width

In order to study the effect of the SET pulse width on the resistance of the PCRAM cell, a fixed magnitude SET pulse is used for SET operation from the RESET state of PCRAM test chip samples. 1.5 mA 200 ns RESET current was used to RESET to the amorphous state of the PCRAM array, and then the array was operated with the SET pulse with the different pulse width. According to the experimental results of the SET pulse magnitude, the optimal SET pulse magnitude is 0.3 mA and the pulse width is 200, 300, 500, 1000, and 2000 ns, respectively. The SET distribution with the different pulse width is shown in **Figure 7**, with a cell percent of the SET Resistance value less than 100 kΩ (log(resistance) < 5) is listed in **Table 2**.

The results show that the longer SET pulse width is, the better SET distribution of the array is. When the time is more sufficient, the ratio of crystallization is higher. And with the SET time increasing, the effect of the optimization of the SET distribution is smaller and smaller because the crystallization ratio in the cell is higher and higher until it is saturated. In the sample, the SET pulse width needs to reach 1000 ns to obtain a better resistance distribution. It can be seen that when SP is used in a SET operation, the pulse width demand is longer and the SET speed is slow.

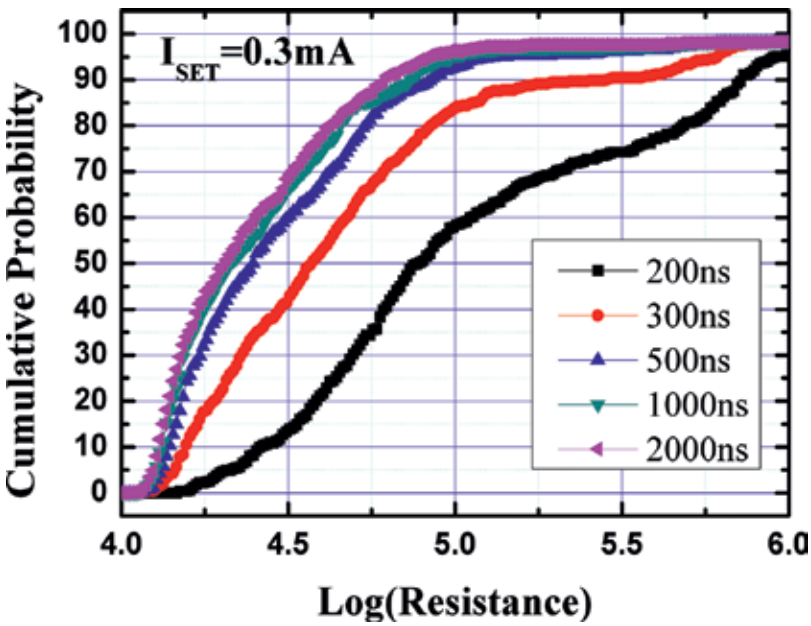

Figure 7. SET distribution with the different pulse width.

SET width (ns)	200	300	500	1000	2000
Cell percent (%)	58.49	84.12	92.77	95.51	96.29

Table 2. Cell percent of the SET resistance value (<100 kΩ) with the different SET pulse width.

2.4. SET process research

To ensure a high enough SET success rate, it is necessary to ensure a sufficient width pulse, which poses a challenge to the speed of the SET operation. In order to have a deeper understanding of the SET operation process, we also need to understand the change of the SET resistance of the array at all times when the SET operation starts. Therefore, we tested the variation of the average resistance of the array with the SET pulse operation time, as shown in **Figure 8**. The array size is 16 kbits, and the test time is 60–630 ns, and the resistance value is tested every 30 ns. Before the SET operation, 1.5 mA 200 ns RESET pulse is used to operate the array. In order to study the influence of SET current, repeated experiments are performed under the different sets of SET current.

The test results show that the resistance variation with the time in the SET process can be divided into three stages. In the first stage, the resistance maintains high resistance. It is particularly

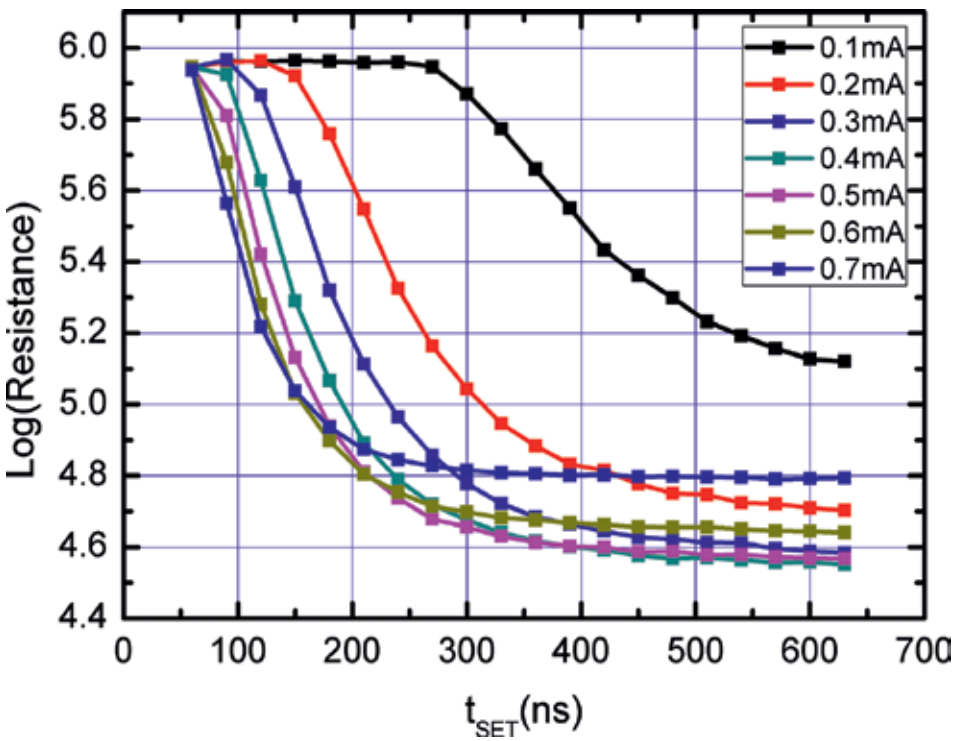

Figure 8. SET resistance variation with the time in the set process.

noticeable when the SET current operation is 0.1 mA. This stage time is affected by the SET current. The larger SET current is, the less time it will take. In the second stage, the resistance variation is the most intense, which decreases rapidly with the increase in SET time. In the third stage, the resistance variation will enter a stationary phase, and the resistance will decrease slowly with the increase in SET time. The larger SET current is, the faster third stage occurring is, and the resistance at this stage is determined by the SET current magnitude.

The variation of SET resistance in different time periods in the SET process is calculated to analyze the SET speed as shown in **Figure 9**. In the SET process, the SET speed is not constant, but at some time, the speed will reach the extreme value. Furthermore, the larger the SET current is, the earlier extreme value appearing is.

The crystallization of the phase change materials is divided into nucleation and crystal growth, and the GST alloy is reflected in the nucleation dominated recrystallization [17]. The crystallization process of the GST alloy is the incubation of crystal nucleus and then the crystal grows. For the SET operation of the PCRAM chip, when the SET pulse is injected, on the one hand, due to the parasitic parameters of the circuit and the cell itself, the cell threshold switching needs some time [18]. On the other hand, the inside of the cell goes through an incubation process [19]. These two causes lead to the first stage of the SET process. However, when the SET current is larger, the influence of the parasitic parameters can be more favorably overcome. When the temperature field formed by the current is higher, it is more favorable for the nucleation incubation [19]. Therefore, the larger is the SET current, the shorter is the first stage.

When the nucleus of the cell begins to grow, the resistance begins to drop rapidly and enters the second stage of the SET process. The SET current heats the electrode and forms a temperature field

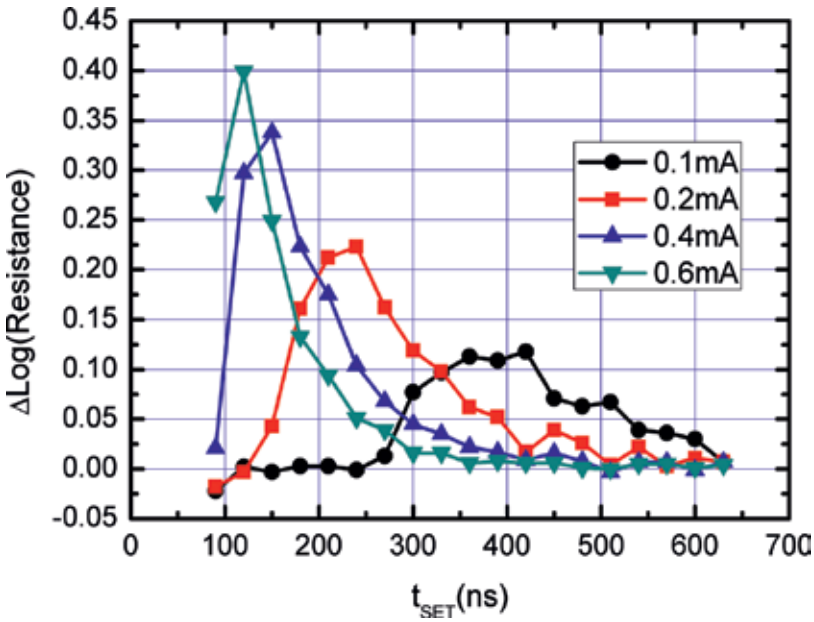

Figure 9. Relationship between the SET resistance variation velocity with the SET time.

inside the cell. There is a temperature gradient in this temperature field as shown in **Figure 10**. This makes the internal temperature of the cell not consistent; the center temperature is higher, and the edge temperature is lower. This makes the incubation time for each region inconsistent. A phenomenon appears in **Figure 9**, whereby the speed of the cell resistance decreasing in the early stages will gradually increase; this is because the cells within different areas do not match the moment into the growth stage. When the area of the cell into growth stage is more and more, the resistance decreases faster. When all amorphous areas of the cell begin to grow, it will reach a rate of extreme value. Except the temperature effect of nucleation speed, the study of Sebastian et al. [20] shows that the velocity of crystal growth also has a great relationship with temperature. The relationship between the velocity and temperature of crystal growth is shown in **Figure 11**.

As shown in **Figure 11**, there is a temperature that allows the crystal to grow the fastest, at about 750 K. In the second stage of the SET process, the growth velocity in the different regions of the cell is different due to the different temperatures, so the time required for completing crystallization of each part is different. The SET process will enter the third stage when the crystal of each region gradually grows to form a crystal channel within the cell. At this stage, as the SET time continues to lengthen, the crystal channels in the cell become more and more, and the resistance still slowly decreases. The three stages of the SET process are shown in **Figure 12**. When the SET current is small, the growth rate of the amorphous region edge can be slow, which can make the crystal channel difficult to form, and the resistance cannot be reduced rapidly in the SET pulse time. This is the reason why the SET distribution is poor using the SET current operation of 0.1 mA in **Figure 5**. When the SET electric current is larger, the growth velocity is faster in the edge. But it may cause the temperature to be too high to be RESET in the center and also can lead to residual amorphous. Therefore, the SET distribution is very poor using the 0.7 mA SET current.

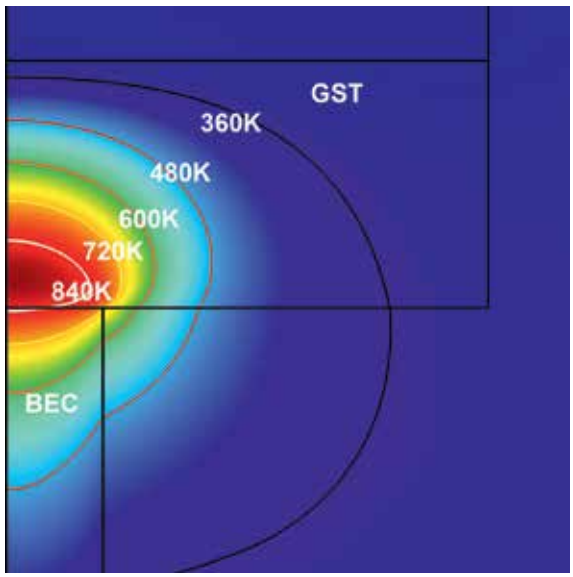

Figure 10. Internal temperature field of the unit within the SET process.

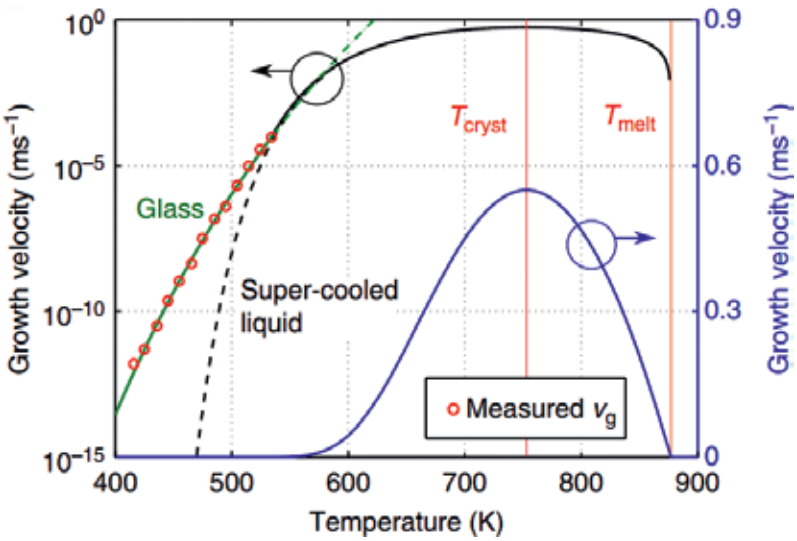

Figure 11. Relationship between the velocity of crystal growth and temperature [20].

Figure 12. Nucleation, growth and saturation stage diagram of PCM cell in the SET process.

3. D-SET operation method

Given the study of the SET process in the last section, it can be seen that the large SET operation current is beneficial to improve the SET speed. On the one hand, because the larger operation current can overcome the influence of the parasitic parameters, which promotes the rapid nucleation; On the other hand, the higher temperature can increase the growth rate of PCRAM crystal, which reduces the time of the second stage. However, a single high SET current can cause too high temperature in the phase change cell and cannot be crystallized, resulting in too many amorphous residues, which in turn result in the failure of the SET operation. Therefore, it is not feasible to use a single lifting SET current to speed up the SET operation, and the shape of SET pulse needs to be optimized.

http://dx.doi.org/10.5772/intechopen.74786

3.1. D-SET

Considering the large SET current required for the promotion of the SET speed, a high power pulse (HPP) is added before the single box SET pulse to improve the SP SET effect on the SET distribution and speed. To verify the feasibility of this improved pulse, we verified the SET effect of SP and improved SET pulse in 16 kbits PCRAM array. The illustration shows that the shape of SP (without HPP) and improved pulse (with HPP) in **Figure 13**.

Figure 13(a) shows the relationship between the SET current I_{SET} and the average SET resistance obtained by the experiment. According to the test results, the relationship between the single pulse and the HPP pulse is consistent with that of the SET resistance. The SET resistance is the minimum when the I_{SET} is moderate. The difference is that in any I_{SET} comparison, the average SET resistance obtained by using the HPP pulse is much lower than that of SP. When the I_{SET} is smaller, the gap is larger. In addition, using the HPP pulse, when 0.3 mA I_{SET} made the smallest average SET resistance, its minimum average SET resistance below 20 kΩ, but the corresponding minimum average SET resistance using SP is over 40 kΩ. The HPP pulse can effectively improve the SET effect.

Figure 13(b) shows the relationship between SET pulse width t_{SET} and average SET resistance. In this case, the array used the same RESET pulse operation prior to the SET operation to make the array initial high resistance state. The magnitude and width of the RESET pulse is 1.5 mA, 200 ns respectively. The I_{SET} SET current of SP and the HPP pulse is 0.3 mA, while for the HPP pulse, the magnitude of HPP before its SET pulse is 1.5 mA and the pulse width is 100 ns. As you can see, for SP, the first stage is about 100 ns, and the SET resistance is still high in this stage. In the second stage, the SET resistance begins to decline slowly with the length of the SET pulse width. The average SET resistance dropping below 100 kΩ takes 250 ns, and it is not capable of reducing the resistance under 50 kΩ within 500 ns. For the HPP pulse, the

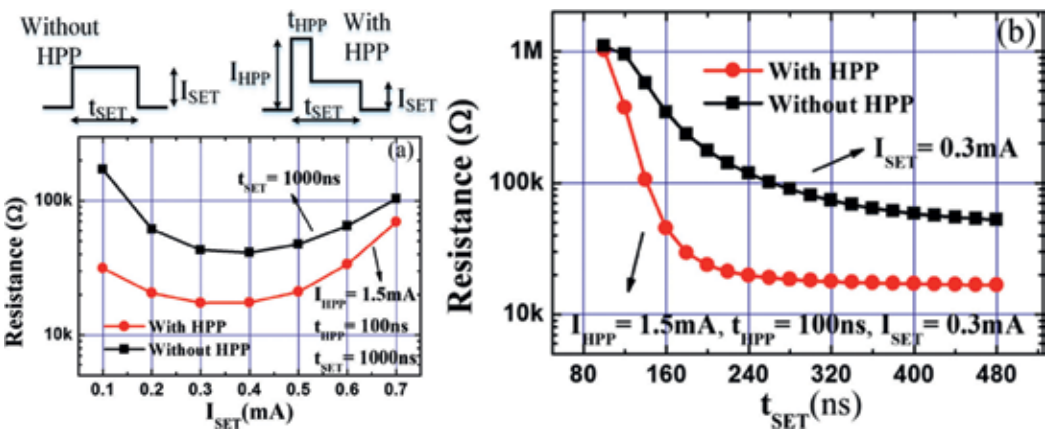

Figure 13. Comparison of SP and improved pulse SET effect [21].

average SET resistance drops rapidly to below 20 kΩ within 240 ns. It can be seen that the HPP pulse can effectively accelerate the SET speed so that the cell is fully crystallized.

Based on the abovementioned comparison experiment, the SET velocity of the HPP pulse was increased and the SET resistance was reduced. So, we designed a new SET operation method called Dual Pules SET (D-SET) [21]. A pulse sequence containing two pulses used in SET operation of the PCRAM cell, in which the first pulse is the HPP pulse, and the subpulse is a regular SET pulse.

3.2. Optimization of the D-SET method

The specific choice of the first pulse and the subpulse is related to the effect of the SET operation for the D-SET. In order to further study the mechanism of the first HPP pulse and further optimize the HPP pulse, the magnitude and pulse width of the HPP pulse were experimentally studied. Firstly, the SET distribution of the HPP pulse width is studied.

From **Figure 14**, it can be seen that when the HPP pulse width increased from 50 to 100 ns, the SET resistance obtained is gradually moving to a lower value. When the HPP pulse width is over 100 ns, the improvement of the SET distribution is increased with increasing HPP pulse width. Considering that the HPP pulse magnitude is the same as that of the RESET pulse, this is similar to the effect of the RESET pulse width.

To optimize the HPP, the effect of I_{HPP} on SET distribution is characterized. As shown in **Figure 15**, the I_{HPP} ranges from 1.1 to 1.5 mA while the I_{RESET} is fixed at 1.5 mA. In the D-SET pulse operation, the HPP pulse width is 100 ns, the subpulse magnitude is 0.3 mA and the width is 900 ns.

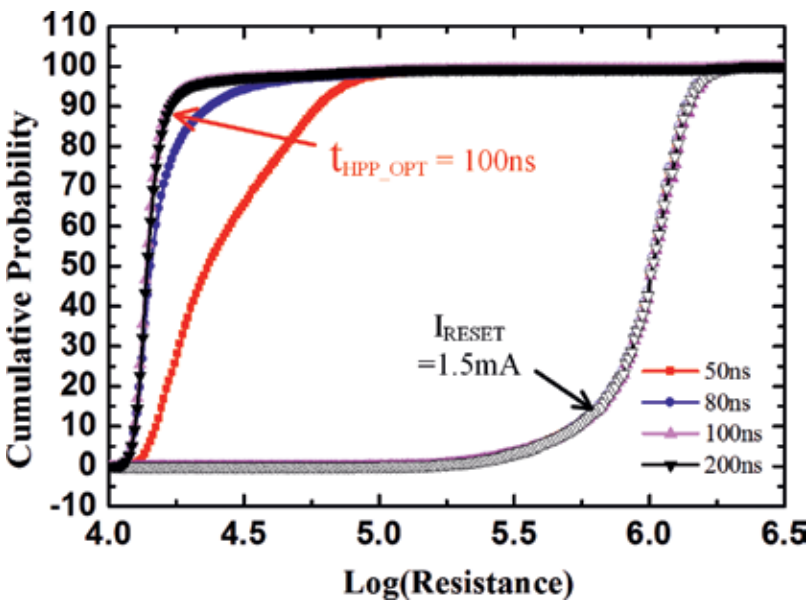

Figure 14. Effect of the HPP pulse width on the SET resistance distribution [21].

http://dx.doi.org/10.5772/intechopen.74786

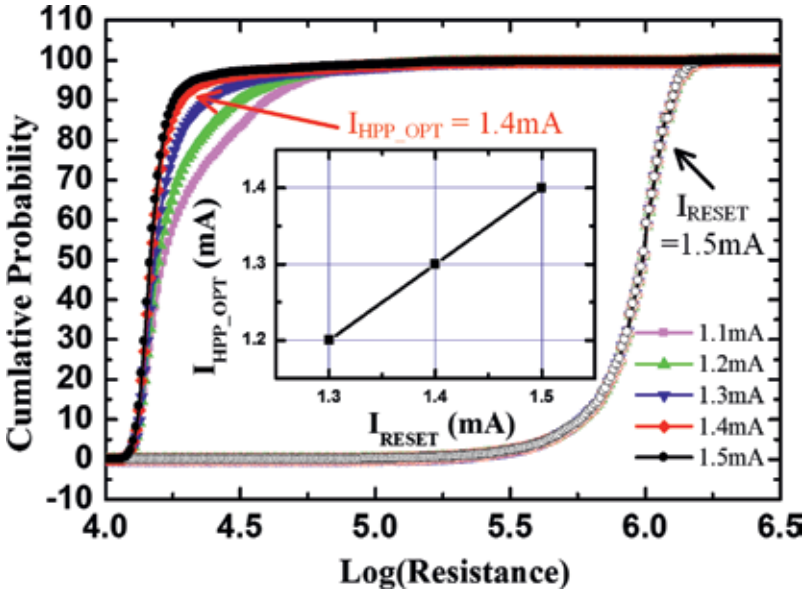

Figure 15. Influence of the HPP magnitude on SET distribution [21].

As the I_{HPP} increases, the SET distribution improves. And when I_{HPP} is over 1.4 mA, this improvement on the SET distribution saturates. This is because that increasing I_{HPP} will extend the favorable temperature annulus. The larger the annulus is, the more amorphous regions meet the favorable temperature when the annulus shrinks. When the annulus is beyond the active region, all the amorphous regions are covered and the improvement on SET resistance is optimal. The specific I_{HPP} that achieves optimal SET performance is called I_{HPP_OPT}. Since the favorable temperature is lower than the melt temperature, I_{HPP_OPT} is lower than I_{RESET}, The correlations of I_{RESET} vs. I_{HPP_OPT} is shown in the inset of **Figure 15**. The corresponding I_{HPP_OPT} to I_{RESET} of 1.5, 1.4, and 1.3 mA are 1.4, 1.3 and 1.2 mA, respectively. It suggests that the smaller the amorphous area that RESET pulse creates, the smaller the favorable temperature annulus needed.

3.3. Analysis of the mechanism of D-SET

For SET process, the crystal growth plays an important role in crystallization and the crystal growth velocity has a huge dependence on temperature. It is reported that the crystal growth velocity is over 8 orders of magnitude spanning a temperature range from 415 to 580 K [22], and the maximal crystal growth velocity appears at near 750 K [9]. A fast crystallization needs to ensure the amorphous region crystallized under favorable temperature range for crystal growth.

When applying the SP without HPP, the favorable temperature annulus is small and near the BEC as shown in **Figure 16**. The temperature near the interface is too low to ensure fast growth. As a result, there is amorphous residual at the outside of the active region when SET pulse terminates. As for the single pulse with HPP, the HPP creates a favorable temperature annulus of large radius, which may be beyond the amorphous region depending on I_{HPP}. When the HPP switches to the single pulse, the device cools off to a steady state temperature

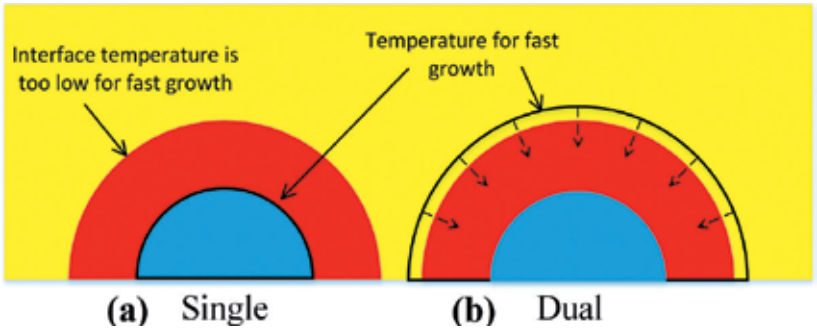

Figure 16. Schematic illustration of the different crystallization process when applying (a) single pulse, and (b) dual pulse [21].

and the favorable temperature annulus shrinks toward the center. As this annulus sweeps in, the outside of the active region also has an opportunity to crystallize at favorable temperature. This is probably the reason why for crystallization that applying HPP pulse is much faster and more sufficient.

3.4. Performance test of D-SET

The D-SET method has excellent advantages to the SET speed and the resistance distribution.

The specific currents as well as the timing for each pulse procedure are described in the inset of **Figure 17**. The SET distributions obtained with those three kinds of SET methods are showed in **Figure 17**. The same RESET pulses are applied before each SET operation, which results in the same RESET resistance distribution. As shown in **Figure 17**, it is found that D-SET results in the lowest and narrowest SET resistance distribution. In the same limited SET time of 300 ns, the proportion of cells with SET resistance under 30 kΩ (log(resistance)<4.5) for D-SET, SP and SCD is 98, 8, and 35%, respectively.

In addition to achieving a good SET distribution, the SET resistance of D-SET is more prominent than the other two SET methods. The resistance drift of the SET resistance obtained by applying those three SET methods are also evaluated. The resistance drift has been described in the literature according to the power-law empirical equation (1) [23]:

$$R(t) = R_0 \left(\frac{t}{t_0}\right)^{v} \tag{1}$$

where t_0 is a normalizing time value, R_0 is the resistance at time t_0, and v is the drift exponent. To extract the drift exponent, both the resistance of PCRAM cells right after SET operation and after an annealing of 3 h at 110°C (resistance read performed at room temperature) are collected firstly. The statistical results are presented in **Figure 18(a)**. Then the corresponding drift coefficients of each cell are calculated by Eq. (1) and the statistics are reported in **Figure 18(b)**. As shown in **Figure 18(a)** and **(b)**, the D-SET method results in the smallest resistance drift as well as in the smallest drift coefficient dispersion. The mean drift coefficients of SET resistance obtained by SP, D-SET, and SCD are 0.056, 0.018, and 0.041, respectively. The correlations of

http://dx.doi.org/10.5772/intechopen.74786

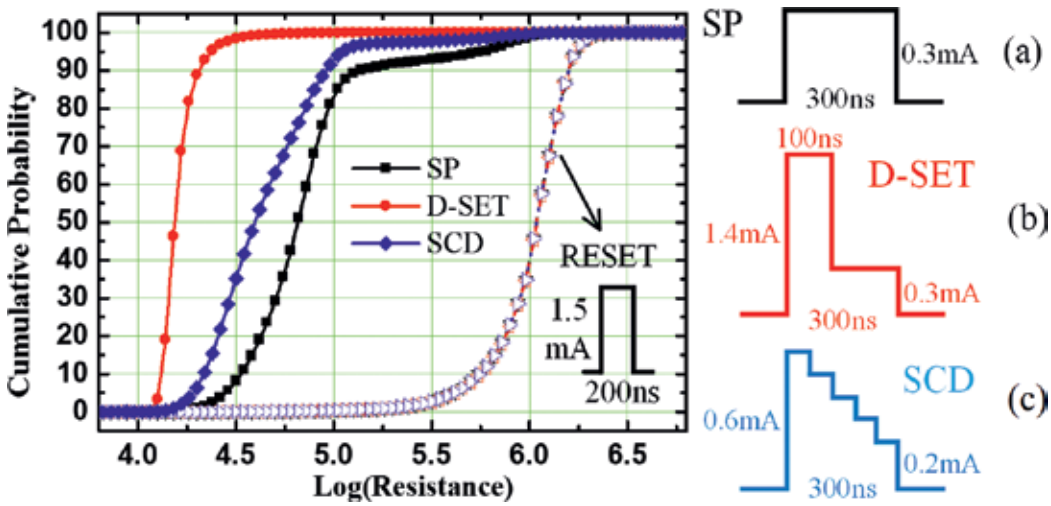

Figure 17. Resistance distributions obtained with three kinds of SET pulses: (a) SP, (b) D-SET, and (c) SCD. The schematic of the SET pulses are showed in the inset figure [21].

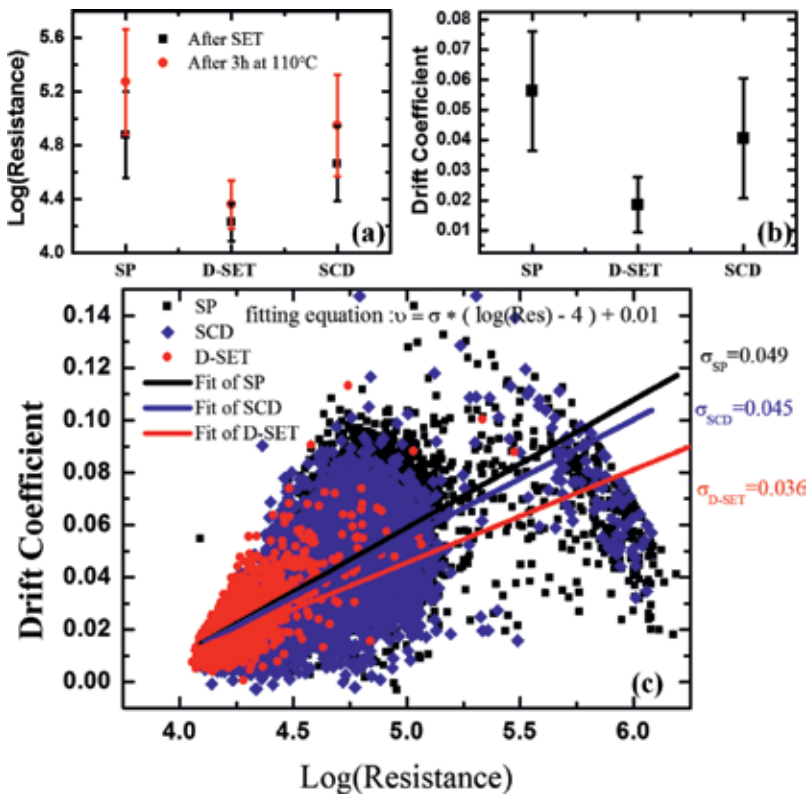

Figure 18. Comparison of (a) the programmed SET resistance, (b) the corresponding drift coefficient, and (c) correlations of drift coefficient vs. SET resistance obtained with SP, D-SET and SCD [21].

drift coefficient vs. SET resistance are shown in **Figure 18(c)**. A strong correlation between the drift coefficient and the programmed resistance has been observed. It shows that the higher the resistance, the higher the value of ν, as described in the literature [24, 25] According to Ref. 22, the drift coefficient values of SET state resistance (less than 10 kΩ) are lower than 0.01. The correlations are fitted with the fitting equation (2):

$$\nu = \delta * (\log(R) - 4) + 0.01 \tag{2}$$

where ν is the drift coefficient value, R is the SET resistance and δ is the fitting parameter which stands for the gradient of drift coefficient. The smaller the gradient is, the slower the drift coefficient increases with resistance. The fitting parameters of SP, SCD, and D-SET are 0.049, 0.045, and 0.036, respectively. It suggests that the drift benefits arise not only from the lower SET resistance but also the smaller gradient. It can be seen that the anti-drift property of the dual pulse is not only because of the smaller SET resistance but also because its drift factor is smaller with the change of resistance.

4. Conclusions

The field of PCRAM based on PCM research has gained momentum in the last decade because of its interesting device and material properties that make them an excellent candidate for future nonvolatile memory applications. This chapter gives an overview of the SET operation method. D-SET has been presented applying HPP before a single SET pulse which benefits the SET speed and SET resistance. The mechanism and performance of the D-SET has been characterized and analyzed. This D-SET is capable of achieving lower SET distribution and smaller resistance drift than the conventional SET method within 300 ns on a 64 MB PCRAM test chip in 40 nm CMOS process.

Acknowledgements

This work was supported in part by the "Strategic Priority Research Program" of the Chinese Academy of Sciences (XDA09020402), National Natural Science Foundation of China (61176122, 61106001).

Author details

Daolin Cai*, Zhitang Song and Yifeng Chen

*Address all correspondence to: caidl@mail.sim.ac.cn

State Key Laboratory of Functional Materials for Informatics and Nanotechnology Laboratory, Shanghai Institute of Micro-system and Information Technology, Chinese Academy of Sciences, Shanghai, China

References

[1] Bez R. Chalcogenide PCM: A memory technology for next decade. In: Proceedings the IEEE International Technical Digest on the Electron Devices Meeting (IEDM' 09); 7-9 December 2009; Baltimore, Maryland, USA. New York: IEEE; 2009. pp. 89-92

[2] Chen M, Rubin KA, Barton RW. Compound materials for reversible, phase–change optical–data storage. Applied Physics Letters. 1986;**49**(9):502-504

[3] Yamada N, Takenaga M, Takao N. Te–Ge–Sn–Au phase change recording film for optical disk. In: Proceedings the International Society for Optics and Photonics (SPIE' 86); 1986. p. 7

[4] Song Z, Zhan Y, Cai D, Liu B, Chen Y, Ren J. A phase change memory chip based on TiSbTe alloy in 40-nm standard CMOS technology. Nano-Micro Letters. 2015;**7**(2):172-176. DOI: 10.1007/s40820-015-0030-z

[5] Rao F, Ding K, Zhou Y, Zheng Y, Xia M, Lv S, Song Z, Feng S, Ider R, Mazzarello R, Zhang W, Ma E. Reducing the stochasticity of crystal nucleation to enable subnanosecond memory writing. Science. 2017;**358**:1423-1427. DOI: 10.1126/science.aao3212

[6] Yamada N, Ohno E, Nishiuchi K, Akahira N, Takao M. Rapid–phase transitions of GeTe–Sb_2Te_3 pseudobinary amorphous thin–films for an optical disk memory. Journal of Applied Physics. 1991;**69**(5):2849-2856. DOI: 10.1063/1.348620

[7] 3D XPoint: A Guide To The Future Of Storage-Class Memory 2015 [Internet]. 2016. Available from: http://www.tomshardware.com/reviews/3d-xpoint-guide,4747.html [Accessed: 2016-11-25]

[8] Cai D, Chen H, Wang Q, Chen Y, Song Z, Wu G, Feng S. An 8-Mb phase-change random access memory chip based on a resistor-on-via-stacked-plug storage cell. IEEE Electron Device Letters. 2012;**33**(9):1270-1272. DOI: 10.1109/LED.2012.2204952

[9] Kolobov AV, Fons P, Frenkel AI, Ankudinov AL, Tominaga J, Uruga T. Understanding the phase-change mechanism of rewritable optical media. Nature Materials. 2004;**3**(10):703-708. DOI: 10.1038/nmat1215

[10] Sun ZM, Zhou J, Ahuja R. Structure of phase change materials for data storage. Physical Review Letters. 2006;**96**(5):055507-1-055507-4. DOI: 10.1103/PhysRevLett.96.055507

[11] Oh HR, Cho BH, Cho WY, Kang S, Choi BG, Kim HJ, Kim KS, Kim DE, Kwak CK, Byun HG. Enhanced write performance of a 64-Mb phase-change random access memory. IEEE Journal of Solid-State Circuit. 2006;**41**(1):122-126. DOI: 10.1109/JSSC.2005.859016

[12] Lee KJ, Cho BH, Cho WY, Kang S, Choi BG, Oh HR, Lee CS, Kim HJ, Park JM, Wang Q, Park MH, Ro YH, Choi JY, Kim KS, Kim YR, Shin IC, Lim KW, Cho HK, Choi CH, Chung WR, Kim DE, Yoon YJ, Yu KS, Jeong GT, Jeong HS, Kwak CK, Kim CH, Kim K. A 90 nm 1.8 V 512 Mb diode-switch PRAM with 266 MB/s read throughput. IEEE Journal of Solid-State Circuit. 2008;**43**(1):150-159. DOI: 10.1109/JSSC.2007.908001

[13] Bedeschi F, Boffmo C, Bonizzoni E, Resta C, Torelli G, Zella D. Set-sweep programming pulse for phase-change memories. In: Proceedings the IEEE International Symposium on the Circuits and Systems (ISCAS '06); 21-24 May 2006; Greece. New York: IEEE; 2006. pp. 967-970

[14] Sandre GD, Bettine L, Calvetti E, Giacomi G, Posotti M, Borghi M, Zuliani P, Tortorelli I, Pellizzer F. Program circuit for a phase change memory array with 2 MB/s write throughput for embedded applications. In: Proceedings of the 34th European Solid-State Circuits Conference (ESSCIRC '08); 15-19 September 2008; Scotland, 2008. pp. 198-201

[15] Bedeschi F, Boffino C, Bonizzoni E, Resta C, Torelli G. Staircase-down SET programming approach for phase-change memories. Microelectronics Journal. 2007;**38**(10):1064-1069. DOI: 10.1016/j.mejo.2007.07.121

[16] Geoffrey W, Burr S, Matthew JB, Sebastian A, Cheng HY, Wu JY, Kim S, Norma E, Papandreou N, Lung HL, Pozidis H, Eleftheriou E, Lam CH. Recent progress in phase-change memory technology. IEEE Journal on Emerging and Selected Topics in Circuits and Systems. 2016;**6**(2):146-162. DOI: 10.1109/JETCAS.2016.2547718

[17] Kalb J, Spaepen F, Wuttig M. Atomic force microscopy measurements of crystal nucleation and growth rates in thin films of amorphous Te alloys. Applied Physics Letters. 2004;**84**(25):5240-5242. DOI: 10.1063/1.1764591

[18] Kang DH, Cheong BH, Jeong JH, Lee TS, Kim IH, Kim WM, Huh JY. Time-resolved analysis of the set process in an electrical phase-change memory device. Applied Physics Letters. 2005;**87**(25):253504. DOI: 10.1063/1.2149172

[19] Redaelli A, Ielmini D, Lacaita A, Pellizzer F, Pirovano A, Bez R. Impact of crystallization statistics on data retention for phase change memories. In: Proceedings the IEEE International Technical Digest on the Electron Devices Meeting (IEDM' 05); 5-7 December 2005; Washington, DC. New York: IEEE; 2005. pp. 742-745

[20] Sebastian A, Gallo ML, Krebs D. Crystal growth within a phase change memory cell. Nature Communications. 2014;**5**:4314. DOI: 10.1038/ncomms5314

[21] Wang YQ, Cai DL, Chen YF, Wang YC, Wei HY, Huo RR, Chen XG, Song ZT. Optimizing set performance for phase change memory with dual pulses set method. ECS Solid State Letters. 2015;**4**(7):Q32-Q35. DOI: 10.1149/2.0041507ssl

[22] Jeyasingh R, Fong SW, Lee J, Li ZJ, Chang KW, Mantegazza D, Asheghi M, Goodson KE, Wong HSP. Ultrafast characterization of phase-change material crystallization properties in the melt-quenched amorphous phase. Nano Letters. 2014;**14**(6):3419-3426. DOI: 10.1021/nl500940z

[23] Ielmini D, Lavizzari S, Sharma D, Lacaita AL. Physical interpretation, modeling and impact on phase change memory (PCM) reliability of resistance drift due to chalcogenide structural relaxation. In: Proceedings the IEEE International Technical Digest on the Electron Devices Meeting (IEDM' 07); 9-11 December 2007; Washington, DC. New York: IEEE; 2007. pp. 939-942

[24] Braga S, Cabrini A, Torelli G. Experimental analysis of partial-SET state stability in phase-change memories. IEEE Transactions on Electron Devices. 2011;**58**(2):517-522. DOI: 10.1109/TED.2010.2090157

[25] Kostylev S, Lowrey T. Drift of programmed resistance in electrical phase change memory devices. In: Proceedings of the European Phase Change and Ovonics Symposium (EPCOS, 08), 8-9 September 2008; Germany. pp. 117-124

Chapter 8

Analysis of Pyrolysis Kinetic Model for Processing of Thermogravimetric Analysis Data

Guodong Jiang and Liping Wei

Additional information is available at the end of the chapter

http://dx.doi.org/10.5772/intechopen.79226

Abstract

Pyrolysis has profound implications for coal as a raw material to make phase change material (PCM). It is necessary to derive a pyrolysis kinetic model for predicting the yield of volatiles and reaction performance during pyrolysis of coal, which is of significant importance for its thermal processing. The devolatilization of coal is characterized by thermogravimetric analysis (TGA) at different heating rates, and many kinetic models can be achieved by analyzing the TGA data. This work was aimed to find an appropriate model to describe the pyrolysis of coal and took Zhundong coal as an example. Four types of isoconversion kinetic methods, that is, Friedman, Flynn-Wall-Ozawa (FWO), Kissinger-Akahira-Sunose (KAS), Miura-Maki method, and different distributed activation energy models (DAEM) were employed here to fit TGA data for pyrolysis of Zhundong coal. The pre-exponential factors and activation energies obtained from different kinetic models were analyzed. An m-nth-DAEM was developed by considering that m classes of reactions took place with the same pre-exponential factor k_0 but different distribution activation energy following logistic distribution or Gaussian distribution. The results showed that the FWO model was better for description of pyrolysis process of Zhundong coal, and the 2-nth-DAEM assuming Gaussian distribution of activation energy gave the best fit for the TGA data of Zhundong coal. The research provides a valuable reference to the development of thermal utilization technology of Zhundong coal.

Keywords: phase change material (PCM), Zhundong coal, pyrolysis, thermogravimetry analysis, isoconversional methods, kinetics, distributed activation energy model

1. Introduction

Energy storage technology can solve the contradiction between energy supply and demand in time and space, so it is an effective way to improve energy utilization [1]. Thermal energy

storage is widely used in industrial and civilian applications, so it occupies an extremely important position in the field of energy storage technology. Phase change materials (PCM) will absorb or release a large amount of latent heat for energy storage when the state of matter changes. As a raw material for the preparation of phase change materials, coal has great energy storage density, and the output temperature and energy are relatively stable, so it has good application prospects [2]. Zhundong coalfield is the largest compositive basin in China, which has a large reserve of 390 Gt and is estimated to meet China's next 100-year coal consumption requirement [3]. In addition, Zhundong coal is more environmentally friendly than other types of coal owing to its extremely low sulfur and ash contents, which has a great significance to coal industry [4, 5]. Therefore, the investigation on Zhundong coal has theoretical and practical significance for the utilization of coal resources of China.

Thermal pyrolysis is the first stage reaction in most of coal thermal conversion processes (combustion, gasification, and liquefaction) and it is also one of the most promising technologies for clean and effective utilization of low-rank coal. During the pyrolysis process, various non-condensible gas and liquid phase matter such as tar are generated, which will lead to the weightlessness of coal samples. The weight losses of the coal range from 10 to 55%, which is affected by pyrolysis temperature, coal size, pyrolysis time and other factors such as pressure, atmosphere, heating rate and mineral content, etc. [6, 7]. The heating rate and pyrolysis temperature have an important influence on the pyrolysis characteristics of coal. The heating rate affects the concentration gradient of the product inside the particle and the ratio of gas phase substance to tar in the volatiles. The pyrolysis temperature determines the pyrolysis of the macromolecule reaction rate in the coal structure and the total release of volatile matters. A thermogravimetric analyzer (TGA) is routinely employed by many researchers to characterize moisture and volatile contents of various coals. It enables the user to monitor the weight change of a certain quality of coal samples as a function of time and temperature, which endue this method to incorporate the advantages of simple operation and good repeatability [8]. From the TG curve, we can obtain the key parameters such as the temperature of initial point of pyrolysis volatilization, the maximum release rate of volatile matter, and its corresponding temperature.

It is necessary to obtain an accurate knowledge of the pyrolysis process, since all the models of coal thermal conversion processes involve pyrolysis, and the kinetic behavior of these products in pyrolysis is fundamental to the optimization of their use. However, the actual phenomena of pyrolysis are complex and the kinetic parameters of which are difficult to obtain. To date, a large number of kinetic models have been proposed in the literature [5–15]. The models for processing TGA data and explaining the kinetic process of coal pyrolysis include first-order single reaction model (SRM), isoconversional or model-free methods, distributed activation energy model (DAEM). The SRM is the simplest, and it is applicable only over a narrow range of temperatures, thus limiting its applicability. Isoconversional or model-free methods are also used to process TGA data in which the kinetics parameters can be obtained without an explicit kinetics model [9]. Friedman method [10], Kissinger method [11], Flynn-Wall-Ozawa [12], and Miura-Maki method [13] are some of the outstanding methods in this classification. Several TGA curves at different heating rates for the same value of conversion are required for these models to determine activation energy for each conversion point. In recent years, nonlinear

regressions (least square optimization) are increasingly used to process the pyrolysis process of coals. More often than not, the distributed activation energy model (DAEM), originally developed by Pitt [14], has become the distinguished representative of them. It assumes that the coal pyrolysis should include a large number of independent, parallel, and irreversible n-order reactions with different activation energies. This distribution of activation energy corresponding to these infinite reactions is often represented by a distribution function of activation energy $f(E)$, which is usually used as logistic distribution or Gaussian distribution. Based on the DAEM, a two-Gaussian DAEM (2-DAEM) [15] has been developed by dividing the pyrolysis process into two steps. According to these indexes, the distributed activation energy model will be better improved and applied.

In the present paper, TGA experiments with pyrolysis of Zhundong coal at different heating rate have been carried out. The data was first processed using various isoconversional methods and then processed using the distributed activation energy model (DAEM). An m-nth-DAEM was developed to predict the weight loss of Zhundong coal, considering that m classes of reactions take place having the same pre-exponential factor k_0 and different distribution of activation energy.

2. Experiment

The experimental tests were with a TGA (Netzsch Model STA449F3). Before the pyrolysis experiments, coals were grounded and the finer particle fractions in a size range 0.075–0.15 (mm) were selected. **Table 1** shows the results of the proximate and ultimate analyses of the coal samples. Small samples were used to ensure uniform heating and to avoid problems of transport phenomena through the sample bed in the crucible. The instrument was first purged for 30 min with nitrogen to remove any remains of air, then further heated from room temperature to 1000°C at a heating rate of 10 $\left(\mathrm{K{\cdot}min^{-1}}\right)$, 20 $\left(\mathrm{K{\cdot}min^{-1}}\right)$, 30 $\left(\mathrm{K{\cdot}min^{-1}}\right)$ and 50 $\left(\mathrm{K{\cdot}min^{-1}}\right)$, respectively. The tests were conducted in an N_2 inert atmosphere, and the samples were maintained at the maximum temperature for 10 min until a constant mass was obtained at this temperature. All experiments at given heating rate were conducted two times and averaged to eliminate measure error. The experiments showed reproducibility within the range of ±3.7%.

Typical decomposition data of Zhundong coal obtained from the TGA experiments [9] are shown in **Figure 1**. The key characteristic parameters related to the main pyrolysis process are summarized in **Table 2**. The initial decomposition temperature is denoted as T_0, the corresponding temperature at the maximum point of the weight loss rate is denoted as T_p, the maximum weight loss rate at T_p is denoted as $R\infty$, and V_f is the weight loss corresponding

Proximate analysis (%)				**Ultimate analysis (%)**				
M_{ad}	A_{ad}	V_{ad}	FC_{ad}	C_d	H_d	O_d	N_d	$S_{t,d}$
9.96	15.46	22.49	52.09	70.55	3.49	7.64	0.62	0.53

Table 1. Proximate and ultimate analyses of raw Zhundong coal samples.

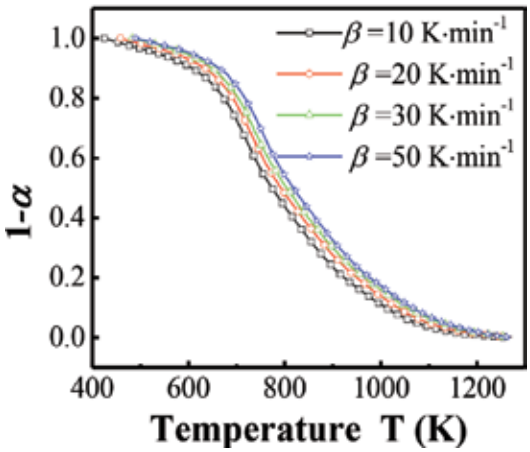

Figure 1. TGA curves of Zhundong coal samples during pyrolysis at different heating rates taken from literature [9].

β (K·min^{-1})	T_0 (K)	T_p (K)	R_∞ (%·min^{-1})	V_f (%)
10	425.39	718.95	0.90	35.8
20	458.89	731.25	1.75	36.4
30	482.89	735.25	2.85	38.0
50	489.86	752.75	5.34	37.9

Table 2. Pyrolysis characteristic values of coal samples.

to the final temperature. As can be seen from **Figure 1**, the mass fraction of releasing volatiles decreases with the increase of heating rate at the same temperature. The reason is that the increasing heating rate results in a thermal hysteresis, which makes the temperature inside the sample lower than the appearance, thereby leading to the value of $1-\alpha$ shifts to lager temperature. As can be seen from **Figure 1**, the TGA curve first decreases slightly due to small molecular gases being removed as the weak bonds are decomposed. Then tar-based volatile components and the formation of char result in a significant decrease of the TGA curve. At the end of the curve, it is close to horizontal, where a cross-linking reaction occurs. The TGA curve contains the main chemical reactions in the coal pyrolysis process, so it is the basis for the kinetic model investigation on coal pyrolysis.

3. Theoretical basis for thermal kinetics

For non-isothermal and heterogeneous systems, the thermal analysis kinetics is usually evolved from the theory of isothermal and homogeneous systems. The kinetics of reactions in isothermal and homogeneous systems for solids are generally described by Eq. (1)

http://dx.doi.org/10.5772/intechopen.79226

$$\frac{dV/V^*}{dt} = kf\left(\frac{V}{V^*}\right) \tag{1}$$

where V is total mass of volatiles released at time 't', V^* is the total mass of volatiles originally available for the reaction, $f\left(\frac{V}{V^*}\right)$ is the reaction model mechanism function, and k is the kinetic rate constant. The reaction rate constant varies with temperature and is assumed to follow the Arrhenius law [16].

$$k = k_0 e^{\left(-\frac{E}{RT}\right)} \tag{2}$$

In the above formula, k_0 refers to pre-exponential factor, E is the activation energy, R is universal gas constant, and T is the thermodynamic temperature. This equation is basically applicable to most elementary reactions and complex reactions, where k_0 and E are two important parameters that need to be combined with experimental and theoretical models. If the TGA experiment is conducted at a linear heating rate of β (K·min^{-1}), the temperature and time coordinates will be related to each other as:

$$T = T_0 + \beta t \tag{3}$$

Thus, $\beta = dT/dt$. Substituting Eq. (2) and (3) into Eq. (1) gives,

$$\beta\frac{dV/dV^*}{dT} = k_0 e^{\left(-\frac{E}{RT}\right)} f\left(\frac{V}{V^*}\right) \tag{4}$$

Assuming $\alpha = \frac{V}{V^*}$, then Eq. (4) becomes,

$$\beta\frac{d\alpha}{dT} = k_0 e^{\left(-\frac{E}{RT}\right)} f(\alpha) \tag{5}$$

For different reaction models, there are differences in the expression of $f(\alpha)$. One of the most commonly used reaction models is the reaction order model, which can be expressed as,

$$f(\alpha) = (1-\alpha)^n \tag{6}$$

The core issue of the general reaction kinetics of coal pyrolysis is determining the three factors k_0, $f(\alpha)$, and E [17], which is used as a key indicator to describe the process of devolatilization. In general, the integral form of the dynamical mechanism function $f(\alpha)$ is,

$$g(\alpha) = \int_0^\alpha \frac{d\alpha}{f(\alpha)} \tag{7}$$

The above is the basic knowledge of thermal analysis dynamics. Next, two methods, that is, the isoconversional model and the distributed activation energy model (DAEM), will be used to align the TGA data of Zhundong coal pyrolysis.

4. Isoconversional methods

4.1. Isoconversional theories

The basic assumption of the isoconversional method is: under different conditions of temperature rise, the activation energy corresponding to the same conversion rate remains the same [18], and the pyrolysis is specified to be a first-order reaction, that is, $n = 1$. Thus, $g(\alpha)$ can be written as,

$$g(\alpha) = -ln\,(1-\alpha) \tag{8}$$

The activation energy and pre-exponential factor for each conversion point can be obtained by analyzing several TGA curves at different heating rates for the same value of conversion (α). Next, we will focus on the typical isoconversional method for discussion, including a temperature differential method and three temperature integration methods.

4.1.1. Friedman method

Friedman model is a typical representative of the temperature differential method. Taking the logarithm of the Eq. (5) on both sides of the equal sign to obtain,

$$ln\left(\beta\frac{d\alpha}{dT}\right) = ln\,(k_0 f(\alpha)) - \frac{E}{RT} \tag{9}$$

The above formula is the general formula of the Friedman method. Thus, the plot of $ln\left(\beta\frac{d\alpha}{dT}\right)$ versus $1/T$ at the same conversion levels should be a straight line, the slope and intercept of which can be employed to specify the values of E and k_0, respectively.

4.1.2. Flynn-Wall-Ozawa method

Combining Eq. (5), Eq. (8) can be rewritten as

$$g(\alpha) = \int_0^\alpha \frac{d\alpha}{f(\alpha)} = \int_{T_0}^{T} \frac{k_0}{\beta} e^{\frac{-E}{RT}} dT \approx \int_0^T \frac{k_0}{\beta} e^{\frac{-E}{RT}} dT = \frac{k_0 E}{\beta R} p(u) \tag{10}$$

where $u = E/(RT)$ and $p(u)$ can be simplified by using integral approximation,

$$\begin{aligned} p(u) = \int_\infty^u \left(\frac{e^{-u}}{u^2}\right) du &= \frac{e^{-u}}{u^2}\Big|_\infty^u - \int_\infty^u e^{-u} du^{-2} = \frac{e^{-u}}{u^2} - \int_\infty^u 2u^{-3} de^{-u} \\ &= \frac{e^{-u}}{u^2} - \frac{2e^{-u}}{u^3} + \int_\infty^u 6u^{-4} de^{-u} \\ &= \frac{e^{-u}}{u^2} - \frac{2e^{-u}}{u^3} + \frac{6e^{-u}}{u^4}\Big|_\infty^u - \int_\infty^u e^{-u} d\frac{6}{u^4} = \cdots \\ &= \frac{e^{-u}}{u^2}\left(1 - \frac{2!}{u} + \frac{3!}{u^2} - \frac{4!}{u^3} + \cdots\right) \end{aligned} \tag{11}$$

Taking the first two items in parentheses on the right side of Eq. (11), we can get the approximate expression of $p(u)$,

$$p(u) = \frac{e^{-u}(u-2)}{u^3} \tag{12}$$

Performing logarithmic operation on both sides of the Eq. (12),

$$lnp(u) = -u + ln\,(u-2) - 3lnu \tag{13}$$

For a given solid fuel, in the temperature range of the thermal reaction stage, the value of u is generally ranging from 20 to 60 [19], which is, $20 \le u \le 60$, then $-1 \le (u-40)/20 \le 1$, take $s = (u-40)/20$, thus it gives,

$$u = 20s + 40 \tag{14}$$

Substituting Eq. (14) into Eq. (13), it gives,

$$lnp(u) = -u - 3ln\,40 + ln(38) + ln\left(1 + \frac{10s}{19}\right) - 3ln\left(1 + \frac{s}{2}\right) \tag{15}$$

Using the Taylor series expansion for the two logarithmic expressions to the right of Eq.(15) and taking a first-order approximate expression of each logarithmic, the following expression can be obtained:

$$lnp(u) \approx -5.3308 - 1.0516u \tag{16}$$

$$\mathrm{p}(u) = 0.0048e^{-1.0516u} \tag{17}$$

Substituting Eq. (17) into Eq. (10) yields,

$$g(\alpha) \approx \frac{k_0 E}{\beta R}\left(0.0048e^{-1.0516\frac{E}{RT}}\right) \tag{18}$$

Eq. (18) can be rewritten as,

$$ln\beta = ln\left(\frac{k_0 E}{Rg(\alpha)}\right) - 5.331 - 1.052\frac{E}{RT} \tag{19}$$

Eq. (19) is the integral form of the FWO model. The plot of $ln\beta$ versus $1/T$ at the same α value for different heating rates gives the E and k_0 value corresponding to the selected α.

4.1.3. Kissinger-Akahira-Sunose method

Taking the first item in parentheses on the right side of Eq. (11), the approximate expression of $p(u)$ can be rewritten as,

$$p(u) = e^{-u}/u^2 \tag{20}$$

Substituting Eq. (20) into Eq. (10) yields,

$$g(\alpha) = k_0 E e^{-u}/(\beta R u^2) \tag{21}$$

Performing Logarithmic operations on the two sides of Eq. (21) and then substituting $u = E/(RT)$ into the formula,

$$ln\left(\frac{\beta}{T^2}\right) = ln\left(\frac{k_0 R}{E g(\alpha)}\right) - \frac{E}{RT} \tag{22}$$

Eq. (22) is the holonomic form of the KAS model. Using Eq. (22), we can estimate both E and k_0 from the Arrhenius plot of $ln\left(\frac{\beta}{T^2}\right)$ versus $1/T$ at the selected α value and β values.

4.1.4. Miura-Maki method

In the Miura-Maki integral method, the approximation of the temperature integral is the same as the KAS method. Rearranging Eq. (22) and inserting Eq. (8) gives,

$$1 - \alpha \cong \exp\left[-\frac{\mathrm{k_0 RT^2}}{\beta E}\exp\left(-\frac{\mathrm{E}}{\mathrm{RT}}\right)\right] = \varnothing(E_s, T) \tag{23}$$

To derive the Miura-Maki integral method, the assumption of distributable activation energy model is used to approximate the right side of Eq. (23) as a step function at $E = E_s$ for a selected temperature. Furthermore, the activation energy E_s can be chosen to meet $\varnothing(E_s, T) = 0.58$ [12]. Substituting Eq. (8) into Eq. (22) yields

$$ln\left(\frac{\beta}{T^2}\right) = ln\left(\frac{k_0 R}{E}\right) - \ln[-ln\,(1-\alpha)] - \frac{E}{RT} \tag{24}$$

Inserting the value of $\varnothing(E_s, T)$ into Eq. (24) gives

$$ln\left(\frac{\beta}{T^2}\right) = ln\left(\frac{k_0 R}{E}\right) + 0.6075 - \frac{E}{RT} \tag{25}$$

Eq. (25) is the final expression of Miura-Maki method. The linear expression used to calculate the activation energy is similar to the KAS method, but there are some differences in the calculation results of the pre-exponential factor.

Generally speaking, the core methods of the above four models for calculating activation energy and pre-exponential factor are the same. The procedure to estimate $f(E)$ and k_0 using the four methods is as follows:

1. Measure α versus T relationships at least three different heating rates;
2. Calculate the values of $ln\left(\beta\frac{d\alpha}{dT}\right)$, for Friedman model, $ln\beta$, for FWO model, and $ln\left(\frac{\beta}{T^2}\right)$, for KAS/Miura-Maki model, at selected α values from the α versus T relationships obtained for different heating rates, respectively.

3. Plot $ln\left(\beta\frac{d\alpha}{dT}\right)$ versus $1/T$, for Friedman model, $ln\beta$ versus $1/T$, for FWO model,and $ln\left(\frac{\beta}{T^2}\right)$ versus $1/T$, for KAS/Miura-Maki model, at the selected α and then determine the activation energies E from the slopes and k_0 from the intercept, respectively.

The Friedman model is a representative of the differential method in the isoconversional method. The FWO model, KAS model, and Miura-Maki method are three typical integration methods. The integral equations all involve a general temperature integral, $\int_0^T \frac{k_0}{\beta} e^{\frac{-E}{RT}} dT$, which cannot be solved exactly, and different approximation methods have been proposed for this integral [13]. The KAS method and the Miura-Maki method express the above integral expression by a step-by-step integration formula, as shown in Eq. (11), and adopt the first item of the integration formula, which produces a lower accuracy. The FWO model performs two terms of the step-integration method, which improves the prediction accuracy. Nevertheless, Taylor approximation for the logarithm gives some errors. Two approximations may cause the FWO method to have some deviation from the experimental value. The Friedman method avoids the problem of integral approximation, but the numerical differential calculation will amplify the experimental noise. Unlike the three methods, the Miura-Maki method uses not only the temperature integral approximation, the same as KAS method, but also the assumption in the DAEM, as discussed below. It is obvious that all the isoconversional methods will cause some inevitable errors, so it is necessary to use a method with a good linear correlation to describe the TGA data.

4.2. Processing thermogravimetric analysis data by isoconversional methods

In order to obtain the key parameters of the Friedman, FWO, KAS, and Miura-Maki models, the value of α is chosen to ranges from 0.05 to 0.95 with an interval of 0.05 in this paper [10]. The activation energy and pre-exponential factor at selected α values can be obtained by the slope and intercept of the linear fit, respectively, as shown in **Figures 4–6** in literature [9]. The activation energy and pre-exponential factor obtained with the isoconversional and Miura-Maki methods with respect to the conversion extent (α) have been shown in **Figure 2**. It can be noted that activation energies obtained from the four methods were almost the same, and they all increase continuously with increased conversion rates. This is because the refractory molecules in coal must require more energy to be released in the form of volatiles. Note also that as the reaction proceeds, the logarithmic value of the pre-exponential factor first increases and then levels off. This indicates that as the temperature rises, the frequency of molecular collisions in the coal rises and the reaction tends to be strenuous; when the reaction proceeds to a certain degree, that is, $\mathrm{E} = 170\ \left(\mathrm{kJ{\cdot}mol^{-1}}\right)$, most of the molecules are in an activated state, and the reaction rate tends to be level, that is, pre-exponential factors fluctuate within an order of magnitude. The relationship between $ln\,k_0$ and E for Zhundong coal are also shown in **Figure 2**. It shows that before the activation energy was 170 $\left(\mathrm{kJ{\cdot}mol^{-1}}\right)$, $ln\,k_0$ and E showed a clear linear relationship, the so-called "kinetic compensation effect" [20], which would bring about some unavoidable errors to the solution of the activation energy and the pre-exponential factor of the reaction. When the activation energy is greater than 170 $\left(\mathrm{kJ{\cdot}mol^{-1}}\right)$, the value of the pre-exponential factor fluctuates above and below $ln\,k_0 = 23$. The fixed value of k_0 obtained here is to be used as a constant value of the k_0' in the distributed activation energy model. The range

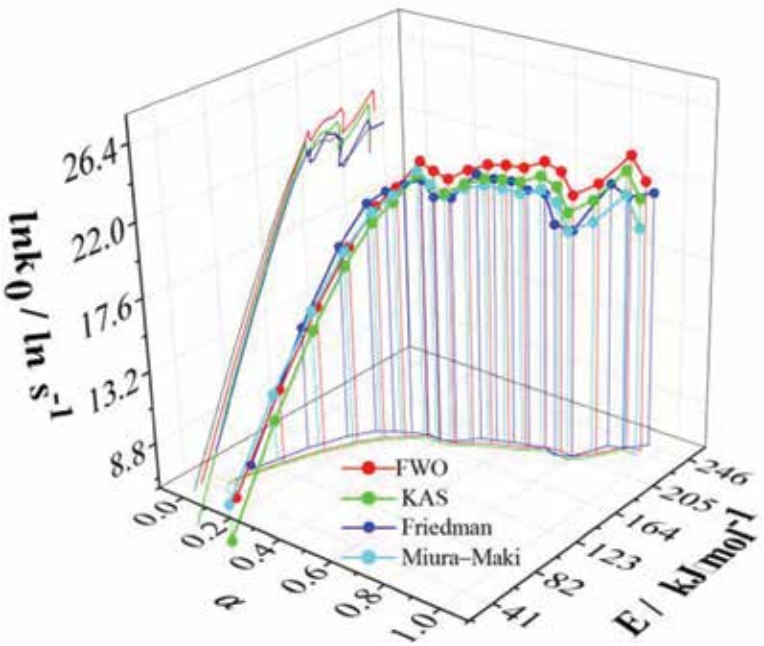

Figure 2. Comparison of activation energy and pre-exponential factor obtained with four different methods for Zhundong coal samples.

of kinetic parameters obtained for the four models is shown in **Table 3**. Since the three integration methods use certain approximation methods in the derivation process, and the differential method will amplify the experimental noise, a method with better linear correlation is used here to discuss the distribution of activation energy in the Zhundong coal. The linear correlation coefficients of the four models are listed in **Table 4**. It can be seen that when

Method	E_{min} $(kJ \cdot mol^{-1})$	E_{max} $(kJ \cdot mol^{-1})$	k_{min} (s^{-1})	k_{max} (s^{-1})
FWO	55	237	120.16	1.58E + 10
KAS	48.5	231.6	9.46	1E + 10
Miura-Maki	48.5	231.6	100.48	3.82 E + 9
Friedman	69.7	247	528.75	5.07E + 9

Table 3. Summary of the kinetic parameters obtained from different methods.

R^2 α **methods**	**0.15**	**0.25**	**0.35**	**0.45**	**0.55**	**0.65**	**0.75**	**0.85**	**0.95**
FWO	0.999	0.998	0.998	0.999	0.999	0.998	0.990	0.973	0.927
KAS/Miura-Maki	0.998	0.996	0.997	0.999	0.998	0.998	0.988	0.969	0.916
Friedman	0.999	0.996	0.997	0.998	0.997	0.993	0.973	0.974	0.881

Table 4. Linearly dependent coefficients for different methods at various α values.

http://dx.doi.org/10.5772/intechopen.79226

the value of α reaches 0.75 or more, the linear correlation coefficient square R^2 of the four methods shows a downward trend. For the FWO method, the linear correlation coefficient is kept above 0.92 when α is between 0.15 and 0.95, and the value of R^2 is higher than the other three methods. It shows that the FWO method describes the experimental data more accurately, and the obtained kinetic parameters are more reliable over a wide range of temperatures. **Figure 3** was obtained by differentiating the α versus E (calculated by FWO method) relationship. It can be seen that the $f(E)$ shows a unimodal distribution, with the peak at 173 $\left(\text{kJ}\cdot\text{mol}^{-1}\right)$ and the activation energy mainly in the range of 160–180 $\left(\text{kJ}\cdot\text{mol}^{-1}\right)$. The calculated activation energy distribution can be well fitted using the Gaussian function, where the correlation coefficient is 0.96. Comparison between the experimental and the simulated data by the FWO method (the best fit among the three methods) is shown in **Figure 4**. The error between the simulated values and the experimental results of α is less than 12.3%, so

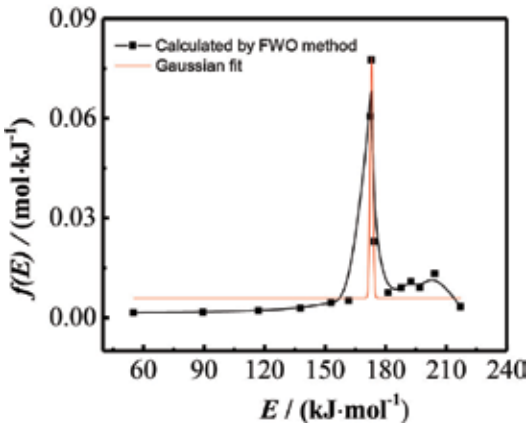

Figure 3. Pyrolysis activation energy distributions $f(E)$ based on FWO model.

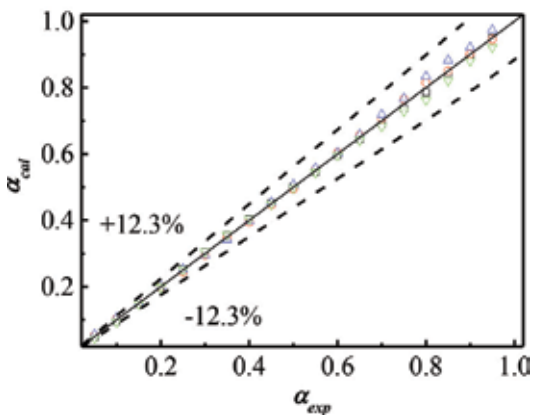

Figure 4. Comparison of calculation results from FWO method (α_{cal}) and experimental data (α_{exp}) of conversion.

FWO model achieves a good agreement with the experimental data over the whole range of conversion. But it needs more than three TGA curves to obtain the distributions of kinetic parameters, which will produce some inconvenience. Jain et al. [23] used Indian coal as an experimental sample and found that the results obtained by using the isoconversional methods at higher temperature had poor linear correlation. Therefore, the activation energy calculated by the isoconversional methods can only reflect the condition within a certain temperature range. However, the kinetic parameters obtained from isoconversional methods can provide inputs for selecting appropriate distributions for the DAEM.

5. Distributed activation energy model

5.1. Distributed activation energy model theory

The DAEM assumes that the original materials of coal contain plenty of constituents, which are numbered $i = 1, 2 \ldots j$. These components have different reaction activation energies [21]. Only when the reaction temperature reaches a certain value will they be released in the form of a volatile fraction. These reactions for diverse components are expressed as n-order reactions and are all irreversible and independent of the reactions in other components. The instantaneous volatilized mass fraction for the i_{th} constituent is denoted by $V_i(t)$, and the total released mass fraction for the ith constituent is $V_i^*(t)$. According to Eq. (4) and Eq. (6), the reaction rate of the mass fraction of releasing volatiles can be expressed as,

$$\beta \frac{dV_i/dV_i^*}{dT} = k_0 e^{\left(-\frac{E_i}{RT}\right)} \left(1 - \frac{V_i}{V_i^*}\right)^n \tag{26}$$

To some solid state reactions, the pre-exponential factor is connected with the temperature through the following relationship,

$$k_0 = k_0 T^{\gamma} \tag{27}$$

Combining Eq. (27), the integrating solution to Eq. (26) may be rewritten as,

$$\begin{aligned} \frac{V_i}{V_i^*} &= 1 - \left[1 - (1-n)\frac{k_0}{\beta}\int_0^T T^x e^{-E_i/RT} dT\right]^{1/(1-n)}, n \neq 1 \\ \frac{V_i}{V_i^*} &= 1 - exp\left[-\frac{k_0}{\beta}\int_0^T T^x e^{-E_i/RT} dT\right], n = 1 \end{aligned} \tag{28}$$

Considering the continuous reactants have different activation energies, the DAEM devotes to describe the energy distribution of the infinite complicated set of reactions, that is $j \to \infty$, as a function $f(E)$. Thus, the amount of volatiles loss that has an activation energy between E and $E + dE$ can be expressed as,

$$dV' = V^* f(E) dE \tag{29}$$

The integration of Eq. (29) brings about,

$$\int_0^\infty f(E)dE = 1 \tag{30}$$

The value of dV' is actually the same concept as V_i^*, which accounts for the total released mass fraction for the ith constituent which has an activation energy between E and $E + dE$. Let replace V_i^* and V_i with dV' and dV, respectively. Introducing Eq. (29) to Eq. (28), Eq. (28) has following expression.

$$\begin{aligned} dV &= V^*\left\{1 - \left[1 - (1-n)\frac{k_0'}{\beta}\int_0^T T^x e^{-E/RT}dT\right]^{1/(1-n)}\right\}f(E)dE, n \neq 1 \\ dV &= V^*\left\{1 - exp\left[-\frac{k_0'}{\beta}\int_0^T T^x e^{-E/RT}dT\right]\right\}f(E)dE, n = 1 \end{aligned} \tag{31}$$

By integrating Eq. (31), the following expression can be obtained,

$$\begin{aligned} 1 - \frac{\int_0^V dV}{V^*} &= 1 - \int_0^\infty \left\{1 - \left[1 - (1-n)\frac{k_0'}{\beta}\int_0^T T^x e^{-E/RT}dT\right]^{1/(1-n)}\right\}f(E)dE, n \neq 1 \\ 1 - \frac{\int_0^V dV}{V^*} &= 1 - \int_0^\infty \left[1 - exp\left(-\frac{k_0'}{\beta}\int_0^T T^x e^{-E/RT}dT\right)\right]f(E)dE, n = 1 \end{aligned} \tag{32}$$

Substituting Eq. (30) into Eq. (32), the equation yields,

$$\begin{aligned} 1 - \alpha &= \int_0^\infty \left[1 - (1-n)\frac{k_0'}{\beta}\int_0^T T^x e^{-E/RT}dT\right]^{1/(1-n)} f(E)dE, n \neq 1 \\ 1 - \alpha &= \int_0^\infty exp\left(-\frac{k_0'}{\beta}\int_0^T T^x e^{-E/RT}dT\right)f(E)dE, n = 1 \end{aligned} \tag{33}$$

A double model [15] was developed assuming that the pyrolysis process occurs in two steps with different kinetic behaviors. The pyrolysis process is divided into two steps: the tar and light hydrocarbon gas formation during the primary pyrolysis and the char condensation, cross-linking reactions, and a further gas production during the secondary pyrolysis. Two sets of parallel reactions occur, sharing the same pre-exponential factor but not the same distributed activation energy. The distribution function of activation of energy $f(E)$ in 2-DAEM equation can be written as,

$$f(E) = \omega f_1(E) + (1-\omega)f_2(E) \tag{34}$$

where ω is a parameter that weighs the different reaction classes, varying from 0 to 1. This parameter describes how many volatiles are released during the various reactions. $f_\varepsilon(E)$, where ε denotes the stage number, is a Gaussian or logistic function of the form with a mean activation energy E_0 and a standard deviation σ,

$$f(E) = \frac{1}{\sigma\sqrt{2\pi}} e^{-(E-E_0)/2\sigma_2}$$
$$f(E) = \frac{\pi}{\sqrt{3}\sigma} \frac{e^{\frac{-\pi(E-E_0)}{\sqrt{3}\sigma}}}{\left[1 + e^{\frac{-\pi(E-E_0)}{\sqrt{3}\sigma}}\right]^2} \tag{35}$$

In the 1-DAEM case, there are four parameters to be estimated: the mean activation energy E_0, the standard deviation σ, the temperature exponent x, and the chemical reaction order n. In the 2-DAEM case, there are seven parameters to be estimated: two mean activation energies E_{01} and E_{02}, two standard deviations σ_1 and σ_2, the temperature exponent γ, the chemical reaction order, and ω.

In this work, the model-fitting exercise was carried out using MATLAB TM (R2014b). It is essential to use an appropriate method to compute the inner dT integral of Eq. (33). An approximation proposed by Cai and Liu [21] was validated by literature [24], and was applied to estimate the general temperature integral,

$$\int_0^T T^{\gamma} e^{\left(-\frac{E}{RT}\right)} dT = \frac{RT^{\gamma+2}}{E} e^{\left(-\frac{E}{RT}\right)} \frac{0.99954E + (0.58058 - 0.044967\gamma)RT}{E + (2.54 + 0.94057\gamma)RT} \tag{36}$$

To deal with the outer dE integral of Eq. (33), Simpson's 1/3 rule [22] was employed. In the numerical integration of Eq. (33), $E_0 + 3\sigma$ value has been used for the upper limit of the outer dE integral. Therefore, for given values of the parameters, the DAEM equation can be numerically solved.

The kinetic parameters of the DAEM are determined using an objective function. An effective criterion for achieving the objective function is to minimize the differences of squares. The functional form of the objective function used in this paper is,

$$OF = \sum_x^l \left(\alpha_{x,cal} - \alpha_{x,exp}\right)_i^2 \tag{37}$$

where $\alpha_{x,cal}$ and $\alpha_{x,exp}$ are the calculated and experimental values of the residual mass fraction, l is data number, and the sub-index x makes reference to data point x. In this paper, the objective function (OF) has been optimized using the pattern search method [23], which is a class of direct search methods. The Gaussian and logistic DAEMs show an interrelationship between activation energies and the pre-exponential factor. Thus, E_0 obtained for DAEM differed significantly over values of k_0', and it was difficult to figure out their relationship. To remove this ambiguity, the k_0' was set to be a fixed value according to the results from isoconversional methods. The initial value of the mean activation energy E_0 and standard deviation σ settled in pattern search method used the results from isoconversional methods.

5.2. Processing thermogravimetric analysis data by distributed activation energy models

In the distributed activation energy models (DAEMS) adopted here, the pre-exponential factor k_0' is shared by all the reactions. From the literature [20], it is known that there exists an interrelation between the pre-exponential factor k_0' and the mean activation energy E_0, which

means that several pairs of k_0' and E_0 values can fit equally well for a given set of experimental data. Thereby, the value of k_0' has to be fixed to remove the mutual influence between k_0' and E_0. Nevertheless, when the value of k_0' is selected within two orders of magnitude, the observed correlation between k_0' and activation energy does not adversely influence the utility of kinetic models [24]. In this paper, the value of k_0' is set to be $1.0\mathrm{E}+10\left(S^{-1}\right)$, which is based on the results from the isoconversional methods discussed above. The initial guess value of $E_0\left(S^{-1}\right)$ used in the pattern search method of DAEMs is also based on the results from isoconversional methods of FWO model, as shown in **Figure 3**, which is corresponding to the peak activation energy and can be set to be 173 $\left(\mathrm{kJ{\cdot}mol^{-1}}\right)$. The expected initial value of σ was set to be 20 $\left(\mathrm{kJ{\cdot}mol^{-1}}\right)$, which is in accordance with the peak width of the $f(E)$ obtained from isoconversional methods. The value of the objective equation (*OF*) can be used as a benchmark for evaluating the prediction results obtained by different DAEMs.

The DAEMs were then applied to fit with the experimental data of $\beta = 20\ \left(\mathrm{K{\cdot}min^{-1}}\right)$. **Figure 5** shows the comparison of the various 1-DAE models. The kinetic parameters of these models and the parameters achieved with these models are listed in **Table 5**. It can be noticed from **Figure 5** that 1-DAE models with Gaussian/logistic distribution do not show good match with experimental values, which suggests that it is not appropriate to describe the pyrolysis process based on the single activation energy distribution for Zhundong coal. 2-DAEMs consider that pyrolysis occurs in two steps assuming that the first and the second stage share the same activation energy. The comparison of the various 2-DAE models with experimental results for Zhundong coal at a heating rate of $\beta = 20\ \left(\mathrm{K{\cdot}min^{-1}}\right)$ are shown in **Figure 6**, and the kinetic parameters extracted from these models are listed in **Table 6**. Looking at the value of *OF* listed in **Tables 5** and **6**, it can be concluded that 2-nth-DAEM assuming the Gaussian distribution gives best fit with the experimental data. From the values extracted with the 2-DAE models assuming the Gaussian distribution, as shown in **Table 6**, it can be seen that the mean activation energy for the primary pyrolysis (where breakage of weaker bonds takes place) is lower than the mean activation energy for the secondary pyrolysis (where breakage of tougher bonds takes place). However, the difference in activation energy between the two stages is not very

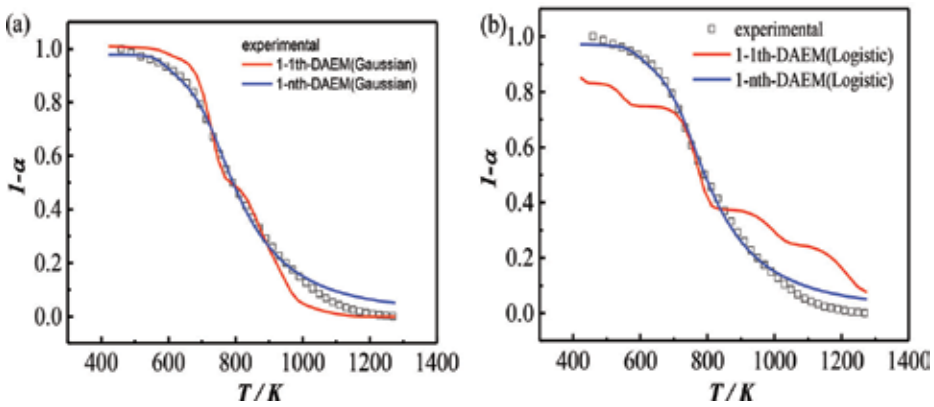

Figure 5. Comparison of experimental data and simulated data with the 1-DAEM methods: (a) Gaussian distribution; (b) logistic distribution.

		$E_0(kJ{\cdot}mol^{-1})$	$\sigma(kJ{\cdot}mol^{-1})$	γ	n	OF
$n=1$	Gaussian	169.42	24.45	−0.444	1	0.0493
	Logistic	175.11	79.84	−0.400	1	0.2148
$n\neq 1$	Gaussian	172.96	18.73	0.127	5.766	0.0058
	Logistic	172.96	19.35	0.132	5.786	0.0060

Table 5. Estimated values of kinetic parameters [1-DAEMs with Gaussian/logistic distribution functions].

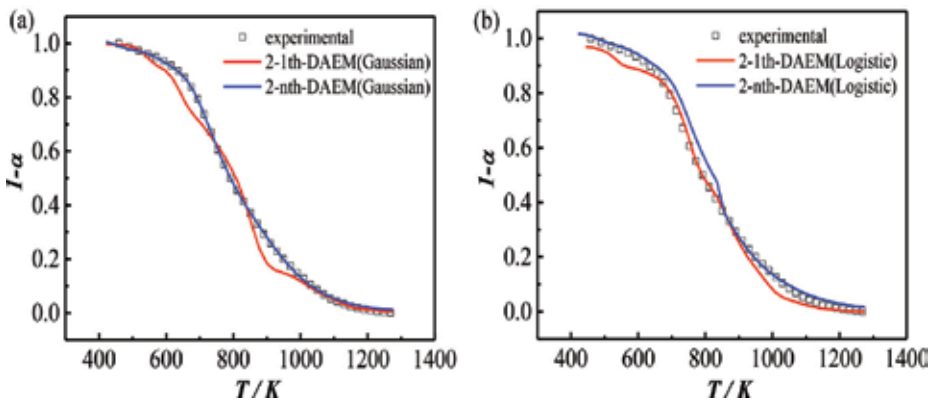

Figure 6. Comparison of experimental data and simulated data with the 2-DAEM methods: (a) Gaussian distribution; (b) logistic distribution.

Model		$E_{01}(kJ{\cdot}mol^{-1})$	$\sigma_1(kJ{\cdot}mol^{-1})$	$E_{02}(kJ{\cdot}mol^{-1})$	$\sigma_2(kJ{\cdot}mol^{-1})$	γ	n	ω	OF
$n=1$	Gaussian	150.00	20.00	173.00	36.85	−0.500	1	0.400	0.0492
	Logistic	151.02	41.89	171.08	25.06	−0.514	1	0.304	0.0160
$n\neq 1$	Gaussian	150.00	28.22	173.00	26.85	−0.502	2.872	0.646	0.0001
	Logistic	150.00	29.57	181.83	34.50	−0.513	2.826	0.765	0.0005

Table 6. Estimated values of kinetic parameters [2-DAEMs with Gaussian/logistic distribution functions].

large. This behavior is more visible with a view to the plots showed in **Figure 7** where the $f(E)$ function versus activation energy for 2-nth-DAEM with Gaussian distribution is exhibited. It can be concluded that the amount of volatile production attributed to primary pyrolysis stage is a little more than the secondary stage for the Zhundong coal. The original 2-DAEM put forward by Caprariis et al. [15] considers coal pyrolysis as a first order reaction, that is, n = 1, and the pre-exponential factor is a constant. This work takes all these factors into account and will be more conducive to better predictions.

The kinetic parameters extracted with 2-nth-DAEM with Gaussian distribution functions (best models to describe data at 20 $(K{\cdot}min^{-1})$ for Zhundong) were used to predict the experimental data obtained at different heating rates of 10 $(K{\cdot}min^{-1})$, 30 $(K{\cdot}min^{-1})$, and 50 $(K{\cdot}min^{-1})$, respectively. The results obtained with 2-nth-DAEM are shown in **Figure 8**. It can be seen that the 2-nth-DAEM with Gaussian distribution shows good match with other three heating rate curves.

http://dx.doi.org/10.5772/intechopen.79226

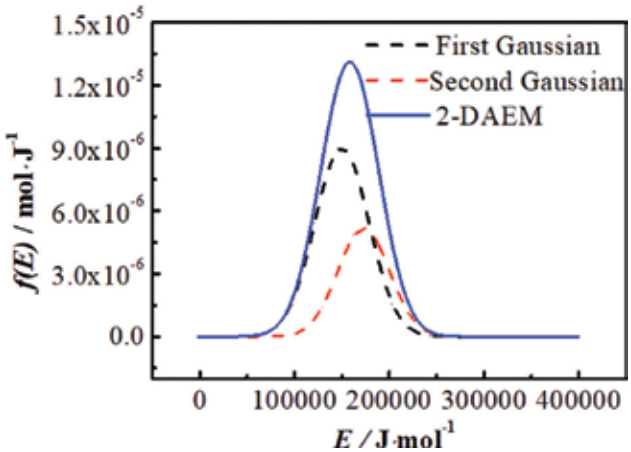

Figure 7. Distribution activation energy curves as a function of activation energy for 2-nth-DAEM with Gaussian distribution functions.

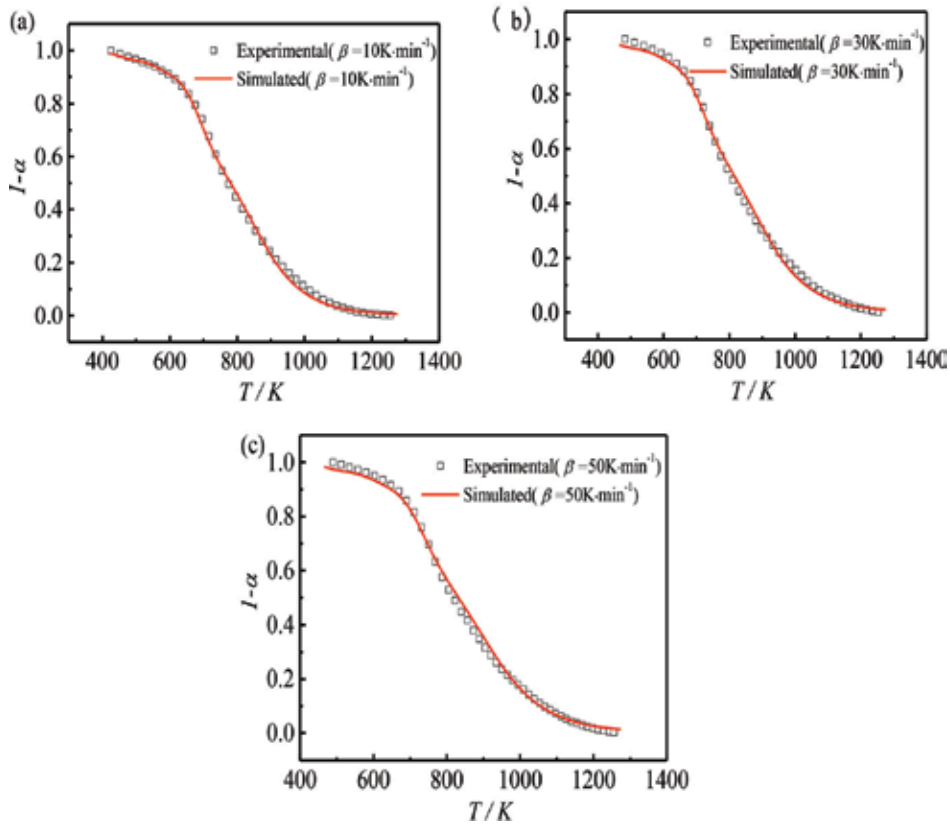

Figure 8. Comparison of predicted results with the experimental data at other heating rates with 2-nth-DAEM with Gaussian distribution functions: (a) $\beta = 10\ (\mathrm{K{\cdot}min^{-1}})$; (b) $\beta = 30\ (\mathrm{K{\cdot}min^{-1}})$; (c) $\beta = 50\ (\mathrm{K{\cdot}min^{-1}})$.

6. Conclusions

As a raw material for the preparation of phase change materials, coal is of great significance to energy utilization. In this work, Zhundong coal was taken as an example to investigate the pyrolysis process of it by means of thermogravimetric tests. In order to evolve appropriate kinetic parameters to characterize the pyrolysis process of coal, various methods and potential assumptions for processing TGA data were rigorously analyzed. The four isoconversional methods, that is, Friedman, FWO, KAS, and Miura-Maki method were used to calculate the activation energy and pre-exponential factor of Zhundong coal samples, respectively. It was found that the FWO model gave the best fit for the experimental data. During the pyrolysis process, the distribution of the activation energy of Zhundong coal, $f(E)$, shows a unimodal distribution, with a peak at the activation energy of 173 $\left(\text{kJ}\cdot\text{mol}^{-1}\right)$.In addition, Several DAEMs have been theoretically derived, considering the reaction order, the dependence of the pre-exponential factor on temperature, the steps mechanism for the pyrolysis, and the form of activation distribution, wherein the 2-nth-DAEM assuming Gaussians distribution of activation energy gave the best fit for the experimental data of Zhundong coal.

Acknowledgements

This work is currently supported by the National Natural Science Foundation of China through contract No.51606153 and China Postdoctoral Science Foundation (2017M3200).

Nomenclature

E	activation energy ($\text{kJ}\cdot\text{mol}^{-1}$)
E_0	mean activation energy ($\text{kJ}\cdot\text{mol}^{-1}$)
$f(E)$	distribution curve of the activation energy E
i	the number of constituents in original materials
k	rate coefficient $\left(s^{-1}\right)$
k_0	pre-exponential factor $\left(s^{-1}\right)$
n	The reaction order
R	universal gas constant ($\text{kJ}\cdot\text{mol}^{-1}\cdot\text{K}^{-1}$)
R_∞	maximum weight loss rate ($\%\cdot\text{min}^{-1}$)
T	temperature (K)
T_0	initial decomposition temperature (°C)

T_p	peak temperature (°C)
V	total mass of volatiles released at time 't' (%)
V_f	the corresponding weight loss percentage when the pyrolysis reaches the final temperature (%)
V^*	total amount of volatile yields (%)
α	Conversion
β	heating rate ($K \cdot min^{-1}$)
γ	Constant
ω	weighing factor
σ	standard deviation ($kJ \cdot mol^{-1}$)
Subscript	
cal	calculated value
exp	experimental value

Author details

Guodong Jiang[1] and Liping Wei[1,2]*

*Address all correspondence to: weiliping@nwu.edu.cn

1 School of Chemical Engineering, Northwest University, Xi'an, Shaanxi, China

2 Chemical Engineering Research Center of the Ministry of Education for Advanced Use Technology of Shanbei Energy, Northwest University, Xi'an, Shaanxi, China

References

[1] Tamme R, Steinmann WD, Laing D. Thermal energy storage technology for industrial process heat applications. ASME 2005 International Solar Energy Conference. 2005. pp. 417-422. DOI: 10.1115/ISEC2005-76250

[2] Murayama N, Yamamoto H, Shibata J. Mechanism of zeolite synthesis from coal fly ash by alkali hydrothermal reaction. International Journal of Mineral Processing. 2002;**64**:1-17. DOI: 10.1016/S0301-7516(01)00046-1

[3] Zhang K, Li Y, Wang Z. Pyrolysis behavior of a typical Chinese sub-bituminous Zhundong coal from moderate to high temperatures. Fuel. 2016;**185**:701-708. DOI: 10.1016/j.fuel.2016.08.038

[4] Tang H, Xu J, Dai Z. Functional mechanism of inorganic sodium on the structure and reactivity of Zhundong chars during pyrolysis. Energy & Fuels. 2017;**31**:10. DOI: 10.1021/acs.energyfuels.7b02253

[5] Zhao Y, Qiu P, Chen G. Selective enrichment of chemical structure during first grinding of Zhundong coal and its effect on pyrolysis reactivity. Fuel. 2017;**189**:46-56. DOI: 10.1016/j.fuel.2016.10.083

[6] Zeng X, Wang Y, Yu J, et al. Coal pyrolysis in a fluidized bed for adapting to a two-stage gasification process. Energy & Fuels. 2011;**25**:1092-1098. DOI: 10.1021/ef101441j

[7] Zhang J, Wang Y, Dong L. Decoupling gasification: Approach principle and technology justification. Energy & Fuels. 2010;**24**:6223-6232. DOI: 10.1021/ef101036c

[8] Nola GD, Jong WD, Spliethoff H. TG-FTIR characterization of coal and biomass single fuels and blends under slow heating rate conditions: Partitioning of the fuel-bound nitrogen. Fuel Processing Technology. 2010;**91**:103-115. DOI: 10.1016/j.fuproc.2009.09.001

[9] Jiang G, Wei L, Teng H. A kinetic model based on TGA data for pyrolysis of Zhundong coal. Ciesc Journal. 2017;**68**:1417-1422. DOI: 10.11949/j.issn.0438-1157.20161335

[10] Babiński P, Łabojko G, Kotyczka-Morańska M. Kinetics of coal and char oxycombustion studied by TG-FTIR. Journal of Thermal Analysis and Calorimetry. 2013;**113**:371-378. DOI: 10.1007/s10973-013-3002-x

[11] Cai J, Wang Y, Zhou L. Thermogravimetric analysis and kinetics of coal/plastic blends during co-pyrolysis in nitrogen atmosphere. Fuel Processing Technology. 2008;**89**:21-27. DOI: 10.1016/j.fuproc.2007.06.006

[12] Hao L. Combustion of coal chars in O_2/CO_2 and O_2/N_2 mixtures: A comparative study with non-isothermal thermogravimetric analyzer (TGA) tests. Energy & Fuels. 2009;**23**:4278-4285. DOI: 10.1021/ef9002928

[13] And KM, Maki T. A simple method for estimating *f(E)* and k_0 (E) in the distributed activation energy model. Energy & Fuels. 1998;**12**:864-869. DOI: 10.1021/EF970212Q

[14] Pitt GL. Fuel. 1962;**41**:267-274

[15] Caprariis BD, Filippis PD, Herce C. Double-Gaussian distributed activation energy model for coal devolatilization. Energy & Fuels. 2012;**26**:6153-6159. DOI: 10.1021/ef301092r

[16] Burnham A, Dinh L. A comparison of isoconversional and model-fitting approaches to kinetic parameter estimation and application predictions. Journal of Thermal Analysis and Calorimetry. 2007;**89**:479-490. DOI: 10.1007/s10973-006-8486-1

[17] Santos KG, Lobato FS, Lira TS. Sensitivity analysis applied to independent parallel reaction model for pyrolysis of bagasse. Chemical Engineering Research and Design. 2012;**90**:1989-1996. DOI: 10.1016/j.cherd.2012.04.007

[18] Starink MJ. The determination of activation energy from linear heating rate experiments: A comparison of the accuracy of isoconversion methods. Thermochimica Acta. 2003;**404**: 163-176. DOI: 10.1016/S0040-6031(03)00144-8

[19] Doyle CD. Kinetic analysis of thermogravimetric data. Journal of Applied Polymer Science. 1961;**5**:239-251. DOI: 10.1002/app.1961.070051506

[20] Vyazovkin S. Modification of the integral isoconversional method to account for variation in the activation energy. Journal of Computational Chemistry. 2001;**22**:178-183. DOI: 10.1002/1096-987X(20010130)22

[21] Cai J, Liu R. New distributed activation energy model: Numerical solution and application to pyrolysis kinetics of some types of biomass. Bioresource Technology. 2008;**99**:2795-2799. DOI: 10.1016/j.biortech.2007.06.033

[22] Suli E. An Introduction to numerical analysis. Mathematics of Computation. 2003:664. DOI: 10.1017/CBO9780511801181

[23] Cai J, Ji L. Pattern search method for determination of DAEM kinetic parameters from nonisothermal TGA data of biomass. Journal of Mathematical Chemistry. 2007;**42**:547-553. DOI: 10.1007/s10910-006-9130-9

[24] Jain AA, Mehra A, Ranade VV. Processing of TGA data: Analysis of isoconversional and model fitting methods. Fuel. 2016;**165**:490-498. DOI: 10.1016/j.fuel.2015.10.042

Edited by Mohsen Mhadhbi

Today, the application of phase change materials (PCMs) has developed in different industries, including the solar cooling and solar power plants, photovoltaic electricity systems, the space industry, waste heat recovery systems, preservation of food and pharmaceutical products, and domestic hot water. PCMs use the principle of latent heat thermal storage to absorb energy in large quantities when there is a surplus and release it when there is a deficit. This promising technology has already been successfully implemented in many construction projects. The aim of this book is to assist the scientists and to provide the reader with a comprehensive overview of the properties that characterize the phase change materials from theoretical and experimental perspectives with a focus on their technological applications. The present status and future perspectives of phase change material are discussed.

Published in London, UK

IntechOpen

ISBN 978-1-83881-623-0